ACTIVE CONTROL OF SUPERSONIC BOUNDARY LAYERS USING ELECTRIC ARC PLASMA ACTUATORS

BY

REBECCA JEANE OSTMAN

THESIS

Submitted in partial fulfillment of the requirements
for the degree of Master of Science in Aerospace Engineering
in the Graduate College of the
University of Illinois at Urbana-Champaign, 2013

Urbana, Illinois

Advisers:

Professor J. Craig Dutton
Professor Gregory S. Elliott

Abstract

Flow control, especially active control, has potential to vastly improve aerospace vehicles in terms of both efficiency and performance. Plasma actuators are a promising technology because they have no moving parts, fast response rates, and they can be forced at a wide range of frequencies. The two plasma actuators studied in this work are a Pulsed Plasma Jet (PPJ) and an array of Localized Arc Filament Plasma Actuators (LAFPAs), which both have shown promise for supersonic applications.

The PPJ design consists of three electrodes and two circuits. One circuit is a high-voltage, trigger circuit, which creates an arc discharge between the trigger electrode and anode, pre-ionizing the gas between the electrodes to facilitate the second arc discharge. The second circuit is a high-current, arc-sustaining circuit, which creates an arc between the cathode and the anode. The electrodes are all contained within a cavity that has a small orifice leading into the flow. When the arc discharges into the cavity, it heats and pressurizes the air within the cavity, which is then exhausted through the orifice. When the discharge ends, the cavity cools and draws air back into it, to reset it for the next cycle, making this a zero-net-mass-flux device, or a synthetic jet.

For this investigation, a single PPJ was placed in a Mach 3 crossflow, and the effect of a single pulse on the boundary layer was studied. Voltage measurements were obtained, which showed that the voltage required for the trigger breakdown was about 3.4 kV, and the arc-sustaining circuit was charged to a potential of 565 V. These measurements also showed that the timing and consistency of the discharges were much improved in the low pressure environment of the Mach 3 crossflow as compared to when the actuator was operated in quiescent, atmospheric conditions. PIV measurements were also obtained and these showed that the PPJ has a very modest effect on the boundary layer. These measurements showed that the PPJ fluctuates in strength over the course of a single pulse. This ‘chugging’ behavior is believed to be due to complex wave dynamics and reflections within the cavity. The maximum transverse velocity achieved by the jet was about 9.8% of the freestream velocity, and the maximum penetration of the jet into the crossflow was about 1.33δ. There was also some evidence in the Reynolds shear stress measurements that some backflow occurred just behind the jet orifice, especially at the times when the outward velocity was lowest, indicating that the cavity refilled at those times.

The LAFPA array used in this investigation consisted of four actuators evenly spaced along the span of the wind tunnel, and each actuator consisted of two electrodes set in small cavities recessed from the surface, but open to it. For most of the experiments, the current through the actuators was 1 A, and voltage measurements revealed that approximately 4.5 kV were required to initiate the breakdown between the electrodes. The LAFPAs were studied in two different flow situations: a boundary layer over a flat surface and a boundary layer over a 5º diverging ramp.

Schlieren imaging was used to investigate the LAFPA's effects on the stability of a normal shock. It was determined that actuation had virtually no effect on either the mean or standard deviation of the position of the normal shock, for either of the boundary layer configurations and regardless of stagnation-to-exit pressure ratio.

PIV was used to study the LAFPA's effects on the boundary layer. The LAFPAs once again had very minimal effects on the boundary layer over both the flat wall and the diverging ramp. Practically no difference in the streamwise velocity was visible between the control and no control cases, regardless of frequency of operation and delay time after the initiation of arc breakdown. The blast wave created by the LAFPAs is visible in the transverse velocity measurements, and it grows in time and is pushed downstream by the crossflow. This blast wave becomes weaker with increasing frequency. A plume of hot gas is also visible, emanating from the actuator cavities, at early delay times. This plume dissipates very quickly, is not observed to move downstream, and follows the same trend as the blast wave, becoming weaker with increasing frequency. Increasing the current from 1 A to 4 A increased the strength of the blast wave and hot gas plume, but again they followed the trend of decreasing strength with increasing frequency. Overall, the effects of the LAFPAs on the supersonic flows studied here were minimal.

Acknowledgements

There are many people whom I would like to thank for all of their help and support in this work. First, I would like to especially thank my advisers, Professors Craig Dutton and Greg Elliott, for the opportunity to do research with them and learn from them. Their guidance and expertise were invaluable, and they were always encouraging and supportive of me in my work. I would also like to extend heartfelt thanks to my colleagues and research partners for always being willing to help, with anything from assisting with experiments, to just listening and providing feedback on ideas. In particular, I would like to thank Brad Sanders, Todd Reedy, Tommy Herges, Nachiket Kale, Brad DeBlauw, Robyn Macdonald, and Richie Orozco. Additionally, I would like to thank my family, especially my parents, Larry and Marjory Ostman, and my sister, Celeste Ostman, for all of their support, not just during my graduate school experience, but also through all the years leading up to it. Without them I would not have even embarked on this grad school adventure, much less completed it. I also would not have been this successful without the support of my friends and family in the Champaign-Urbana area, especially my ultimate Frisbee teammates on Prion and my aunt, Leslie Ireland. Finally, I would also like to thank AFOSR with Dr. John Schmisseur as program monitor (Grant No. FA9550-10-1-0111) for supporting this research. Any opinions, findings, and conclusions or recommendations expressed in this material are those of the author and do not necessarily reflect the views of AFOSR.

Table of Contents

List of Abbreviations and Symbols

A, mA	amp, milli-amp
AFOSR	Air Force Office of Scientific Research
AIAA	American Institute of Aeronautics and Astronautics
B	magnetic field strength
C_f	skin friction coefficient
CCD	charge coupled device
DBD	dielectric barrier discharge
DC	direct current
DEHS	diethylhexyl sebacate
E	electric field strength
EHD	electohydrodynamic
EMI	electromagnetic interference
e	elementary charge
Fig.	Figure
H	shape factor
HV	high voltage
Hz, kHz	hertz, kilohertz
I_{EHD}	EHD interaction parameter
I_{MHD}	MHD interaction parameter
K	kelvin
kPa	kilopascals
L	length scale
LAFPA	localized arc filament plasma actuator
M	Mach number
MHD	magnetohydrodynamic
m, mm, nm	meters, millimeters, nanometers
m/s	meters per second
Nd:YAG	neodymium-doped yttrium aluminum garnet
n_+	ion number density
nF, µF	nanofarads, microfarads
no.	number
ns, µs	nanoseconds, microseconds
PFA	perfluoroalkoxy
PIV	particle image velocimetry
PPJ	pulsed plasma jet
pp.	pages
Q	minimum peak ratio
Re_{xy}	Reynolds shear stress
Re_θ	Reynolds number based on momentum thickness
RF	radio frequency
SBLI	shock/boundary layer interaction
SU	shock upstream
std. dev.	standard deviation
TTL	transistor-transistor logic
U_{diff}	velocity difference
U_x	streamwise velocity
U_y	transverse velocity
U_∞	freestream flow velocity
u_{Tot}	total uncertainty in velocity

u	gas velocity
u^+	velocity in wall normal coordinates
V, kV	volts, kilovolts
vol.	volume
X	distance downstream of actuators
x	streamwise-direction spatial variable
y	transverse-direction spatial variable
y^+	wall normal coordinate
$\Delta\varphi$	potential difference across the space charge region
δ	boundary layer thickness
δ^*	displacement thickness
ε_0	dielectric permeability of vacuum
θ	momentum thickness
Π	wake strength parameter
ρ	gas density
σ	electrical conductivity
Ω, kΩ	ohms, kilo-ohms
º	degrees
”	inches
~	approximately

1. Introduction

Since the invention of the first airplane, engineers have been designing more and more complex aerospace vehicles and pushing them into harsher and more extreme flow regimes. Additionally, there is increasing international and domestic pressure to improve fuel efficiency and reduce noise from both commercial and military aircraft. For these reasons, there has been a big push to develop and improve flow control methods for all flow regimes. There are many goals that an engineer might have for a particular flow control application; these include, but are certainly not limited to, delaying or advancing the transition to turbulence, suppressing or enhancing turbulence, and preventing or promoting flow separation. Some of the resulting benefits might include a reduction of drag, improvement of lift, enhancement of mixing, augmentation of heat transfer, and suppression of noise created by the flow. These could in turn lead to other broader benefits such as increased fuel efficiency, improved maneuverability, reduced weight, reduced noise, reduced cost, and improved compliance with environmental regulations (Kral, 1998).

Due to the potential benefits that flow control could provide, an extraordinary amount of research has gone into the development of numerous types of flow control strategies and devices. One way to classify flow control devices is based on where they are applied, either at a surface or far away from it.

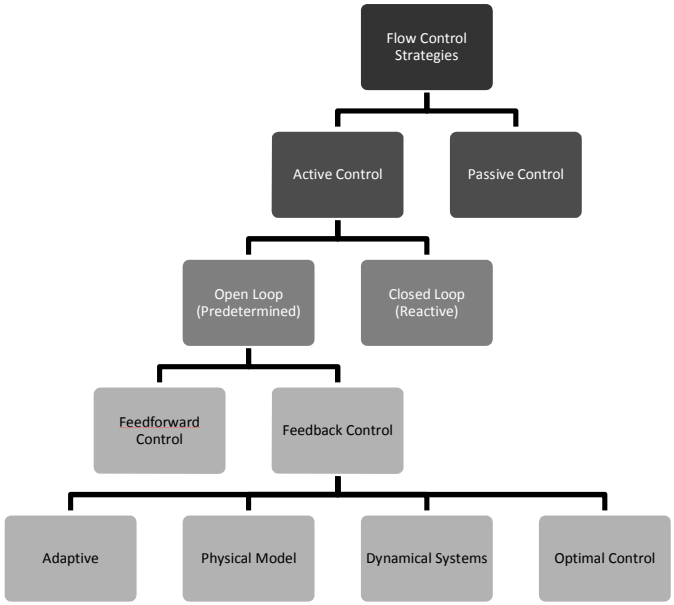

Fig. 1.1 Schematic of a commonly used flow control classification scheme.

Another classification scheme is based on the flow scale that the control device targets, either globally targeting the mean velocity profile or specifically targeting small dissipative eddies. Probably the most widely used classification scheme for flow control devices is based on the energy expenditure and control

loop used for the device. If the device requires no auxiliary power, it is referred to as a passive flow control device, or sometimes a flow management device. An active flow control device on the other hand, requires some kind of energy input and can be further classified by the type of control loop used. Open loop control, which is also called predetermined control, applies either steady or unsteady energy regardless of the state of the flow; this is advantageous because it requires no sensors. A closed loop control scheme, also called reactive control, does require sensors, but can adjust the energy to the device based on input from measurements of the flow (Gad-el-Hak, 1996). A schematic of this classification scheme is given in Fig. 1.1.

One of the many things that must be considered when designing a flow control device is the type of flow that is to be controlled and the flow control goal(s) associated with that type of flow. Free-shear flows are susceptible to inviscid instabilities due to the inflection point in the mean-velocity profiles. These types of flows are intrinsically unstable and are thus more easily manipulated than wall bounded flows, which are intrinsically stable and therefore harder to control. Control goals for free-shear flows include delay or advancement of transition, mixing enhancement, and/or noise suppression, while for wall-bounded flows they include delaying separation, reattaching a separated flow, and reducing drag/skin friction (Gad-el-Hak, 1996). As an example, for a turbulent boundary layer, drag reduction is a very common flow control goal, and one way to achieve this is thought to be through interrupting the "bursting" process. This process occurs in the sublayer of a turbulent boundary layer when elongated (along the streamwise direction) vortex pairs with alternating circulation abruptly lift away from the wall. The scales of this flow phenomenon are extremely small and thus, it is believed that some kind of micro-actuator would be appropriate to meet that flow control goal (Diez-Garias et al., 2000).

There are many challenges involved in designing or choosing a flow control device, but one of the most important ones is to design a simple device, both to operate and to manufacture, that achieves the desired flow control objectives while minimizing other adverse effects. Additionally, the benefit from the device should outweigh the cost and energy expenditure (Gad-el-hak, 1996). Passive flow control methods meet many of these requirements; they are generally simple to manufacture and implement and they require no additional energy input. Some examples of passive flow control methods include geometric shaping, fixed mechanical vortex generators, and longitudinal surface grooves or riblets. These have all been shown to be effective control methods; however, there are some drawbacks. The largest drawback of passive devices is that they are optimized for a narrow range of flow conditions, and at off design conditions they can have large penalties, such as increased drag (Kral, 1998).

Active flow control devices have a few advantages over passive devices: 1) the energy input can be varied so that active control can be used to control complex, dynamic processes and changing flow conditions (depending on the control loop used) and 2) they can be used to control natural instabilities of

a flow, so that a small, localized energy input can generate a large effect. However, these types of actuators are inherently more complex than passive devices, and some additional factors should be considered in their design such as robustness, practicality, power consumption, response time, reliability, and cost (Kral, 1998). In general, though, the potential benefits of active flow control are considered to be very substantial, and many types of actuators have been and are being investigated. Generally, these utilize one of three techniques: mechanical deflection of control surfaces, continuous or pulsed mass injection, and zero net mass flux synthetic jets (Cybyk et al., 2006).

Mechanical devices generally work by altering the vehicle surface to affect the flow. Some examples of these include Micro-Electro-Mechanical System (MEMS) flaps, electro-active polymers, electro-active ceramics, and shape memory alloys. MEMS devices are a particularly promising technology because they are of micron size scale and can be fabricated in large-scale batches. Additionally, they are easily integrated with sensors and electronics on the same scale, and arrays of sensors and actuators can be used over large surface areas. Their extremely small size makes MEMS devices ideal for control of flows with small-scale structures, such as turbulent, high-Reynolds-number flows. However, their small size also makes them unable to produce large forces (Ho and Tai, 1996).

Mass injection actuators involve expulsion of mass into a flow, for example from combustion of a gaseous fuel-air mixture inside a small chamber, which is then expelled through a small orifice into the flow (Crittenden et al., 2001). These types of actuators can also be pulsed, which has been shown to be effective for separation control, although a combination of steady and oscillatory blowing is potentially even more effective (Seifert et. al, 1993; Seifert and Pack, 1999). The main disadvantage of these types of actuators is that they require an external source of mass and/or fuel and require somewhat complex plumbing.

Synthetic jets generally involve a piezo-electric diaphragm inside a small cavity, with a small orifice in the wall opposite the diaphragm. As the diaphragm moves toward the orifice it forces air out of the cavity. At the edges of the orifice a vortex pair is formed and advects away from the orifice under its own self-induced velocity; this is illustrated in Fig. 1.2. Then as the diaphragm moves away from the orifice it draws air back into the cavity. Thus, these devices create a periodic jet using the working fluid of the flow they are immersed in; they transfer momentum, but no net mass (Cybyk et al., 2006; Glezer et al., 1998; Smith and Glezer, 1998).

There has been a considerable amount of work done showing that many of these devices are very effective actuators for subsonic flow. Periodically pulsed jets in particular, either synthetic or with mass injection, have been shown to be particularly effective at controlling boundary layer separation (Amitay et al., 1998; Crittenden et al., 2001; McManus et al., 1996, Seifert et al., 1993; Seifert and Pack, 1999; Wygnanski, 1997). In fact, it has been shown that one to three orders of magnitude less momentum input

is needed for a periodic jet than a traditional steady one (Wygnanski, 1997). However, many of these actuators may be unsuitable for controlling a supersonic flow. The synthetic jets have relatively low exhaust velocities that may not be sufficient to penetrate a supersonic boundary layer. Also, mass injection jets may have limited operational frequencies (~100 Hz) due to plumbing or finite combustion rates, which may be too low to excite natural instabilities in a supersonic flow. Additionally, many of these active flow control devices have complex, moving parts or plumbing, which tends to make them more expensive to build and maintain and can limit where the actuators can be applied.

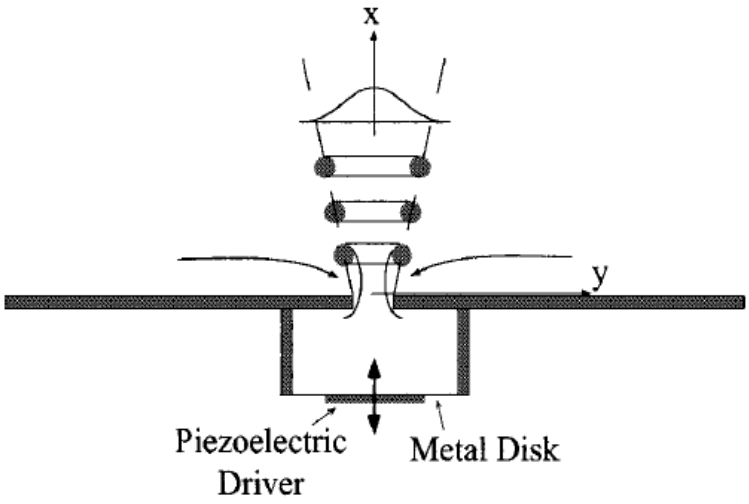

Fig. 1.2 Schematic of a synthetic jet, side view (Smith and Glezer, 1998)

In order to address some of the issues with these flow control devices, a fourth type of actuation has been developed and studied. This type of actuation uses either surface or volume-filling plasma for energy deposition in a flow, and it has many attractive characteristics, especially for high speed flow control. These actuators have no mechanical components, do not require an external supply of fuel or air, and have extremely short response times, high activation frequency, and phasing capabilities. There are three mechanisms that typically drive plasma actuators: electrohydrodynamic (EHD) interactions, magnetohydrodynamic (MHD) interactions, and volumetric gas Joule heating (Utkin et al., 2007).

EHD effects, also known as “ion wind,” are induced by the collisions of charged particles in an electric field with the neutral particles in the ambient gas and the resulting transfer of momentum. The strength of this effect is proportional to the net space charge density, and thus significant EHD effects can be expected in areas such as cathode sheaths or space-charge regions of corona discharges, which have

large space charges. This strength can be expressed by an interaction parameter which is the ratio of EHD push work to the fluid momentum flux and is given by the following equation:

$$I_{EHD} = \frac{\varepsilon_0 E^2}{2\rho u^2} \cong \frac{e n_+ \Delta\varphi}{\rho u^2} \quad (1)$$

where ε_0 is the dielectric permeability of vacuum, E is the electric field strength of the space charge region, ρ is the gas density, u is the gas velocity, *e* is the elementary charge, n_+ is the ion number density and Δφ is the potential difference across the space charge region. The fraction of the gas actually flowing through the space charge region is as important as the interaction parameter for that fraction of the gas. Additionally, at high pressures, where the interaction parameter can be significant (on the order of unity), the space charge region is extremely small (micron scale), and thus, the interaction can only affect a small portion of the overall flow. For boundary layer control this may not be a significant drawback, and from an examination of the equation for the interaction parameter, it is clear that the effect is stronger where the gas velocity is lower, i.e., in the boundary layer. (Macheret et al., 2004) However, EHD effects in a boundary layer are still only significant up to a freestream velocity of approximately 100 m/s (Utkin et al., 2007).

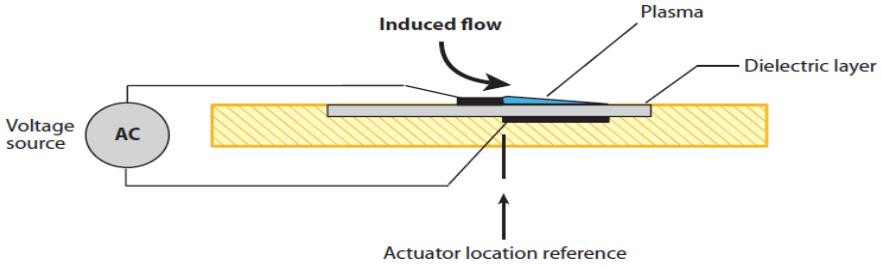

Fig. 1.3 Schematic of a typical dielectric barrier discharge (DBD) actuator (Corke et al., 2010)

Despite some of the limitations associated with EHD forcing, a significant amount of research has been done to study dielectric barrier discharge (DBD) actuators, which use this forcing mechanism. These actuators generally consist of two electrodes separated by a barrier made of a dielectric material (Fig. 1.3); this barrier prevents the glow discharge, formed between the electrodes when a voltage is applied, from becoming unstable and collapsing into thermal arcs. Additionally, the discharge is self-terminating due to the accumulation of electrons at the dielectric (Corke et al., 2010). As expected from analysis of the interaction parameter, these devices can be effective for subsonic flow applications, including reattachment of a separated boundary layer over an airfoil. DBDs have been shown to induce velocities on the order of tens of m/s, and if arrays of them are actuated successively at increasing phase angles, a

traveling electrostatic wave is generated that could improve their capabilities (Roth, 2003). However, due to their relatively weak effect, it is believed these types of actuators will be less effective for supersonic applications.

The most significant challenge in using MHD forcing for flow control is creating and sustaining adequate electrical conductivity in a flow. High-temperature atmospheric re-entry flows are practically the only type of flow in which ionization would not need to be created and sustained artificially, which requires additional power input that limits the performance of an MHD device (Macheret et al., 2004). Similar to EHD forcing, an interaction parameter describing the strength of MHD effects has been determined. It is the ratio of the Lorentz force work to the fluid momentum flux and is given by the following equation:

$$I_{MHD} = \frac{\sigma B^2 L}{\rho u} \tag{2}$$

where σ is the electrical conductivity, B is the magnetic field strength, L is the length scale, and ρ and u are again the gas density and velocity, respectively. Based on this equation and the conductivity currently achieved in non-equilibrium air plasmas, the gas density, and consequently pressure, must be very low for the MHD effect to be significant. Again, similar to EHD effects, MHD effects are larger in a boundary layer and higher pressure gas can be used (Utkin et al., 2007).

Both EHD and MHD forcing have fairly severe limitations that make them difficult to use as supersonic flow control mechanisms. EHD effects are only significant at low flow velocities and there is inevitably Joule heating that occurs, which produces thermal expansion and increases the viscosity, both of which oppose the EHD forces. MHD effects are only significant if the gas flow is ionized and additionally, for a low density gas in the presence of a strong magnetic field, gas Joule heating also becomes significant (Macheret et al., 2004). Since Joule heating tends to be the dominant effect in an electric discharge, a significant effort has been made to develop this effect as a flow control mechanism. Various different types of discharges have been studied such as glow discharges, filamentary arc discharges, and radio frequency (RF) discharges. Glow discharges and filamentary arc discharges are both local events that produce rapid, near-adiabatic heating and a subsequent pressure spike. This causes an artificial jet to form, which has been shown to produce weak oblique shock waves and induce separation (Utkin et al., 2007; Shin and Mahadevan, 2011). Glow discharges occur at lower current, ~1-100 mA, and are nonthermal, nonequilibrium plasmas, while filamentary arc discharges generally require much higher current, ~1 A, and are thermal, quasi-equilibrium. Glow discharges operate in two modes, diffuse and constricted, depending on the current and gas pressure. The diffuse mode has been the only one found to

achieve flow actuation, although this effect is weak. It is believed that EHD forces are still significant for glow discharges (Shin et al., 2007; Shin and Mahadevan, 2011). Filamentary arc discharges generally have higher current densities and higher temperatures, and devices based on this type of electric discharge are the focus of this work.

Arc discharges actually begin as glow discharges, which breakdown via the Townsend mechanism and are initiated by an electron avalanche. A strong electric field is created when a high electric potential is created between a cathode and an anode, causing electron flow to begin from the cathode to the anode. This electron flow ionizes the gas between the electrodes, creating more electrons and initiating a flow of ions back toward the cathode. These ions impact the cathode releasing even more electrons, and once the ion bombardment is sufficient, a self-sustaining current is initiated. For a glow discharge, there is not enough heating at the cathode for thermionic emission to be initiated, and the current remains low. For an arc discharge, the cathode heating does reach sufficient levels to initiate thermionic emission, and thus the current is much higher. Additionally, a streamer is formed connecting the electrodes by the coalescence of the channel of positive ions due to their own induced electric field (Fridman and Kennedy, 2004).

There are three main regions of the arc discharge: the cathode layer, the positive column, and the anode layer. The cathode layer, as its name suggests, is the area around the cathode and is characterized by a positive space charge due to the ions attracted to it. Similarly, the anode layer is the area around the anode, which is marked by a negative space charge. The voltage drop occurs primarily near the two electrodes due to these space charges. The positive column is quasi-neutral due to the presence of both ions and electrons and cannot sustain a large potential, although it is conducting. The majority of the Joule heating used for flow actuation occurs in the positive column (Fridman and Kennedy, 2004).

The current work focuses on the development of two devices that use arc discharges for supersonic flow control purposes. The first, called a pulsed plasma jet (PPJ), uses a three-electrode configuration to create the arc discharge, which is then placed inside a chamber with a small exhaust orifice. This effectively uses the arc discharge to create a synthetic jet, and is described in more detail in Chapter 2. The second device is called a localized arc filament plasma actuator (LAFPA), which uses a two electrode configuration within a recessed cavity. This actuator will be described in more detail in Chapter 3. The goal of this research is to study the effects of these two plasma actuators on supersonic boundary layers, in order to determine if they have sufficient control authority over this type of flow.

2. Pulsed Plasma Jet (PPJ)

2.1 Introduction

The pulsed plasma jet studied here is based on the "SparkJet" concept developed at The Johns Hopkins University Applied Physics Laboratory (Grossman et al., 2003). The device operates by creating an electric arc discharge inside a cavity, which heats the gas inside the cavity causing a sharp increase in pressure. This pressure increase forces the gas out of the cavity through an orifice, creating a jet. Once the gas has exhausted, there is a partial vacuum inside the cavity, which draws air back into it and resets it for the next cycle. This effectively creates a zero-net-mass-transfer synthetic jet, driven by the electric arc discharge.

A significant amount of research has been conducted on synthetic jets, although most of the devices studied are driven by piezoelectric disks set in a small chamber opposite an exhaust orifice. As the disk moves toward the orifice, it pushes fluid out of the chamber through the orifice. The sharp edges of the orifice cause the flow to separate and form a vortex sheet which rolls up into a vortex pair (this is for a slot-shaped orifice; for a circular orifice, such as the one for the PPJ studied here, a vortex ring is formed). This vortex pair then advects away from the orifice under its own self-induced velocity and another discrete vortex pair is formed at the orifice exit. As these vortex pairs travel downstream they begin to breakdown and transition to turbulence, ultimately forming a fully-developed turbulent jet. When the disk inside the cavity moves back away from the orifice it draws fluid back into the chamber, but it leaves the vortex pairs basically unaffected because they have enough induced momentum and have moved far enough from the orifice exit (Smith and Glezer, 1998; Glezer et al., 1998).

Almost all of the applications that piezoelectric-driven synthetic jets have been considered for have been in the subsonic regime. For example, they have been shown to be effective at reducing drag and enhancing lift on a cylinder (Amitay et al., 1998) and at delaying stall and improving reattachment of separated flow over a thick airfoil (Amitay et al., 1999). However, they have generally been considered unsuitable for supersonic flow regimes; this is because of relatively low jet exit velocities that may not be useful for control of high-speed flows.

So far, there has also been little work done investigating the use of conventional pulsed jets for supersonic flow control compared to the amount that has been done for subsonic flow control, and despite the successes in that regime. However, some studies have examined the mixing effectiveness of pulsed jets in supersonic crossflows, for application in ramjet and scramjet engines. Randolph et al. (1994) and Kouchi et al. (2010) both found that pulsed jets are able to penetrate into a supersonic crossflow significantly farther than a steady jet, at equivalent exit pressures and velocity ratios. Additionally, they found that mixing was improved with a pulsed jet. This is partly due to the different structure of the

pulsed jet. Most importantly, the Mach disk feature of steady jets, which is effectively a momentum sink, does not have time to form (Randolph et al., 1994). The ability of pulsed jets to have significant effects at lower velocity ratios, suggests that they may also be suitable for supersonic flow control applications.

The pulsed plasma jet studied in the current work is based on the SparkJet concept originally developed by Grossman et al. (2003). This first iteration of the SparkJet consisted of a cathode, an anode, and a grid; the breakdown is initiated by a low current cathode-to-grid breakdown, which ionizes the gas in the cavity and facilitates the high current, more conventional breakdown from the cathode to the anode. The second generation Sparkjet developed by Grossman et al. (2004) simplified the design by removing the grid. Cybyk et al. (2006) redesigned the Sparkjet to consist of three electrodes: a cathode, an anode, and a high-voltage trigger. The trigger ionizes the air gap with a kilovolt, low-amperage pulse, which is then followed by the discharge of a capacitor across the other two electrodes. This design significantly reduces the voltage required by the device. Caruana et al. (2009) sought to further simplify the device by reducing it to two electrodes, with the cathode being the "cap" into which the orifice was machined. However, this cap is heated by the electric discharge, and this heats the gas as it is drawn back into the cavity, resulting in reduced jet velocities.

The device considered here is the one characterized by Reedy et al. (2012), which is similar to the one used by Cybyk et al. (2006). Reedy et al. (2012) examined the effect of this PPJ on quiescent air and found that peak velocities of several hundred meters per second can be produced. Additionally, larger capacitors produced higher peak velocities, but with diminishing returns as capacitance was increased. Simulations by Cybyk et al. (2006) predicted jet velocities of several hundred meters per second, and a peak velocity of 100 m/s was observed experimentally. When placed in a Mach 3 crossflow, a similar Sparkjet design was observed to penetrate the flow by approximately 1.5 boundary layer thicknesses, and the momentum flux ratio of the PPJ to the freestream was about 0.6 (Narayanaswamy et al., 2010). A computational investigation was performed on a single pulse of the PPJ, both in quiescent air and exhausting into a Mach 3 turbulent boundary layer. This study found that the dimensionless impulse is the parameter of interest for evaluating control authority. The dimensionless impulse was found to be higher for the jet issuing into the supersonic turbulent boundary layer than into quiescent air (Anderson and Knight, 2012).

The current work continues investigations of the suitability of this plasma actuator for high-speed flow control applications by placing it in a Mach 3 crossflow and observing the effect of a single pulse on the boundary layer. Schlieren, electrical and particle image velocimetry (PIV) measurements are reported.

2.2 Experimental Set-Up

2.2.1 Wind Tunnel Facility

A supersonic blowdown wind tunnel designed for Mach 3.0 was used to investigate the effect of the PPJ on a Mach 3 boundary layer in cross-flow (Fig. 2.1a). The PPJ was positioned along the bottom wall of the 2.5” x 2.5” wind tunnel test section with the jet orifice machined into the wall. The PPJ was machined into a tiered perfluoroalkoxy (PFA) cylinder containing the cavity geometry (Figs. 2.1b and 2.2). The PFA cylinder had a 19 mm diameter with a 0.83 mm jet orifice between the 4.76 mm diameter cavity and test section. The cavity had a height of 10.16 mm. The cavity-containing PFA cylinder had three grooves extending away from the cavity to receive the three electrodes (Fig. 2.1b). The PPJ geometry employed was obtained from Reedy et al. (2012).

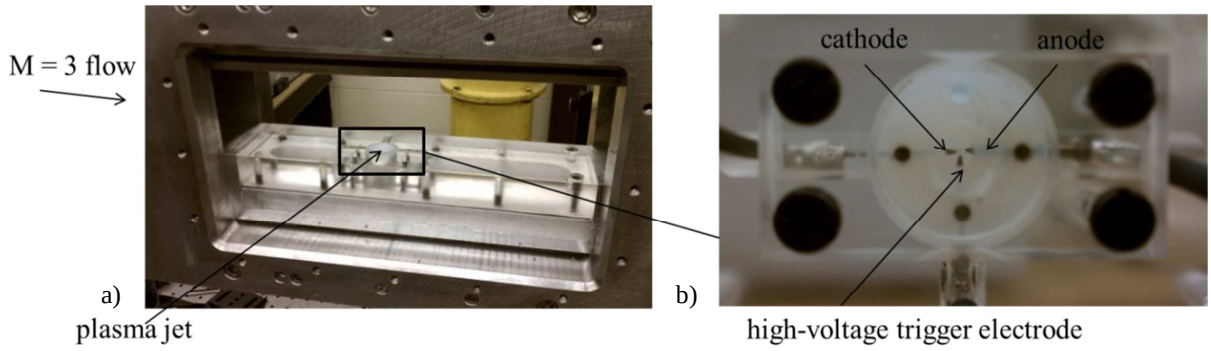

Fig. 2.1 Pulsed plasma jet (a) inside wind tunnel test section, and (b) electrode arrangement. (Sanders, 2012)

The tunnel stagnation pressure during this investigation was 482.6±6 kPa, while the total temperature was 303 K with a unit Reynolds number of 34×10^6 m^{-1}. The tunnel flow was controlled by both a pneumatic valve, with a Fisher TL 101 Process Controller, and a manual gate valve. There were three pressure transducers, one for the supply tank, one for the tunnel stagnation pressure, and one for the static pressure in the test section. A thermocouple mounted in the stagnation chamber of the tunnel measured the total temperature.

2.2.2 Pulsed Plasma Jet

The design of the PPJ used in the current work is a three-electrode PPJ (Reedy et al., 2012). The three electrodes consisted of a high-voltage trigger electrode made of ceriated tungsten, grounded cathode also made of ceriated tungsten, and an iridium-plated automotive sparkplug tip for the arc-sustaining anode (Fig. 2.2). The iridium-plated sparkplug tip was used as the anode to mitigate corrosion and extend the lifecycle of the actuator. The cathode and trigger electrode had a 1 mm diameter with sharpened tips ending in a truncated cone shape. The three electrodes were positioned in the same plane inside the 4.76 mm diameter chamber with the trigger electrode perpendicular to the anode and cathode. The electrode

spacing was determined empirically to maximize plasma breakdown consistency and minimize electrode corrosion (Reedy et al., 2012). This resulted in spacing between the anode and cathode of approximately 0.72 mm, and 0.2 mm between the trigger electrode and cathode.

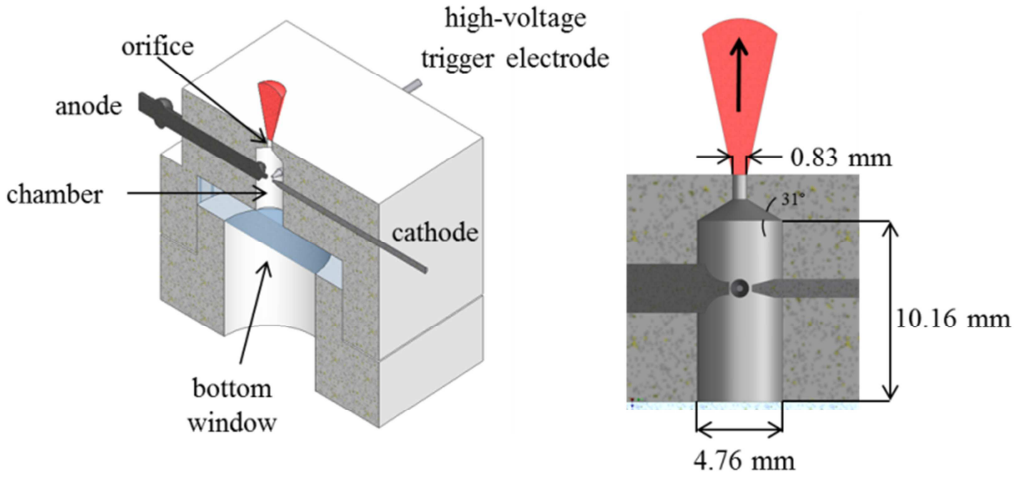

Fig. 2.2 Pulsed plasma jet design and geometry (Reedy et al., 2012)

Two electrical circuits were utilized for the actuation of the PPJ (Fig. 2.3). These consisted of a high-voltage/low-current trigger circuit and a low-voltage/high-current arc-sustaining circuit. A 22 kV low amperage output from an Information Unlimited Igniter10 high-voltage generator was connected through an ignition coil to the trigger electrode. An envelope of ionized gas between the anode and cathode was created using a low-energy spark across the trigger electrode and cathode. This spark was generated by the high-voltage power supply. The ionized gas caused the continuously-charged capacitor in the second circuit to discharge, forming a high-current electric arc between the anode and cathode. A 2 μF capacitor was connected to the anode and was continuously charged by an Acopian U500Y20 DC power supply with an unregulated nominal 500-V, 0.2-A output (Reedy et al., 2012). A 3.3-kΩ resistor was placed in series with the DC power supply to limit the capacitor charging current. A detailed description of the actuator and the operational and safety procedures are also given in Reedy (2013) and Sanders (2012).

2.2.3 Particle Image Velocimetry

PIV images were acquired using a laser sheet directed into the test section vertically along its center span. A dual-head New Wave Nd:YAG laser provided a 532-nm light sheet that was focused into the wind tunnel test section through the top window of the wind tunnel, using the set up seen in the schematic in Fig. 2.4a (Fig. 2.4 is not drawn to scale). The laser sheet impinged along the plasma jet orifice centerline illuminating the streamwise xy plane of the flowfield near the jet orifice, as seen in Fig.

2.4b. The bottom of the test section was painted black in order to reduce laser glare. A Vicount 1300 smoke generator, with a modified heat exchanger to allow it to be operated at higher pressures, was used to produce seed particles. The smoke generator used Smoke Fluid 180 (mineral oil) to produce particles ~0.2 μm in diameter, which gives a Stokes number of 0.01-0.02. This Stokes number is well below 0.1, which indicates that the particles track the flow well (Samimy and Lele, 1991).

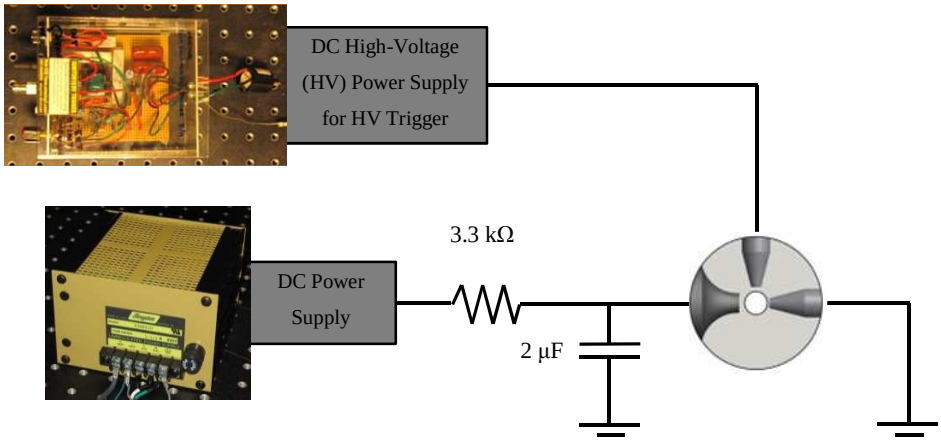

Fig. 2.3 Pulsed plasma jet (PPJ) circuit schematic (Reedy et al., 2012)

Phase-locked PIV images were acquired at various delay times following the PPJ actuation. A Quantum Composers pulse/delay generator was used to control the timing for the PPJ, PCO.1600 CCD image acquisition camera, and laser. The PPJ was pulsed at a low frequency of 5 Hz to capture the behavior of single-pulse jets in the Mach 3 cross-flow. The delay on the signal between the PPJ and PIV system varied throughout the experiments to capture the time progression through the PPJ actuation cycle. Two Agilent N2771A high-voltage probes were used to monitor the voltage from the high-voltage trigger and the capacitor discharge upon plasma breakdown. A Pico Technology PicoScope 4424 PC oscilloscope was used to monitor and acquire the voltage traces corresponding with each PIV image pair.

The image pairs were analyzed using LaVision DaVis 8.1 PIV analysis software. The particle displacements were determined using multi-pass, cross-correlation calculations using 50% interrogation region overlap. The initial interrogation region was 64 by 64 pixels, while the final passes were reduced to a 32 by 32 region size. Post-process filtering was used to remove erroneous vectors; this included a minimum peak ratio Q of 1.5.

An approximate, but conservative estimate of the uncertainty of the PIV measurements was made based on the method described by Lazar et al. (2010). Uncertainty in PIV comes from four main sources: equipment, particle dynamics, sampling, and image processing. The total uncertainty as a fraction of the freestream velocity is given for a sample case (time delay of 20 μs after the plasma initiation) in Fig. 2.5; this case was chosen because it is a representative case and it appeared to have the largest velocity

gradients, which contribute significantly to particle dynamics and processing errors. In this study, the average total uncertainty is about 1.3% of the freestream velocity, although around the PPJ orifice and the

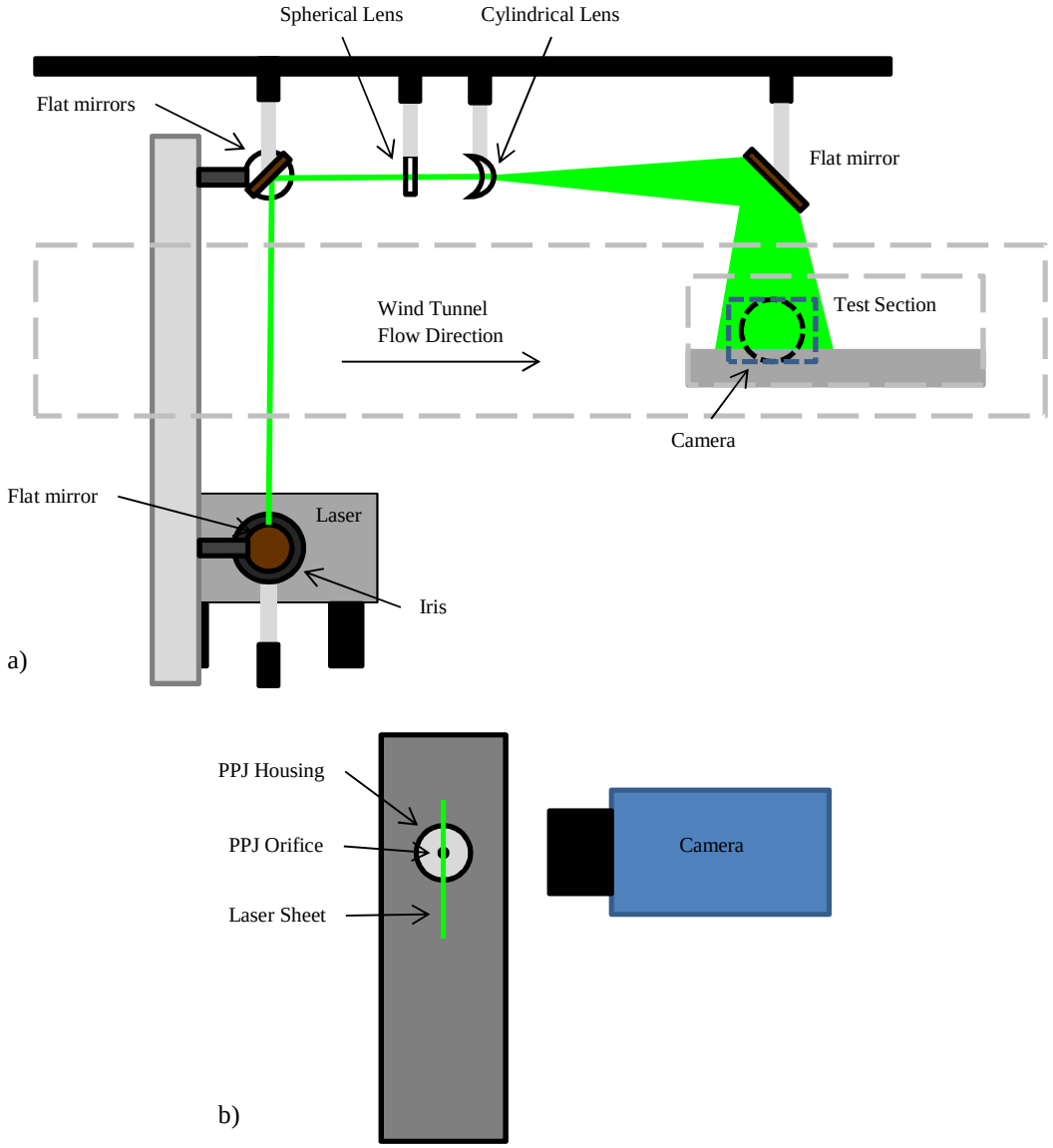

Fig. 2.4 Schematic (not to scale) of PIV a) optical set up and b) laser sheet position.

shocks created by the PPJ, the uncertainty was found to be as high as 6.0% of the freestream. For the flowfield as a whole, the equipment error and the processing error were the largest contributors; on average these were about 1.0% and 0.7%, respectively. However, in the boundary layer the sampling error became a large contributor at up to 2.0%. This is due to poorer seeding in the boundary layer and glare from proximity to the floor of the tunnel, which resulted in a reduced number of usable vectors in the boundary layer. Additionally, around the shock and PPJ orifice there was an increase in the particle lag error, up to 5.8%, due to the larger velocity gradients that occurred in those areas. Overall, the uncertainty

in the PIV measurements for this investigation is relatively small, and the data represent the flowfield well.

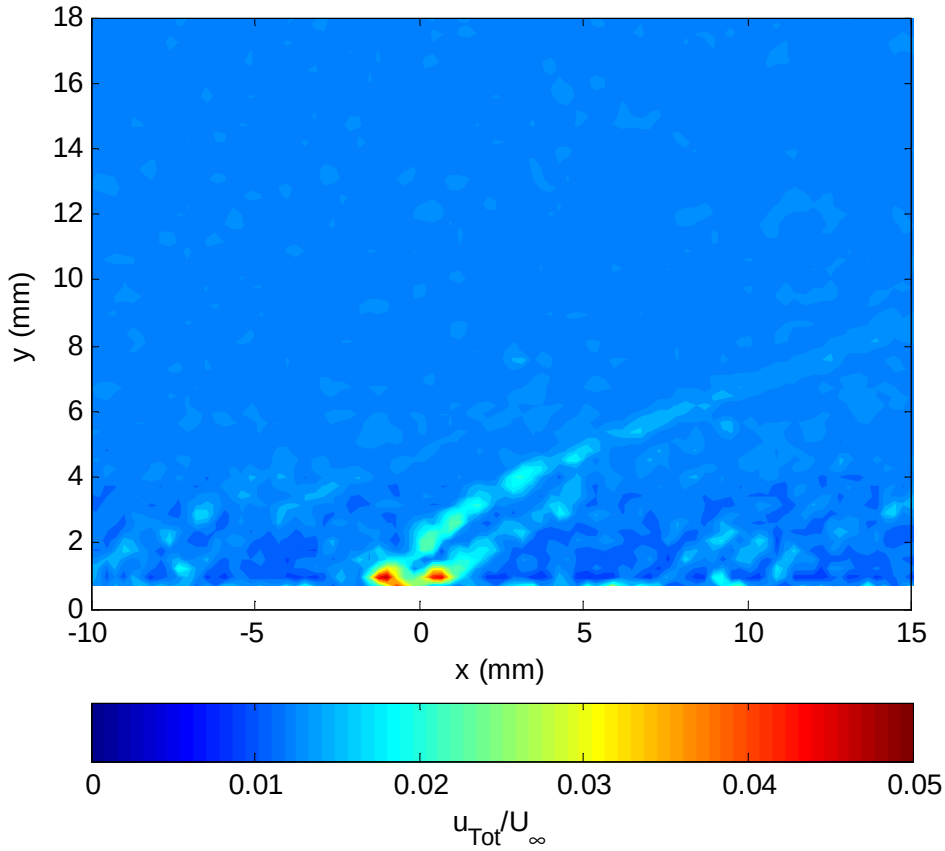

Fig. 2.5 Total uncertainty divided by the freestream velocity. Typical PPJ case at 20 µs delay.

2.3 Results

2.3.1 Voltage Measurements

For each PIV image pair, voltage traces of the high-voltage trigger and the capacitor discharges were recorded to monitor the electrical characteristics of the PPJ. The averaged (top) and an instantaneous (bottom) trace are shown in Fig. 2.6. The PPJ is initiated by charging the high-voltage trigger until breakdown occurs, at approximately 3.4 kV. This breakdown then triggers a discharge of the capacitor circuit, which is charged to an electric potential of 565 V for each actuation. The two discharges took about 8 µs. The timing of the capacitor discharge with respect to the high-voltage trigger was very consistent; the capacitor discharge was always within nanoseconds of the high-voltage trigger. Additionally, there were no instances of the capacitor failing to discharge following the high-voltage trigger (misfire). This is in contrast to what Reedy et al. (2012) observed in quiescent, ambient conditions,

where the timing was inconsistent and some misfires occurred. These improvements in performance under Mach 3 conditions are due to the much lower static pressure that makes electric breakdown easier.

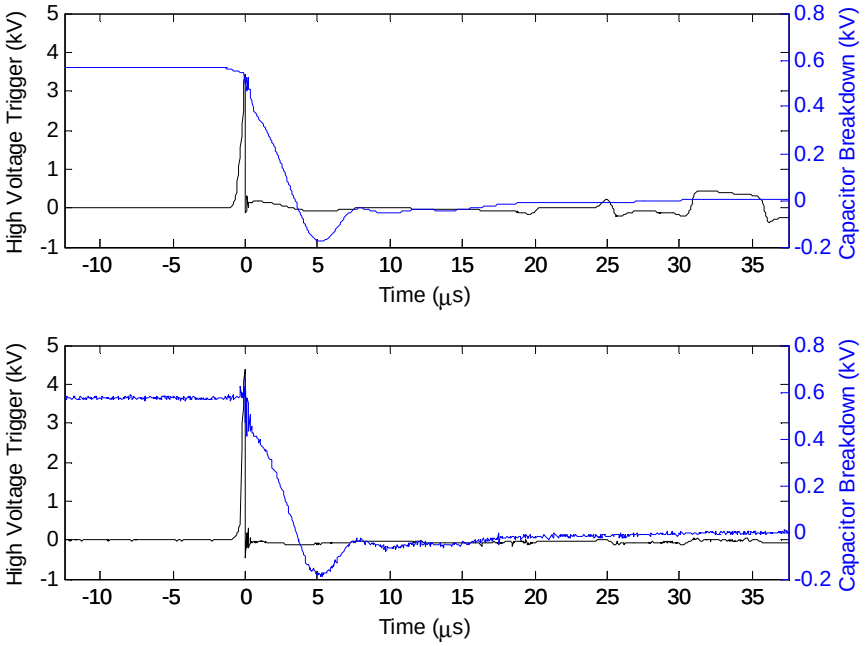

Fig. 2.6 Average and instantaneous voltage traces for the high voltage trigger and the capacitor breakdowns.

2.3.2 Schlieren Images

An instantaneous schlieren image of the Mach 3 flowfield with the PPJ orifice present, but without actuation, is displayed in Fig. 2.7. The instantaneous schlieren image was obtained with a 20 ns spark source duration. Weak Mach waves are present in the freestream due to small imperfections in the wind tunnel joints upstream of the test section. The un-actuated PPJ orifice also produces a weak Mach wave. The fully developed turbulent boundary layer is clearly observed.

2.3.3 Incoming Boundary Layer

PIV measurements were obtained in order to characterize the incoming boundary layer. This was done to establish the baseline flow with which to compare the actuated flow. The boundary layer thickness of the incoming flow was determined by the wall-normal distance at 99% of the mean freestream velocity and was found to be approximately 5.61 mm. A modified wall wake velocity profile for turbulent compressible boundary layers, as discussed in (Sun and Childs, 1973), was fit to the measurements of the incoming boundary layer. The comparison of the modified wall wake velocity profile to the experimental measurements for the incoming boundary layer is shown in Fig. 2.8. The incompressible shape factor, *H*, (listed in Table 2.1 along with other relevant parameters) is marginally

higher than the typical value of 1.3 for a fully developed turbulent boundary layer. The wake strength parameter, Π, is significantly higher than the typical turbulent boundary layer value of 0.55 ± 0.05 for a compressible turbulent boundary layer with $Re_\theta > 2000$ (Fernholz and Finley, 1980). These values indicate that the Mach 3 boundary layer may not be completely in equilibrium.

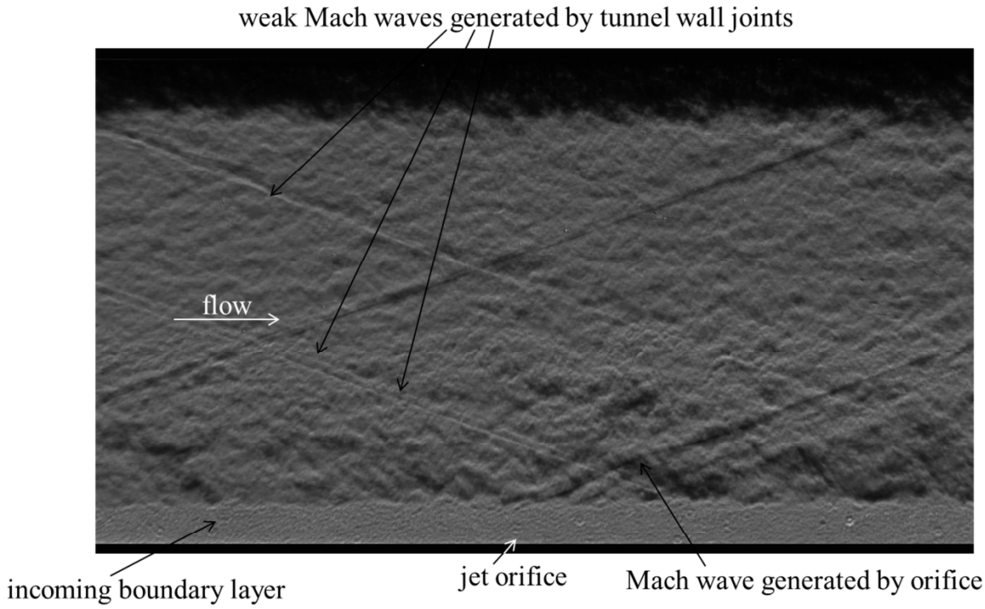

Fig. 2.7 Instantaneous Schlieren photograph of test section without PPJ actuation

2.3.4 Flowfield PIV Measurements

Figure 2.9 shows the mean streamwise velocity, normalized by the incoming freestream velocity, for the no-control case and actuated cases with delay times of 20 µs, 30 µs, 40 µs, 60 µs, 70 µs, 90 µs, and 100 µs after the high-voltage breakdown. The freestream velocity is about 620 m/s. The effect of the PPJ on the streamwise velocity is rather small, but there is a slight disturbance slightly downstream of the jet orifice. This disturbance starts at 20 µs and is also the strongest at this delay time. The strength of the disturbance diminishes slightly at 30 µs, but at 40 µs has regained some strength. At 60 µs the disturbance is barely noticeable, but then following that, the disturbance again becomes stronger, until 100 µs, when the disturbance again has weakened. At the delay times for which the jet is stronger, the disturbance appears to propagate downstream within the boundary layer. However, these disturbances are very small.

The pattern of fluctuating jet strength is much more noticeable in the average transverse velocity, which is shown in Fig. 2.10, again normalized by the freestream velocity. There are contour lines on some of these plots, which were used in determining the penetration of the jet, and will be explained later. The maximum transverse velocity created by the jet occurs at 20 µs and is about 61 m/s, which is about 9.8% of the freestream velocity. At 30 µs the velocity in the jet is reduced, but it recovers and grows until 60

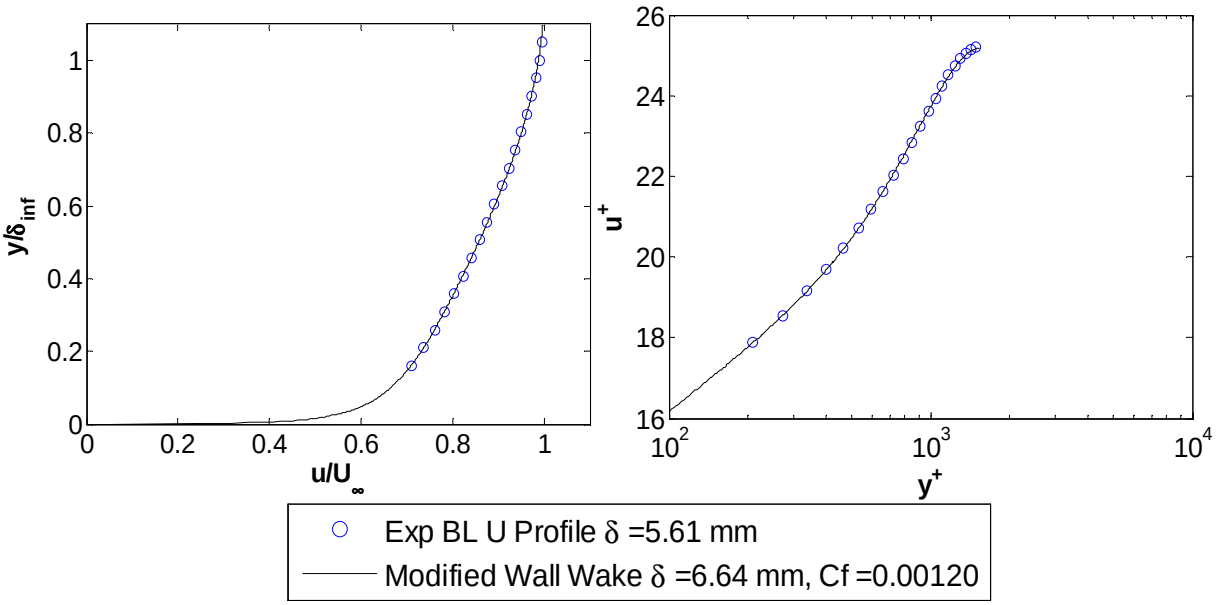

Fig. 2.8 Measured incoming boundary layer velocity profile compared to the fit for a modified wall wake velocity profile (Sun and Childs, 1973): (a) in normalized outer coordinates and (b) in wall coordinates.

µs. At this delay time the velocity in the jet is significantly reduced, to about 17 m/s, which is about 2.8% of the freestream velocity. By 70 µs the jet velocity has recovered the velocity it had prior to 60 µs and maintains this recovery until 100 µs. At 30 µs, 40 µs, 70 µs, and 90 µs there is a region of negative transverse velocity just behind the jet. This could be an indication that some vorticity is being introduced to the boundary layer; however, it is very weak and does not appear to propagate downstream. This negative transverse velocity region does not appear downstream of the jet at 20 µs, even though this is the time at which the maximum positive transverse velocity occurs, because the jet does not extend very far into the flow.

The weak Mach waves seen in the schlieren image of Fig. 2.7 at the jet orifice can also be seen in Fig. 2.10a. In Fig. 2.10a these waves are resolved into the series of waves at the front and back of the cavity insert in addition to the one at the jet orifice. These Mach waves induce a maximum transverse velocity of about 13 m/s, which is 2.1% of the freestream and a minimum transverse velocity of about -11 m/s, which is 1.8% of the freestream. While these Mach waves do not interfere with the PPJ, they do give an indication of the magnitude of the velocity effect that they have. At its weakest, the jet has an effect comparable to the Mach waves created just by the insert's joints, and even at its strongest, the effect of actuation is still modest.

A common measure of transverse jet strength is the momentum flux ratio, which compares the momentum flux of the jet to that of the freestream. This parameter could not be calculated for the PPJ

because the temperature inside the electrode cavity was not determined. Additionally, this parameter is generally used to characterize steady jets, and temporal changes are not considered. For this study, the peak velocity ratio was calculated for each time delay and for five different spatial regions above the jet orifice. These values are shown in Fig. 2.11a and the spatial regions are shown in Fig. 2.11b. The trend of fluctuation in jet strength is clearly observed, with peaks at 20, 40 and 80 µs. The peak near the orifice (Region 1) at 20 µs is about twice the size of any of the other peak velocities, but moving further away from the orifice, this ratio decreases rapidly. This is the only point that this behavior is seen; at the other time delays, the velocity ratio is much more consistent along the length of the jet, and the largest velocity is not in the region nearest the jet orifice. It is also useful to consider a jet-to-crossflow ratio based on the average velocity over the duration of the pulse and over all five regions. This velocity ratio is approximately 0.047, which indicates that overall the jet is weak and will have little influence on the flow, unless it is "tuned" to natural instabilities in the crossflow.

Table 2.1 Incoming Boundary Layer Properties

Quantity	Value
δ	5.61 mm
δ^*	0.942 mm
θ	0.697 mm
H	1.35
C_f	0.0012
Π	1.01

Another common measure of transverse jet strength is the penetration of the jet into the crossflow. The penetration of the jet was determined by plotting the contour of velocity equal to 16 m/s and finding the maximum height of the contour. The velocity for that contour was approximately the minimum transverse velocity induced by the jet (above the maximum transverse velocity of the no control case). The penetration heights for all the time delays are plotted in Fig. 2.12 (the contours are seen in Fig. 2.10). The jet penetration follows a slightly different pattern than the jet velocity; there is no peak at 20 µs, just one at 40 µs and one at 80 µs, with a minimum at 60 µs. These peaks are 1.25δ and 1.33δ, respectively, which is slightly lower than that observed by Grossman et al. (2003). However, that study was done at Mach number of 2.5, so it is reasonable that the jet penetration is lower in this Mach 3 case.

The 'chugging' behavior of the PPJ was also observed in simulations as well as other experiments. In simulations by Grossman et al. (2004), cyclic suction-expulsion behavior appeared within a single energy deposition cycle. About 400 µs after energy deposition, flow reversal occurred and fresh air was drawn back into the cavity. This air mixed with the hot air in the cavity and was expelled again, re-establishing choked flow at the orifice. This cycle was then repeated for the same energy deposition. While the timescale is much larger for this simulation than what is observed here experimentally, the

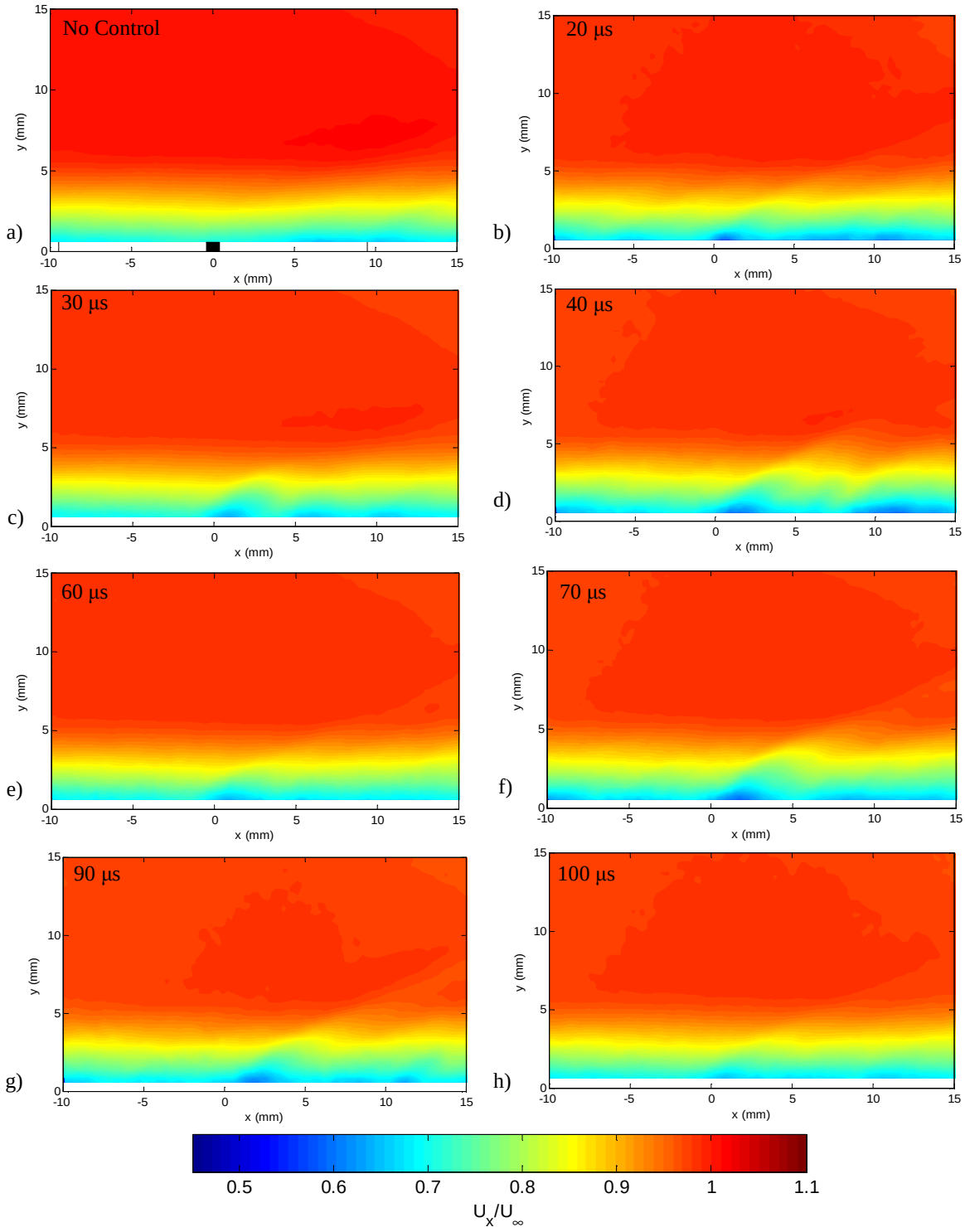

Fig. 2.9 Mean streamwise velocity normalized by the freestream velocity (a) for no control, (b) after 20 µs delay time, (c) after 30 µs delay time, (d) after 40 µs delay time, (e) after 60 µs delay time, (f) after 70 µs delay time, (g) after 90 µs delay time, and (h) after 100 µs delay time.

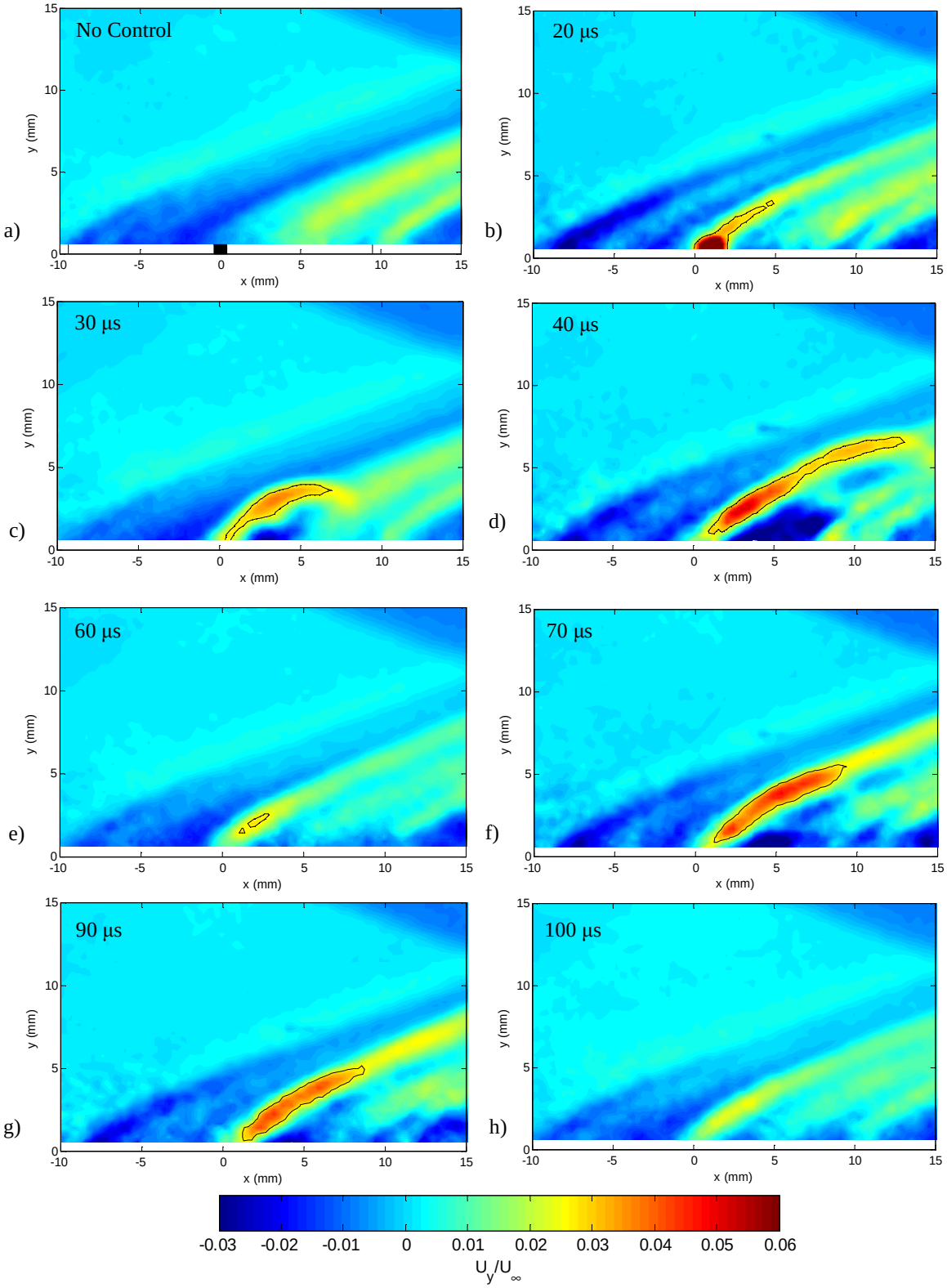

Fig. 2.10 Average transverse velocity normalized by the freestream velocity (a) for no control, (b) after 20 µs delay time, (c) after 30 µs delay time, (d) after 40 µs delay time, (e) after 60 µs delay time, (f) after 70 µs delay time, (g) after 90 µs delay time, and (h) after 100 µs delay time.

behavior is very similar. In the experiments done by Reedy et al. (2012), where the PPJ was exhausted into quiescent air, this behavior was observed again. For the 0.25 μF and 2 μF capacitors, the jet consisted of a series of discrete vortex rings. This could account for the fluctuating strength of the jet in this study, but it is more likely that the jet here is displaying behavior similar to that of the 25 μF case in quiescent air. In that case, there is a strong ring vortex exhausted initially, followed by a sustained jet, which peaks in strength, then drops off sharply, and then peaks again before slowly tapering off at the end of the pulse. This corresponds very well to the 2 μF case studied here; the maximum jet velocity, but small penetration at 20 μs is the initial strong vortex ring, and following this there is a sustained jet that fluctuates in strength. This behavior is believed to be caused by pressure wave dynamics inside the electrode cavity. Additionally, the greatly reduced pressure of the Mach 3 environment causes the 2 μF PPJ to display the same behavior only seen with the larger capacitor at ambient conditions. This is because the lower pressure and density conditions require less power for the gas to be heated to the same temperature, which is believed to be one of the main drivers behind the wave dynamics inside the cavity.

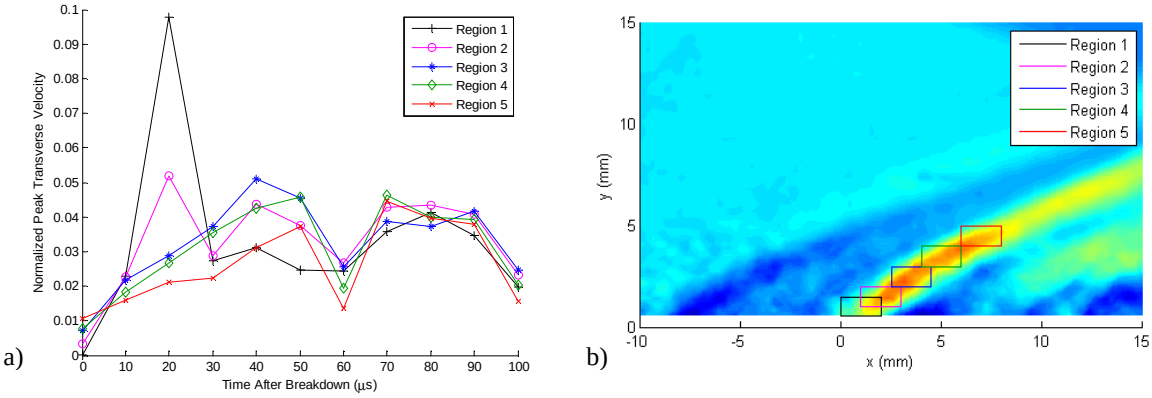

Fig. 2.11 (a) Peak transverse velocities in five regions above the jet orifice for each time delay and (b) the regions in which the peak velocities were found.

Although the transient behavior of the PPJ under Mach 3 crossflow conditions is consistent with that in quiescent air, the peak jet velocities are much, much lower. The peak jet velocities that were found by Reedy et al. (2012) were 130 m/s, 320 m/s, and 495 m/s for the 0.25 μF, 2 μF, and 25 μF cases, respectively, for the ambient case. The peak velocity observed in this study, 61 m/s, is much lower than all of these velocities; it is just under half the velocity of the weakest case in quiescent air. This is partly due to the strength of the crossflow and its 'resistance' to the transverse jet. However, some of this reduction in peak jet velocity is also due to the lower density of the Mach 3 environment; there is simply less mass that can be forced out of the cavity.

Narayanaswamy et al. (2010) also investigated a pulsed plasma jet, but of a slightly different design. In that study the PPJ was also placed in a Mach 3 crossflow and additionally in a vacuum

chamber with pressure and density conditions similar to that of the crossflow. In the crossflow, a jet penetration of 1.5δ was observed; this is somewhat higher than what was found in this study. Additionally, in the vacuum chamber, the velocity of the contact surface was found to be about 250 m/s, which is the upper limit on the fluid velocity in the jet. This is much higher than the jet velocity found in this study; it is more comparable to that found in Reedy et al. (2012). The discrepancy is most likely due to the differences in cavity design; the cavity in the current work was about eight times larger than the one studied by Narayanaswamy et al. (2010), and the orifice was about half the size. However, it is not known how much these factors influence the jet.

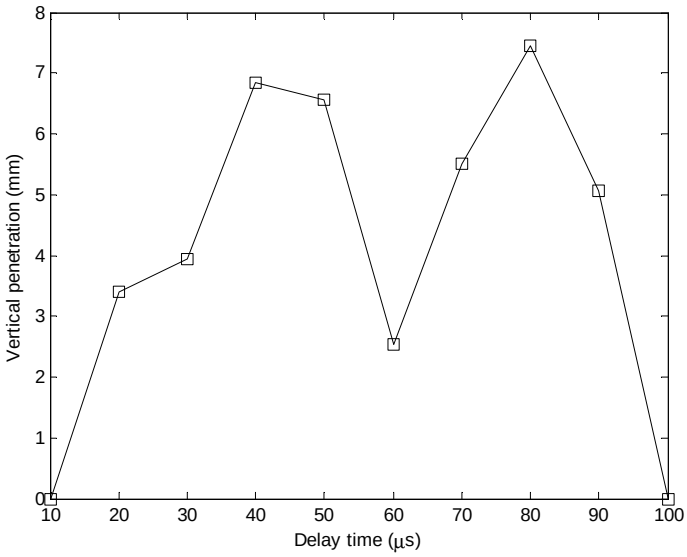

Fig. 2.12 Vertical penetration of jet into crossflow for each delay time.

Figure 2.13 shows the Reynolds shear stress, normalized by freestream velocity squared, for the no control, 30 μs, 60 μs, and 100 μs delay cases. The bow shock that is created in front of the jet can be seen for the cases with the PPJ on. It is strongest at 30 μs, which is consistent with the jet being strongest at that time, out of the cases shown. What is more interesting, however, is that right behind the shock in those cases, the shear stress is slightly positive. This phenomenon is weakest at 30 μs, where the jet velocity is largest and strongest at 60 μs and 100 μs, where the jet velocity is significantly smaller. This indicates that there is some backflow and possibly that the cavity is refilling at these times.

2.4 Conclusions

A pulsed plasma jet was exhausted transversely into Mach 3 crossflow, and single pulses were examined to determine their effect on the boundary layer and the flow in general. Particle image

velocimetry and voltage measurements were obtained to measure these effects. The PPJ was found to have a modest effect on the flow; the largest peak jet velocity was 9.8% of the freestream velocity, and

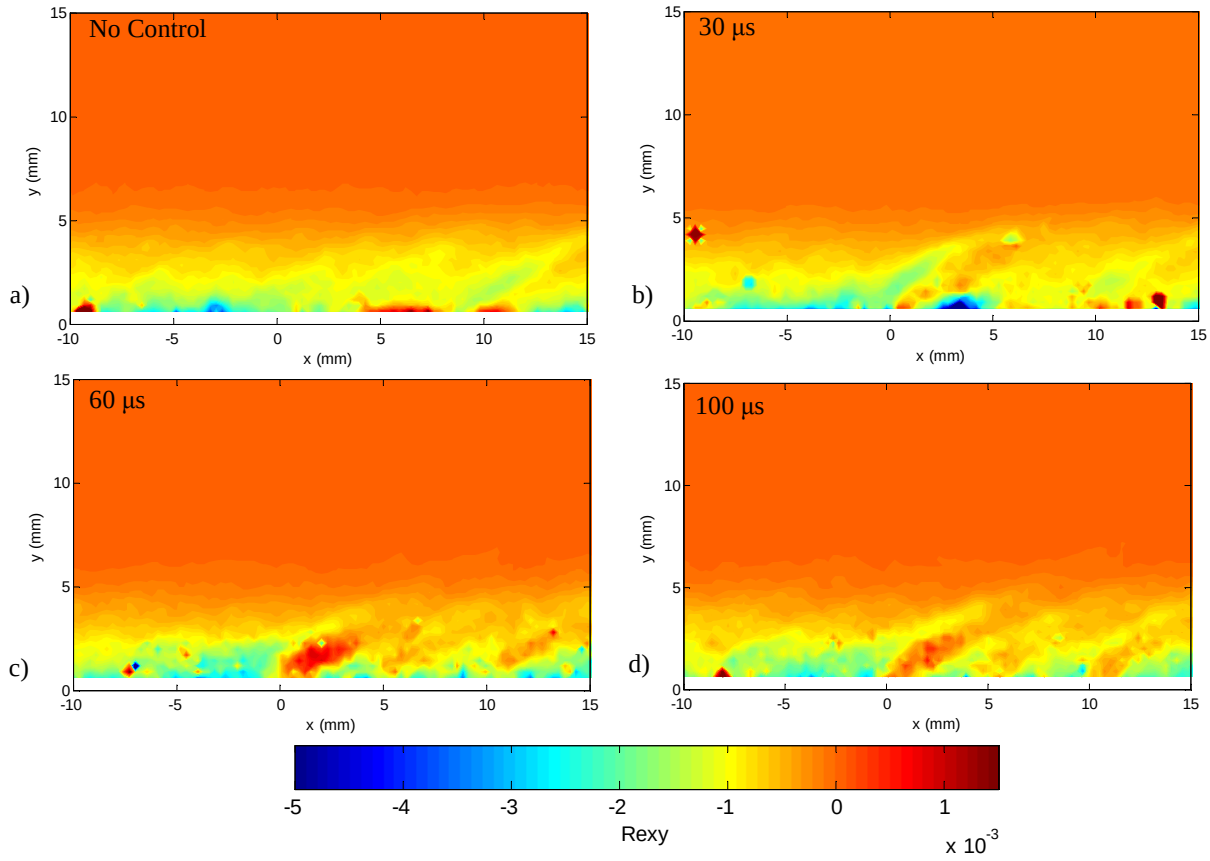

Fig. 2.13 Reynolds shear stress normalized by the freestream velocity (a) for no control, (b) after 30 µs delay time, (c) after 60 µs delay time, and (d) after 100 µs delay time.

the average peak jet velocity was about 4.7% of the freestream velocity. The low jet velocities caused weak disturbances in the streamwise velocity and weak bow shocks in front of the jet. Additionally, the jet was observed to fluctuate in strength over the course of a single pulse, which is consistent with the behavior of the jet exhausted into quiescent air. However, the jet velocities are much lower in the Mach 3 case than for the quiescent case. Some of this is due to the velocity of the crossflow and some of it is due to the reduced pressure and density in the Mach 3 environment. The relative magnitude of these two influences is not known. Due to the modest effect of the PPJ, it may be necessary to tune it to frequencies that induce natural instabilities in the flow.

3. Localized Arc Filament Plasma Actuators (LAFPAs)

3.1 Introduction

The localized arc filament plasma actuator studied here is based on an actuator design developed at the Ohio State University (Samimy et al., 2004). This actuator was designed to overcome some of the limitations of glow discharge-type actuators which were discussed in Chapter 1. Glow discharge actuators have many advantages such as no moving parts, no additional plumbing, a very fast response time, are operable at high frequencies, etc. However, they have some disadvantages that limit their usefulness. They rely on EHD forces which produce relatively weak effects, especially when the external flow velocity is large; this is most likely due to Joule heating effects counteracting the EHD mechanism. Additionally, when the current rises above a certain threshold, the glow discharge becomes unstable and transitions to an arc. LAFPA actuators seek to sidestep these issues, while maintaining the advantages, by using an arc discharge and using Joule heating as the driving mechanism. Joule heating from the arc discharge causes rapid, localized heating and a subsequent pressure rise, which acts as a virtual obstacle abruptly placed in the flow (Samimy et al., 2004).

LAFPAs consist of two electrodes separated by a small air gap. One electrode is grounded and the other is connected to a high voltage power supply, and both electrodes are recessed from the surface in either a small cavity or groove, to prevent the plasma from being blown off by a crossflow. In order to create the arc discharge, the voltage is ramped up until the arc discharge is formed between the two electrodes. In general, a few kilovolts are needed for the initial electric breakdown, but once the arc is initiated, the voltage needed to sustain it is much lower, on the order of hundreds of volts (Utkin et al., 2007; DeBlauw et al., 2011). High- resolution spectroscopy was done by Sanders (2012) to determine the emission and temperature characteristics of the LAFPAs. It was found that while emission intensity was highest at the beginning of a pulse, the rotational and vibrational temperatures increased over the entire duration of the pulse, and thus the Joule heating effects are actually stronger later in the pulse. Additionally, there is substantial variation in the rotational, vibrational, and electronic temperatures during the pulse, especially at the beginning, which indicates a high degree of non-equilibrium. The velocity field induced by the LAFPAs when operated in quiescent air has also been characterized. It was found that a blast wave is initially created by the actuators, and this is followed by a plume of hot gas. The maximum outward velocity induced by the actuators is on the order of tens of m/s, and operation at lower frequencies produces higher outward velocities. This suggests that the cavity containing the electrodes needs some time to adequately refill between pulses (DeBlauw et al. 2011).

It has been proposed that there are two ways that the LAFPAs interact with and control a flow. The first is that when the actuators are operated at a relevant flow frequency they can excite natural flow

instabilities. Exciting flow instabilities by forcing at certain frequencies has been shown to be particularly effective for controlling jets. For example, acoustic excitation and vibrating ribbons have been used successfully to suppress turbulence in both circular and plane jets, especially when operated at a preferred Strouhal number (Zaman and Hussain, 1981). Thus, it was a natural step to use the LAFPAs to control jets. They are particularly appealing for this application because they can be operated at very high frequencies, enabling them to match the instability frequencies of even high-speed jets, and they have the additional capability of operating at various azimuthal modes. When placed around the exit of Mach 0.9 and Mach 1.3 axisymmetric jets, forcing the jets caused the turbulent structures to become very well organized in space as well as in time, and the length of the jet potential core was significantly reduced. These effects are optimal when the actuator is operated at the jet preferred frequency (which corresponds to a Strouhal number, based on jet exit diameter, of approximately 0.3) and in the $m = \pm 1$ flapping mode, i.e., the top actuators and the bottom actuators are operated at the same time, but 180° out-of-phase with each other (Samimy et al., 2007; Utkin et al., 2007).

The second way the LAFPAs act on a flow is as 'virtual' vortex generators which impart some momentum to the boundary layer, thus making it 'healthier' and less prone to separation. Vortex generators, such as micro-ramps, split ramps, and ramped vanes, have been shown to be effective passive control devices for normal shock/boundary-layer interactions (SBLIs). Pairs of counter-rotating vortices are formed at the trailing edge of the vortex generators, and as they move downstream, they draw higher-momentum fluid into the boundary layer. This thickens the boundary layer, but makes it more resistant to separation and also helps with pressure recovery (Herges et al., 2010; Rybalko et al., 2012). Recently, LAFPAs have been applied to similar SBLIs. In addition to them acting as virtual vortex generators, it was hoped that their periodic operation would allow them to excite or suppress natural instabilities in the shock/boundary-layer interaction. Caraballo et al. (2009) found that when the LAFPAs are placed upstream of the shock, the velocity in the boundary layer near the wall is increased, with the strongest effect occurring at a Strouhal number of 0.03. This is approximately the Strouhal number at which the upstream leg of the lambda shock structure oscillates (Dupont et al., 2006). Further study of the LAFPAs' control over an SBLI showed that the most noticeable effect was a slight shifting of the reflected shock upstream by about one boundary layer thickness. Frequency and location of the actuators had negligible influence on the effectiveness of the LAFPAs but duty cycle (duration of actuator on time) did. This suggests that the LAFPAs do not work through an instability, but actually heat the boundary layer going into the SBLI. This increases the size of the separation bubble downstream of the SBLI, which pushes the reflected shock upstream (Webb et al., 2012; Webb et al., 2013).

The current work continues to investigate the control authority of the LAFPAs by observing their effects on the boundary layer of a Mach 1.4 crossflow. Additionally, the effects of the actuators on the

stability of a normal shock is studied, as well as their effects on a separated boundary layer. Schlieren and PIV measurements are both used to investigate these effects and are reported in the following sections.

3.2 Experimental Set-Up

3.2.1 Wind Tunnel Facility

The same supersonic blowdown wind tunnel facility described earlier (section 2.2.1) for the PPJ experiments was used here for the LAFPA experiments, but with a few modifications. First, the Mach 3.0 nozzle was replaced with a nozzle designed for Mach 1.4 flow, and a 5° diffuser was installed at the end of the test section. The tunnel stagnation pressure for these experiments varied, in order to vary the shock position, from 127.6 to 172.4 kPa, while the total temperature was 303 K and the unit Reynolds number was 26×10^6 m^{-1}. Additionally, the floor of the tunnel was modified to accommodate an insert housing the LAFPAs, which was placed at two different positions, as shown in Fig. 3.1. Figure 3.1a shows the LAFPA insert 95.5 mm upstream of the ramp corner; this position was used to observe the LAFPAs' effects on the unseparated boundary layer. Figure 3.1b shows the LAFPAs centered (in the streamwise direction) on the corner; this position is the "receptivity region," the region that will be most receptive to the introduction of periodic instability excitation. This will also allow observation of the LAFPAs' effects on a separated boundary layer.

a) 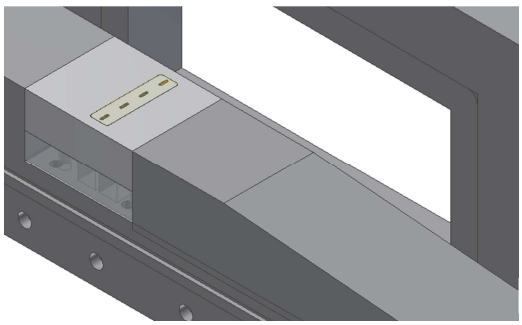 b) 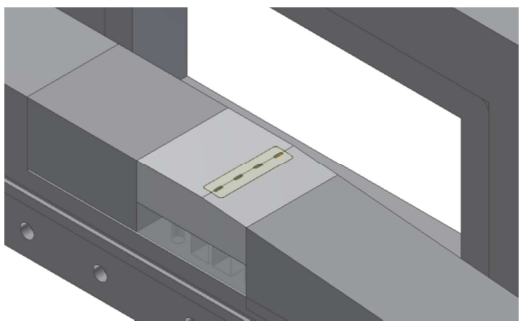

Fig. 3.1 LAFPA array positions a) 95.5 mm upstream of the 5º ramp and b) centered on the corner of the 5º ramp.

The pressure transducers used previously were also replaced with a Measurement Specialties Inc. NetScanner System Intelligent Pressure Scanner module, model 9016. Two channels were used to measure test section static pressure, one at the upstream end and one at the downstream end of the test section, and a third was used to measure the tunnel stagnation pressure. The module was re-zeroed and calibrated daily using the internal calibration manifold, and its accuracy is ±0.05% of full-scale.

3.2.2 LAFPAs

The LAFPA system used here is very similar to the design used by Utkin et al. (2007) for the control of high-speed jets. The actuators are composed of two tungsten electrodes 1 mm in diameter, placed in a small cavity (5.842 mm by 1.778 mm by 1.778 mm). The electrodes tips are ~3 mm apart. Four actuators were used, spaced evenly across the span of the tunnel, 13.881 mm apart, center-to-center, and this array is shown in Fig. 3.2. The actuator cavities were machined into a boron nitride insert, which was housed in an aluminum and plexiglass block and placed in the tunnel.

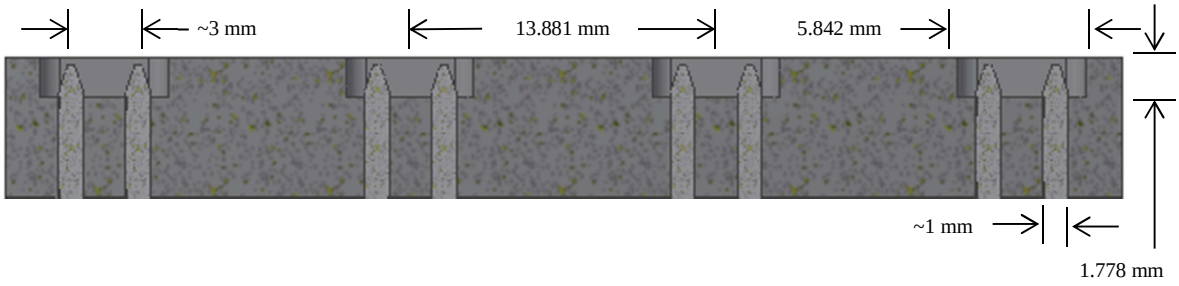

Fig. 3.2 Schematic of the LAFPA cavities and array.

A Glassman High Voltage, Inc. 10 kV, 1 A DC power supply was used to generate the high voltage. Four actuators are powered by the power supply so that each actuator can be supplied with up to 0.25 A. A ceramic, 15 kV, 1 nF, TDK Electronics FD-12AU capacitor is used to buffer the power supply

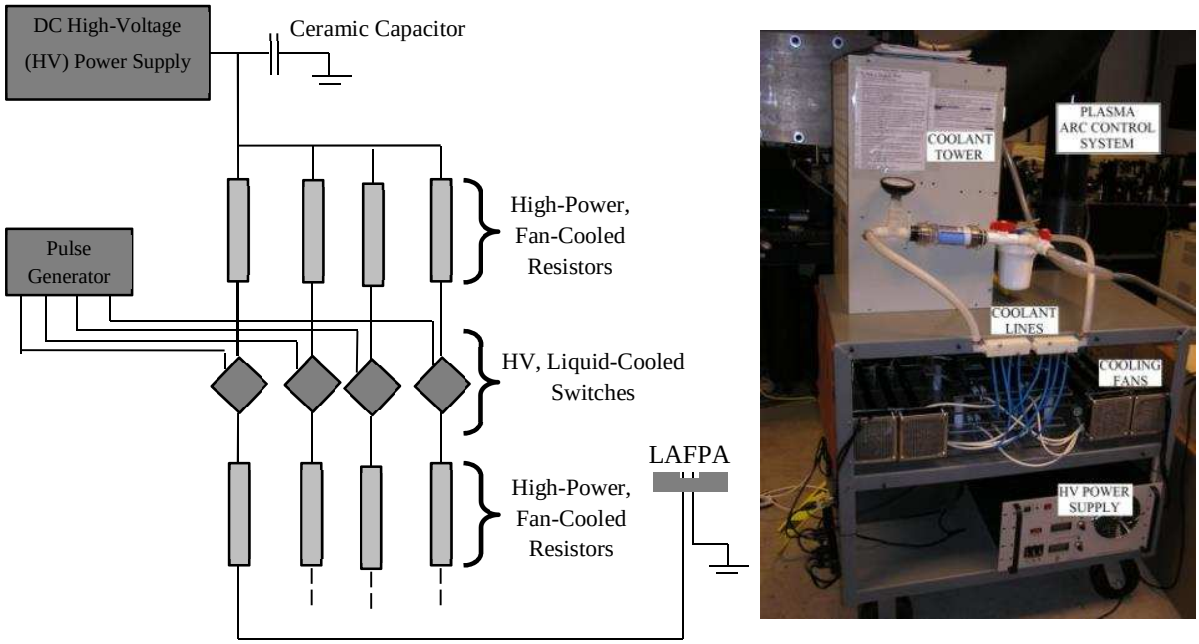

Fig. 3.3 a) Schematic of LAFPA circuit and b) photo of LAFPA control system (DeBlauw et al., 2011)

and assists in providing peak current above 1 A for short durations. Each actuator is individually controlled by a liquid-cooled, high-voltage Behlke MOSFET switch, which is capable of pulsing at

frequencies up to 200 kHz with pulse-widths as short as 0.1 ns. For each actuator, two high-power, solid-body 3750 kΩ ballast resistors are used in series, one on each side of the switch, to regulate the load on the power supply. A schematic of the circuit and a photo of the system are shown in Fig. 3.3. A Quantum Composers pulse generator with controllable TTL outputs is used to control each switch individually. In order to reduce electromagnetic interference, the pulse generator was optically isolated from the LAFPA circuitry, and any low voltage-carrying BNC was wrapped in aluminum foil and grounded. Detailed descriptions and operational and safety procedures are given in Reedy (2013), Kale (2013), and DeBlauw (2012).

Voltage and current traces were obtained using an Agilent N2771A high-voltage probe and a Pearson Current Meter model 4100, respectively, and were recorded using a Picoscope 4424 PC Oscilloscope. An average voltage of about 4.5 kV was required for the LAFPAs to break down, although there was significant variation in the required breakdown voltage. As expected, the current was sustained at about 1 A over the duration of the breakdown. Average and instantaneous voltage and current traces for a sample case (frequency of 8 kHz, on-time of 12 μs) are shown in Fig. 3.4.

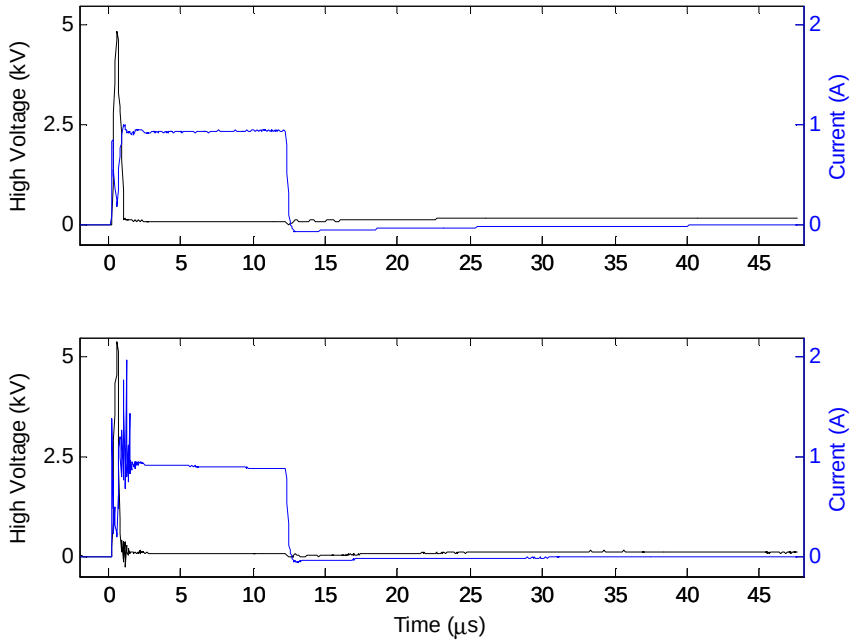

Fig. 3.4 Average (top) and instantaneous (bottom) voltage and current traces for a single LAFPA, operated at a frequency of 8 kHz and with an on-time of 12 μs.

3.2.3 Diagnostics

3.2.3.1 Schlieren Imaging

Schlieren imaging was used to characterize the baseline flow and to determine the LAFPAs' effect on the stability of the normal shock. A typical Z-type arrangement was used consisting of two

7.625” diameter parabolic mirrors with focal lengths of 63.625” and 64” and a horizontally oriented knife edge, shown in Fig. 3.5. The light source was a Xenon Corp. M-437B Nanopulser, which had a spark duration of approximately 20 ns. The camera was a Cooke Corporation PCO 1600 (1600 x 1200 pixel) CCD with a C-mounted Nikon Nikkor 70-300 mm zoom lens. Phase-locked images were obtained without LAFPA operation (no control) and at various time delays after the arc was initiated. A Stanford Research Systems Inc. delay/pulse generator was used as a master to control the pulse generator controlling the LAFPAs, as well as the camera and the light source. This allowed the LAFPA forcing frequency to be varied and the image sampling frequency to be kept at 10 Hz.

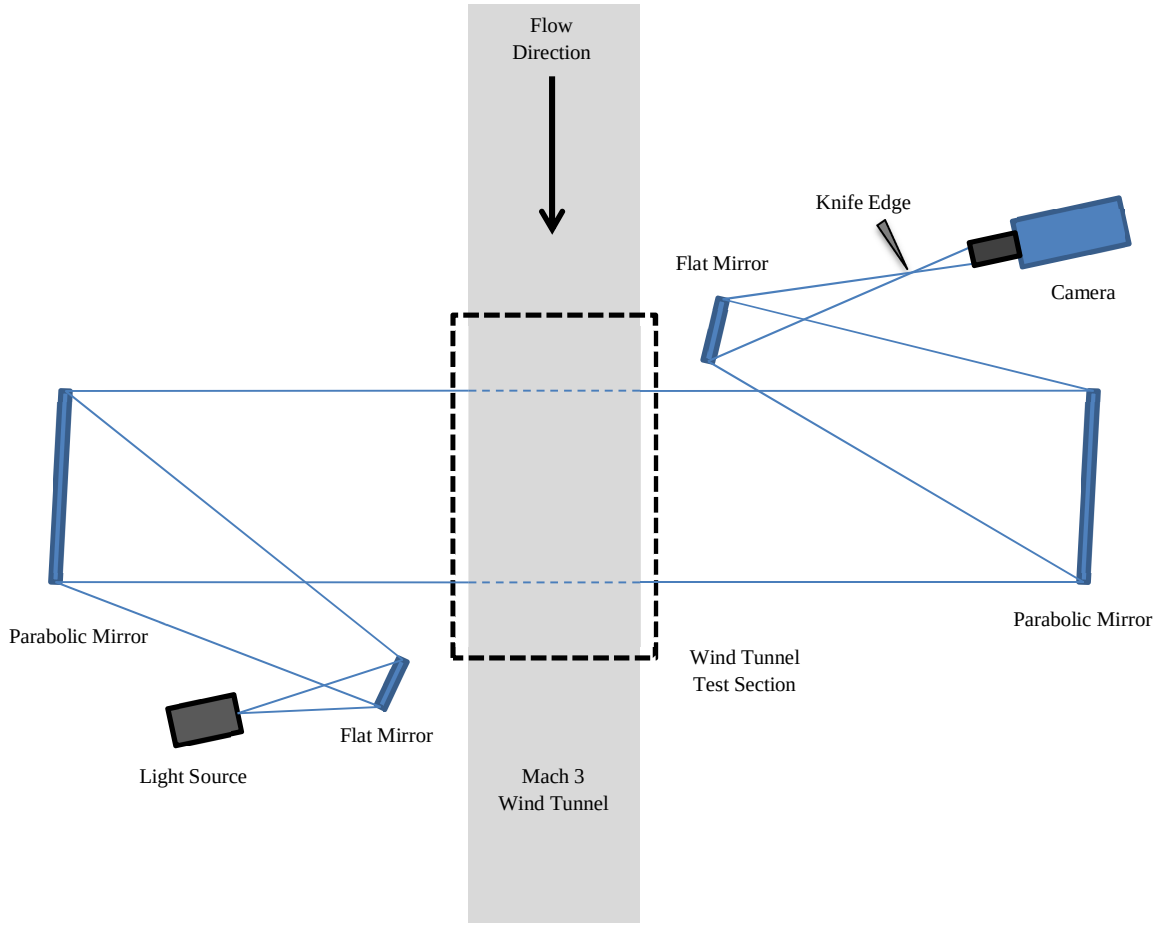

Fig. 3.5 Schematic (not to scale) of Schlieren Z-type optical configuration.

3.2.3.2 PIV

PIV was used to determine the effect of the LAFPAs on the Mach 1.4 crossflow boundary layer, both before and after separation. The same camera, laser, and optics used for the PPJ experiments were used again, and are shown in Fig 3.6a, with the dotted laser sheet and camera indicating the position of those devices for the cases with the LAFPAs on the corner). The most significant difference in the PIV set up is that the laser sheet was moved to the spanwise center of one of the actuators, which is offset from

the tunnel spanwise center, as shown in Figs. 3.6b and 3.6c for the two actuator locations. A Laskin nozzle was used to introduce seed, made of diethylhexyl sebacate (DEHS), into the flow upstream of the

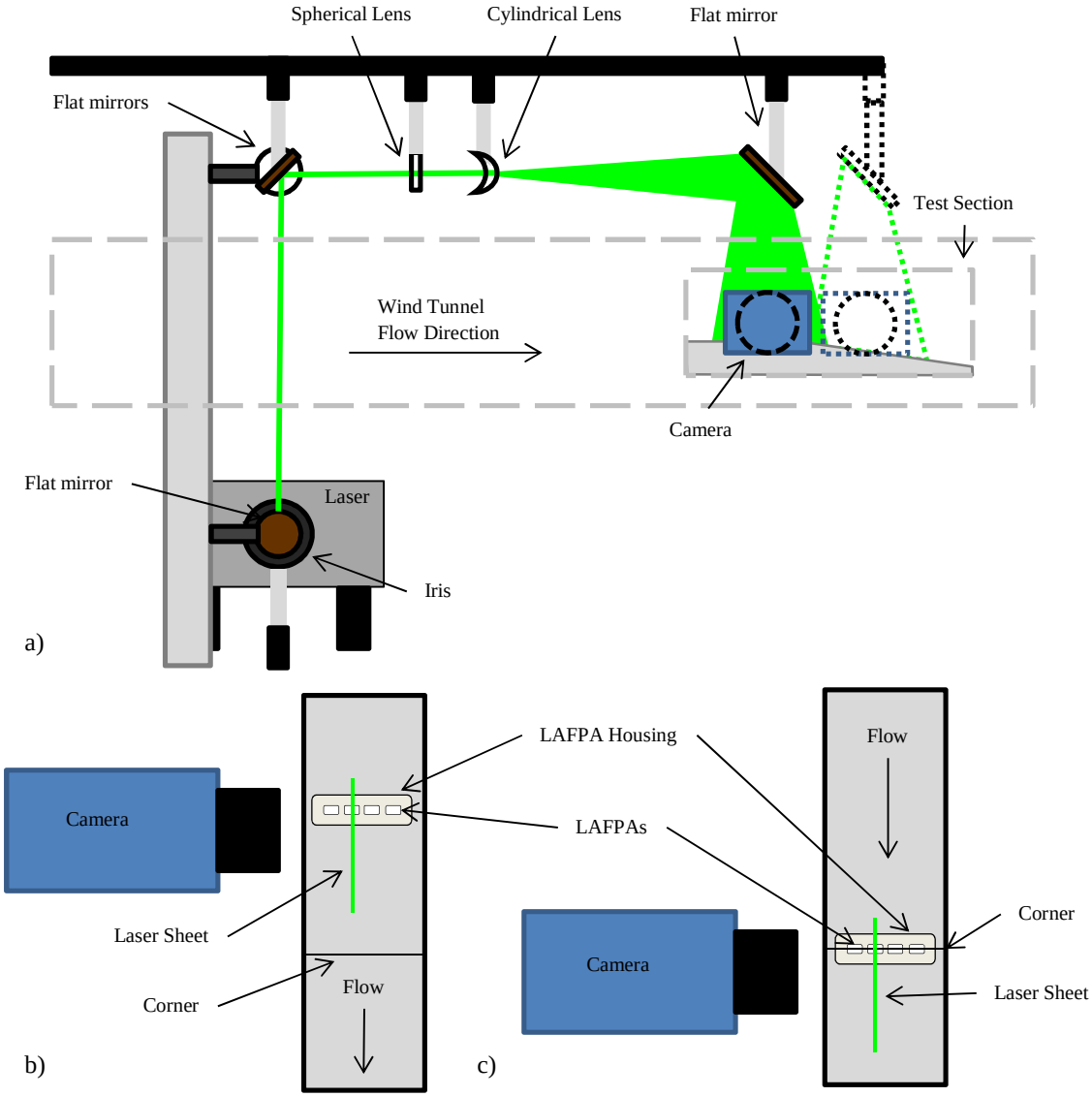

Fig. 3.6 Schematic (not to scale) of PIV a) optical set up (dotted lines indicate laser sheet and camera position for LAFPAs on the corner), b) laser sheet position for LAFPAs upstream of the corner, and c) laser sheet position for LAFPAs on the corner.

stagnation chamber. The particles are approximately 0.8 μm in diameter and have a Stokes number of 0.16, which indicates that the particles are capable of tracking the flow well (Samimy and Lele, 1991). Phase-locked images were acquired for no actuation as well as at various delay times after the arc was initiated. Similar to the Schlieren imaging system, a master pulse generator was used to control the pulse

generator controlling the LAFPAs, the laser, and the camera, so that the LAFPAs could be operated at various frequencies, while the image acquisition rate was kept at 10 Hz.

The PIV image pairs were analyzed using LaVision DaVis 8.1 analysis software. Similar to the PPJ experiments, the particle displacements were determined using multi-pass, cross-correlation calculations using 50% interrogation region overlap. For these experiments, the initial interrogation regions were 32 x 32 pixels and the final passes were 16 x 16 pixels. Post-processing was applied to the resulting vectors, including filtering, using a minimum peak ratio, Q, of 1.7 to remove bad vectors.

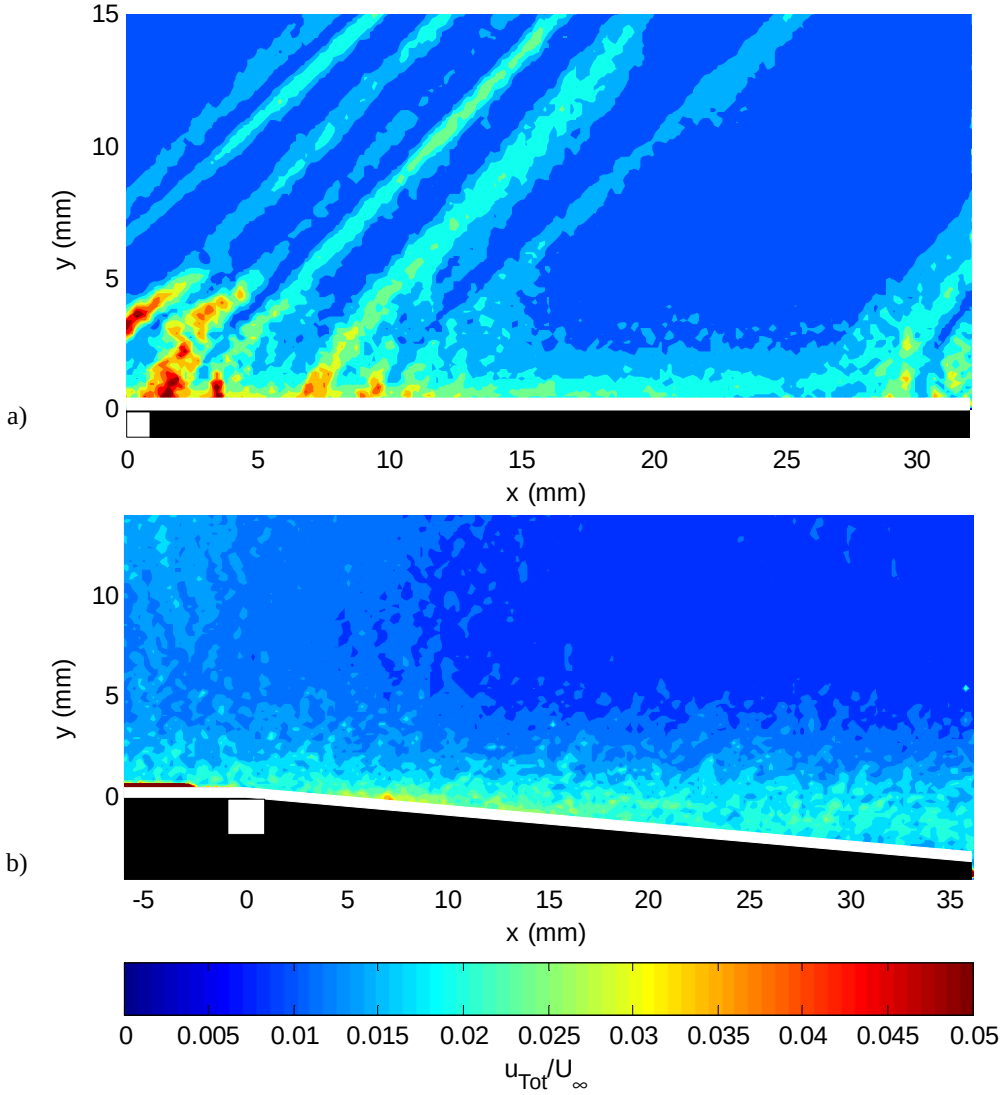

Fig. 3.7 Total uncertainty for two representative cases, a) for the boundary layer study, 1 kHz at 20 µs, and b) for the separation region study, 2 kHz at 60 µs.

A conservative analysis of the uncertainty of the PIV measurements was again made using the method described by Lazar et al. (2010). Two representative cases are shown in Fig. 3.7. Figure 3.7a

shows the total uncertainty in the measurements of the boundary layer before separation (for the case of a frequency of 1 kHz and a delay of 20 μs after plasma initiation), and Fig. 3.7b shows the uncertainty of the separated boundary layer in the diffuser (for the sample case of a frequency of 2 kHz and a delay of 60 μs after plasma initiation). For the boundary layer investigation (upstream of the diffuser corner), the average total uncertainty was about 1.5% of the freestream velocity, although areas of high velocity gradient and areas with reduced seeding (the boundary layer) had uncertainties up to 8% of the freestream, for some cases. For the separation region, the average uncertainty was about 1.5% of the freestream velocity, although the uncertainties got as high as 10% of the freestream, for some cases. The uncertainty of the PIV measurements for the boundary layer is slightly larger than that of the separated region, and this is partly due to differences in the processing, but is mostly due to better seeding and image quality for the separation region cases. Overall, the uncertainty is fairly low and the data represent the actual flow well.

3.3 Results

3.3.1 Shock Stability

Schlieren imaging was used to study the effects of the LAFPAs on the stability and position of the normal shock; both LAFPA positions (upstream of and centered on the corner) were examined. There are two mechanisms that are believed to drive the shock unsteadiness; one is the state of the incoming boundary layer, and the other is natural fluctuations in the separated flow behind the shock. Data support both of these mechanisms as potential causes of the low-frequency oscillation of the shock; however, it is likely that a combination of the two effects is responsible (Dupont et al., 2006; Clemens and Narayanaswamy, 2009). The LAFPAs were operated over a range of frequencies in an attempt to excite either of these sources of unsteadiness. The frequency of 333 Hz, which corresponds to a Strouhal number of 0.03 for this flow, was more closely examined because this is the Strouhal number that has been associated with the low-frequency oscillation of shock/boundary layer interactions, and there is some evidence that suggests the LAFPAs are effective at this Strouhal number (Dupont et al., 2006; Caraballo et al., 2009).

A sample of instantaneous schlieren images obtained with the LAFPAs in their upstream position can be seen in Fig. 3.8. The corner and the normal shock can be seen in the no-control image (Fig. 3.8a), and additionally the start of the secondary shock train can be seen, indicating that the flow after the normal shock is transonic. Mach waves from both joints in the tunnel and from the LAFPA cavities can also be seen; these Mach waves are weak and have minimal influence on the flow. In Figs. 3.8b-e, at various delay times after the LAFPA pulse, the blast wave created by the operation of the LAFPAs can be

seen moving outwards and downstream while also becoming weaker. In this case the LAFPAs were operated at a frequency of 333 Hz. Figure 3.9 shows the LAFPAs at the corner, at the same delay times

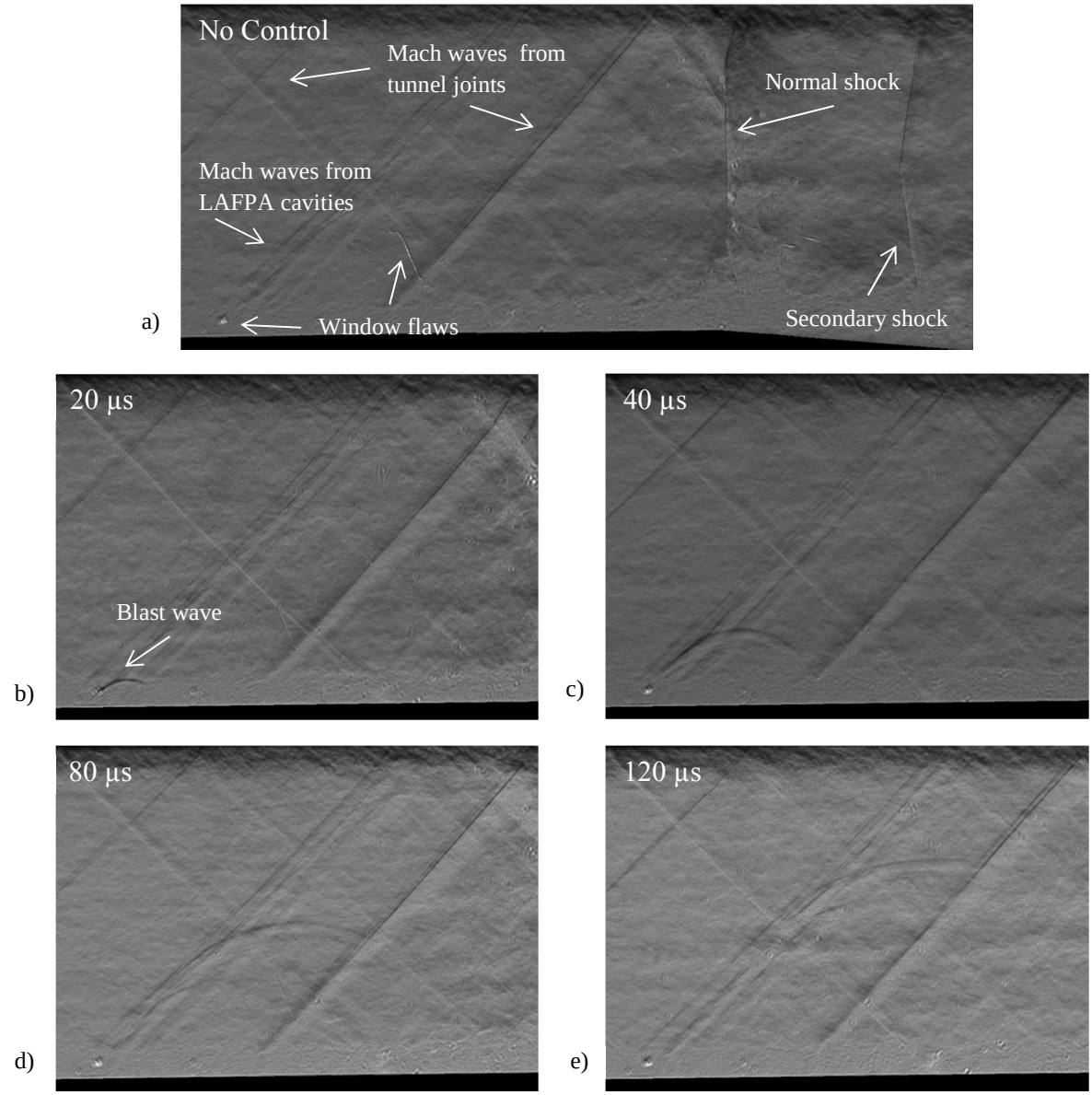

Fig. 3.8 Schlieren images with the LAFPAs in the upstream position for a) no Control, b) 20 µs, c) 40 µs, d) 80 µs, and e) 120 µs delays, all at a frequency of 333 Hz.

and frequency as in Fig. 3.8, but with the shock upstream of the LAFPAs and the corner. The blast wave exhibits the same behavior as in the previous figure; however, it appears to be slightly weaker in the transonic region behind the normal shock.

The nominal position of the normal shock is determined by the ratio of the tunnel stagnation pressure to exit pressure. However, there is a large amount of unsteadiness in the shock position even at a

nominally constant pressure ratio. To determine if the actuators could be used to improve the stability of the normal shock, two pressure ratios for each LAFPA position were examined. The shock location was

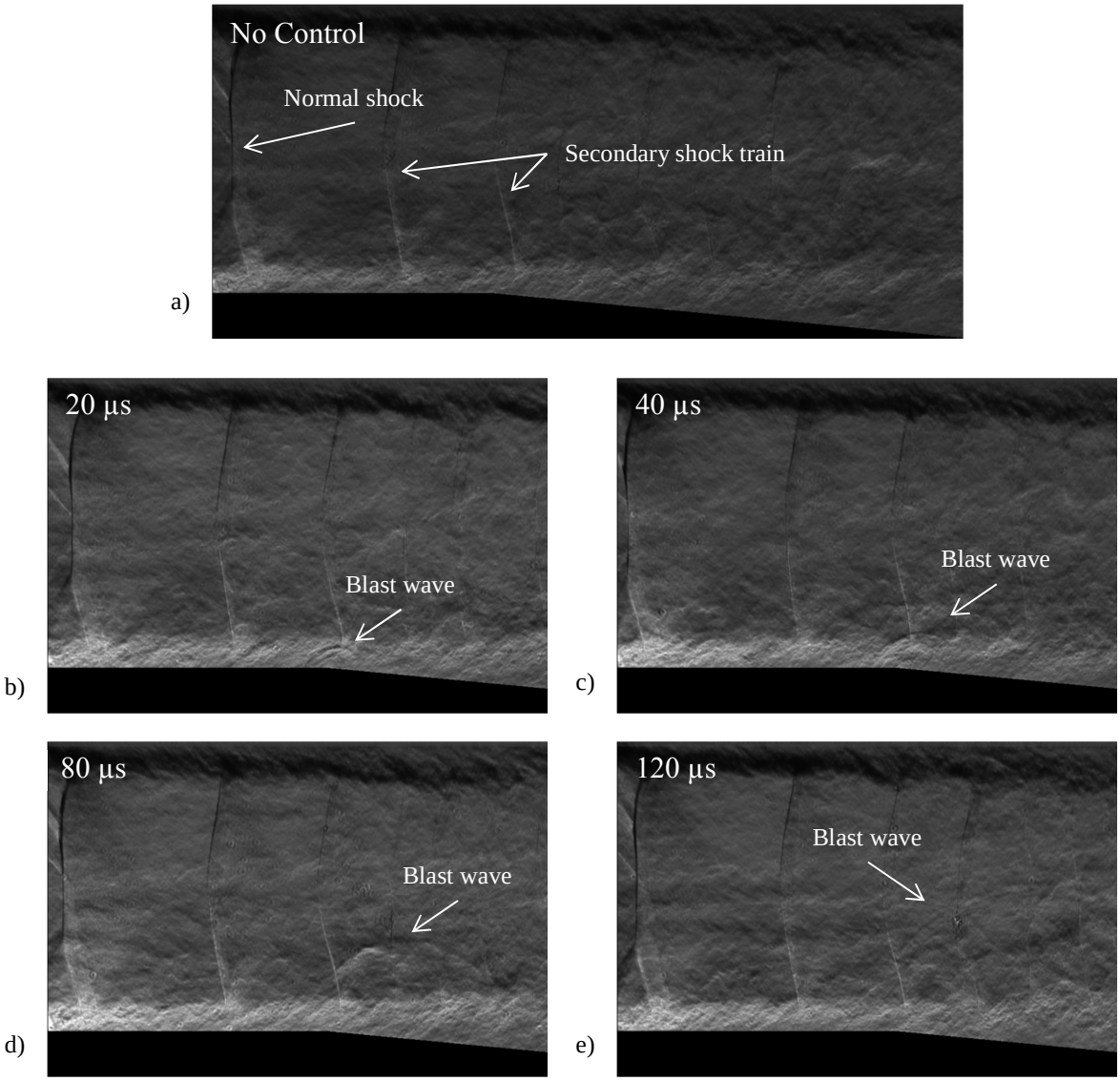

Fig. 3.9 Schlieren images with the LAFPAs at the corner for a) no control, b) 20 μs, c) 40 μs, d) 80 μs, and e) 120 μs delays, all at a frequency of 333 Hz.

determined for each image, and then the mean location for each pressure ratio was found. Figure 3.10 shows the mean and standard deviation of the shock location for the LAFPAs at the upstream position, for multiple frequencies (Figs. 3.10a-b; low frequencies highlighted in Figs. 3.10c-d) and delay times (Figs. 3.10e-f). The bars represent one standard deviation of the shock position (which is also displayed in the plots in the right column), the blue line represents a stagnation-to-exit pressure ratio of 1.37 (mean position of the shock on the corner), and the black line represents a stagnation-to-exit pressure ratio of

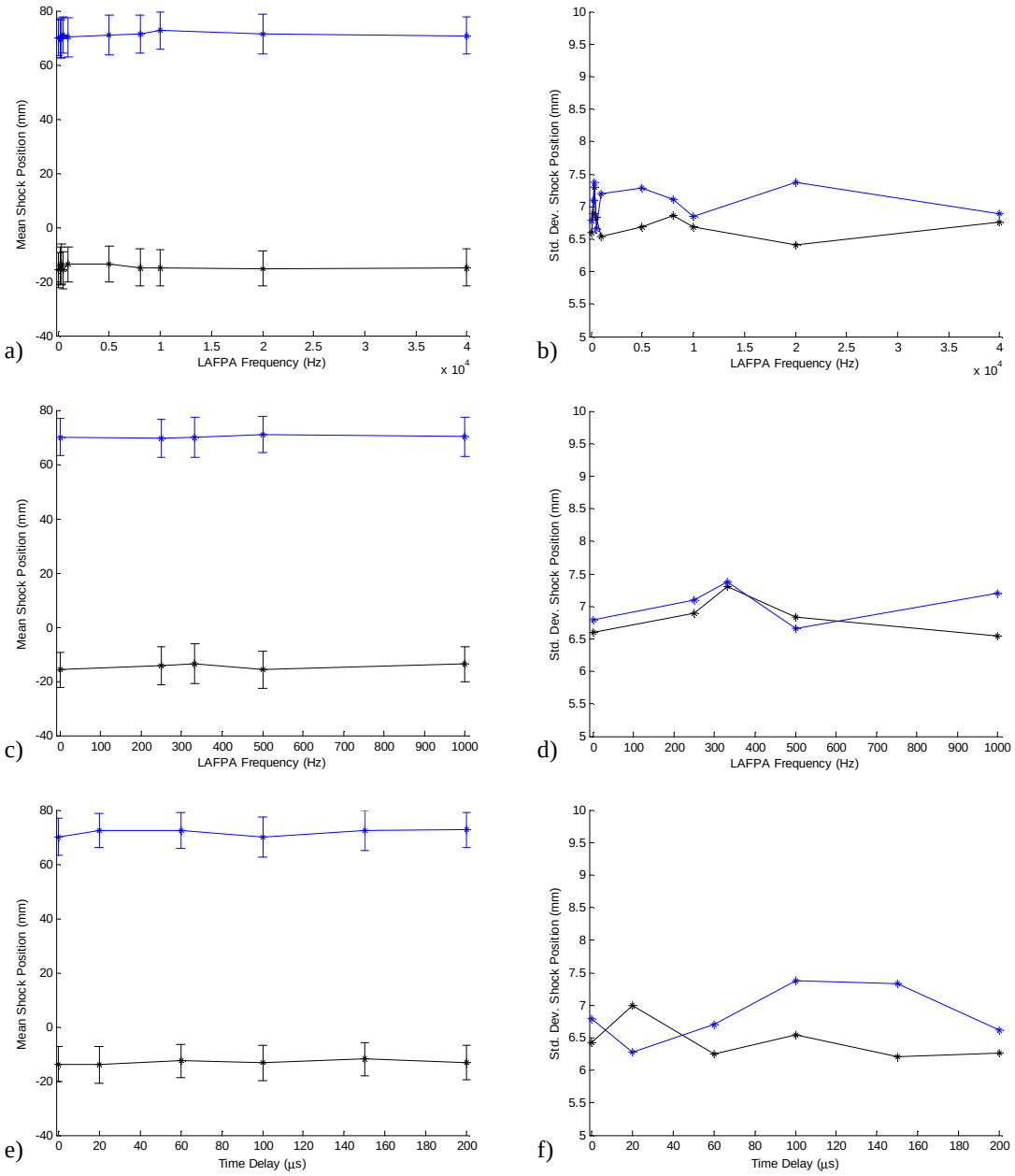

Fig. 3.10 Mean and standard deviation of shock location for two stagnation-to-exit pressure ratios (black is 1.31 and blue is 1.37), with the LAFPAs at the upstream position a-b) over all the frequencies studied, c-d) over the lower frequencies, all at a time delay of 100 μs, and e-f) over various time delays, all at a frequency of 333 Hz.

1.31 (mean position of the shock is upstream of the corner, on the LAFPAs). Neither the mean shock position nor the standard deviation appears to be significantly influenced by the LAFPAs at any frequency or at any delay time. There are some small differences in mean shock position, but these are

well within one standard deviation of the position with no control. In addition, the variability of the shock position doesn't appear to be affected by the LAFPAs, as can be seen in the plots of standard deviation.

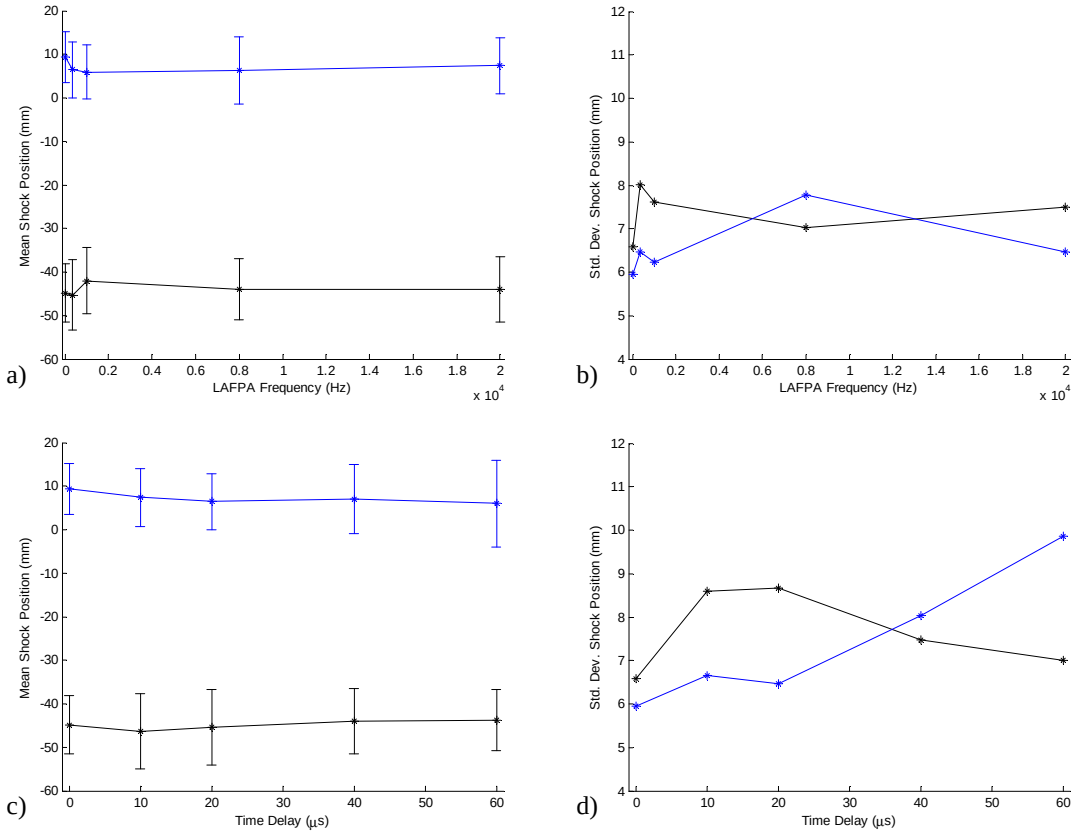

Fig. 3.11 Mean and standard deviation of shock location for two stagnation-to-exit pressure ratios (black is 1.32 and blue is 1.35), with the LAFPAs at the corner, over a-b) various frequencies, all at a time delay of 20 μs and c-d) various delay times, all at a frequency of 333 Hz.

The mean and standard deviation of the shock location for the LAFPAs at the corner are shown in Fig. 3.11 at various frequencies (Figs. 3.11a-b) and various delay times (Figs. 3.11c-d). For this LAFPA location, the blue line represents a stagnation-to-exit pressure ratio of 1.35 (mean position of the shock at the corner) and the black line represents a stagnation-to-exit pressure ratio of 1.32 (mean position of the shock upstream of the corner). At the higher pressure ratio, the LAFPAs appear to push the shock slightly upstream compared to the no-control case. However, similar to the other LAFPA position, the differences in shock position are well within one standard deviation of the mean location with no control. Thus, it is unlikely that this difference in shock position is due to the LAFPA actuation and rather is just a natural variation in run-to-run shock position. Again, the RMS in shock position fluctuations is virtually unaffected by the LAFPA operation.

3.3.2 Supersonic Boundary Layer

Phase-locked PIV was used to study the LAFPAs' effects on the supersonic boundary layer, far upstream (3.758") of the 5° corner. In order to see the effects, the stagnation-to-exit pressure ratio was maintained at approximately 1.71, so that the shock was far downstream of the actuators and the corner of the ramp. Figures 3.12-3.15 present the mean velocity fields obtained using PIV normalized by the freestream velocity. For each of these figures (and all further velocity field plots) the LAFPA position is indicated by the black-outlined, white rectangle in the lower left corner of each figure. The lower wall of the tunnel is indicated by the black region at the bottom of each figure, and the white region above that is the area where the PIV setup could not accurately capture the flowfield. This loss of accuracy near the wall is due to the focus plane being further away from the camera than the edge of the bottom wall. This causes the edge of the wall to be out of focus and blurry up to approximately 0.5 mm above the wall, making the PIV data obtained within that 0.5 mm not useable.

Figure 3.12 shows the mean streamwise velocity fields for various delay times after the start of the LAFPA breakdown, with the LAFPAs operated at 333 Hz. The delay times were varied from 20 μs (which is when the breakdown ends for the 333 Hz case; the LAFPA's on-times are given in Table 3.1 for the various operating frequencies) to 200 μs. From the figures it can be seen that the LAFPAs had no noticeable effect on the streamwise velocity of the flow. There is some variation in the thickness of the boundary layer near the LAFPAs; however, it is virtually the same for all the delay times and the no control case, and is most likely due to the oblique shock waves created by the LAFPA cavities. Operation of the LAFPAs has no apparent influence on those shock waves.

Table 3.1 LAFPA Operating Parameters

Frequency	On-Time
333 Hz	20 μs
1 kHz	20 μs
2 kHz	20 μs
5 kHz	20 μs
8 kHz	12 μs
20 kHz	5 μs

The mean transverse velocity fields corresponding to the streamwise velocity fields in Fig. 3.12 are shown in Fig. 3.13. Again the oblique Mach waves created by the LAFPA cavities can be seen, and do not appear to be influenced significantly by the actuator operation. At 20 μs delay (Fig. 3.13b) a blast wave created by the LAFPA can be seen; at this delay time it has already reached the edge of the boundary layer. This blast wave travels outward from the LAFPA and is also pushed downstream by the Mach 1.4 crossflow. At 40 μs (Fig. 3.13c) the blast wave has extended to about 2δ, and appears to have weakened as indicated by the reduction in the upward velocity induced by the blast wave. There also

appears to be the start of a second much weaker blast wave emanating from the cavity. By 60 µs (Fig. 3.13d) the initial blast wave has moved outside of the field of view, although the front edge can just

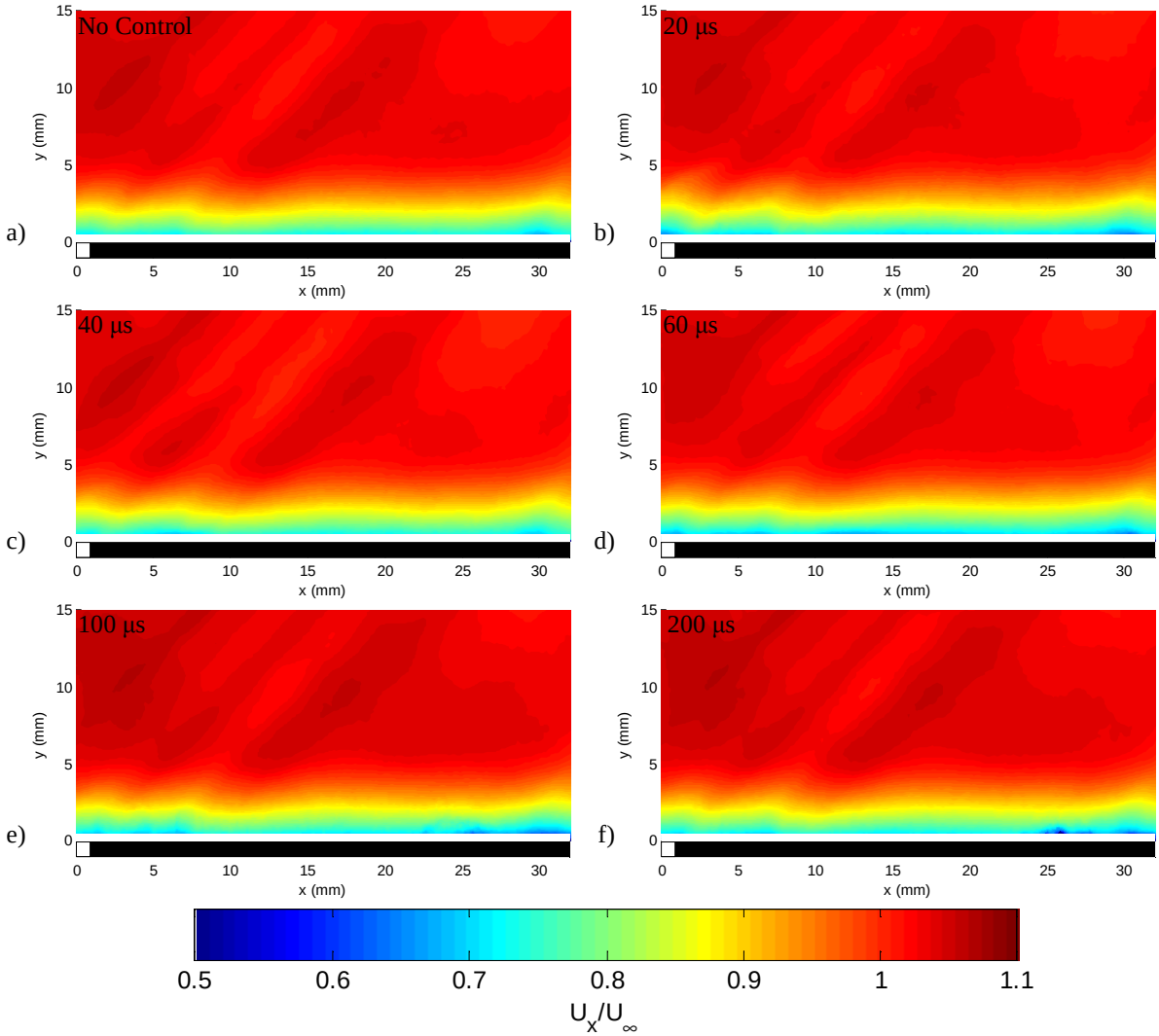

Fig. 3.12 Mean streamwise velocity normalized by the freestream velocity for the LAFPAs operated at 333 Hz at various delay times: a) no control, b) 20 µs, c) 40 µs, d) 60 µs, e) 100 µs, and f) 200 µs.

barely be seen, in addition to a few secondary, weaker blast waves. These waves are likely from reflections of the initial blast wave off the bottom of the LAFPA cavities. By 100 µs (Fig. 3.13e) all of the blast waves have completely moved out of the field of view and dissipated. At 20 µs there appears to be some upward velocity emanating from the LAFPAs, probably due to the expulsion of the heated gas from the LAFPA cavity. This plume of gas moves downstream and can be seen at 40 µs about 5 mm downstream of the LAFPAs. However, by 60 µs, the slug of hot gas has completely dissipated and cannot be seen. Additionally, the magnitude of the velocity induced by this plume is about the same or less than that induced by the Mach waves created by the edges of the boron nitride electrode housing and LAFPA

cavities, indicating that the effect is very weak. It also appears to have had no effect on the boundary layer further downstream.

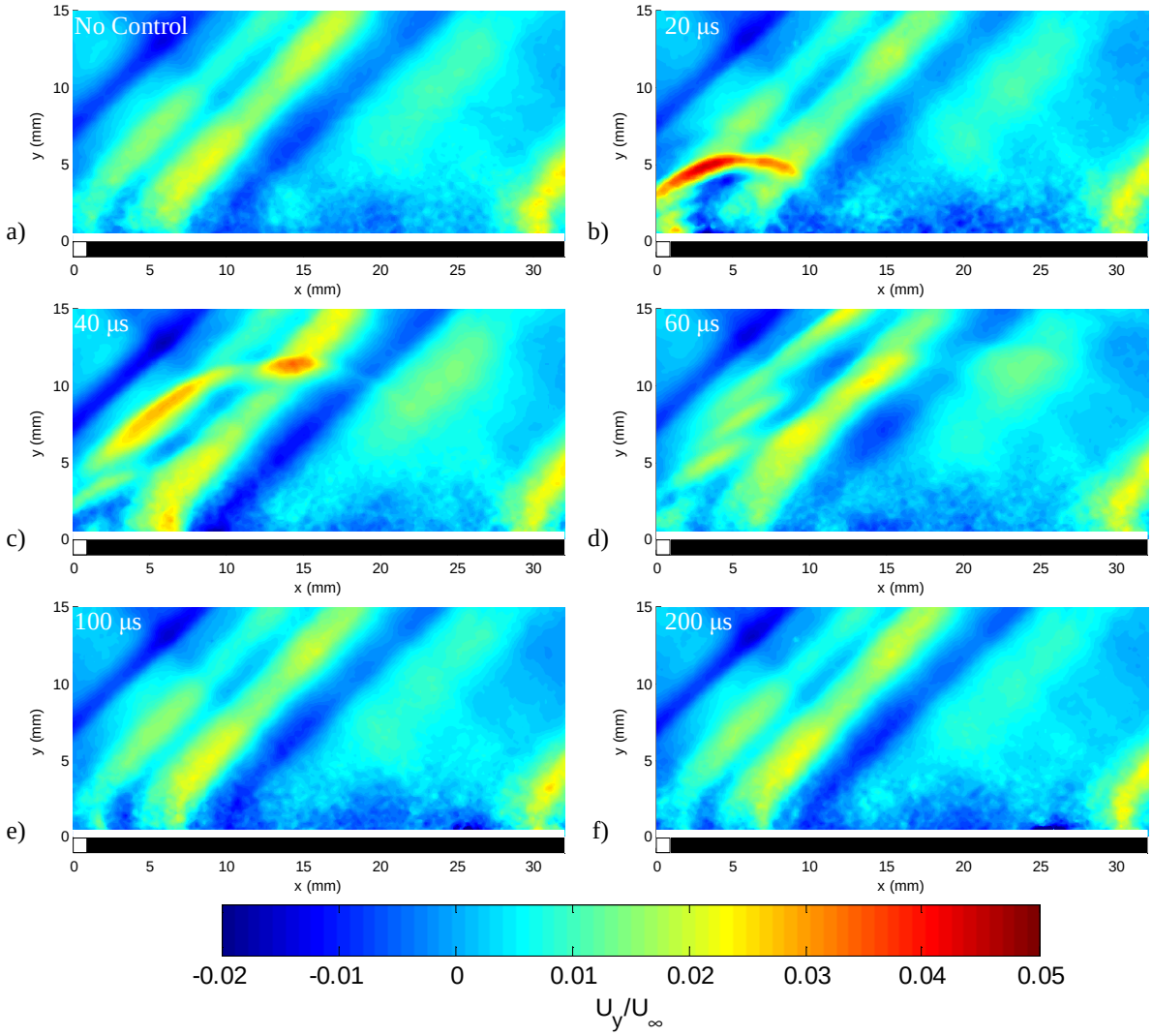

Fig. 3.13 Mean transverse velocity normalized by the freestream velocity for the LAFPAs operated at 333 Hz at various delay times: a) no control, b) 20 µs, c) 40 µs, d) 60 µs, e) 100 µs, and f) 200 µs.

Figures 3.14 and 3.15 show the normalized streamwise and transverse velocity fields for the LAFPAs operated at various frequencies, all at a delay time of 20 µs. Once again, the LAFPAs appear to have virtually no effect on the streamwise velocity, as indicated by the similarity of all the plots in Fig. 3.14. In Fig. 3.15 the blast waves all penetrate similar distances into the flow, which indicates that the speed at which the blast wave travels is not influenced by the frequency at which the LAFPAs are operated. At 20 kHz, the blast wave from the previous pulse can also be seen. The blast wave appears to weaken as the frequency is increased; the upward velocity induced by the blast wave is reduced at the higher frequencies. There are several factors that are believed to contribute to this effect. First, at the

higher frequencies there is less time between pulses for the cavity to cool and refill, resulting in less mass that can be expelled during each pulse. Second, due to the limitations of the power supply, the on-time of the LAFPAs at the higher frequencies had to be reduced (refer to Table 3.1). Additionally, the plume of gas that is expelled from the LAFPA cavity is visible for the lower frequencies, 333 Hz and 1 kHz, but not for the higher ones, 8 kHz and 20 kHz.

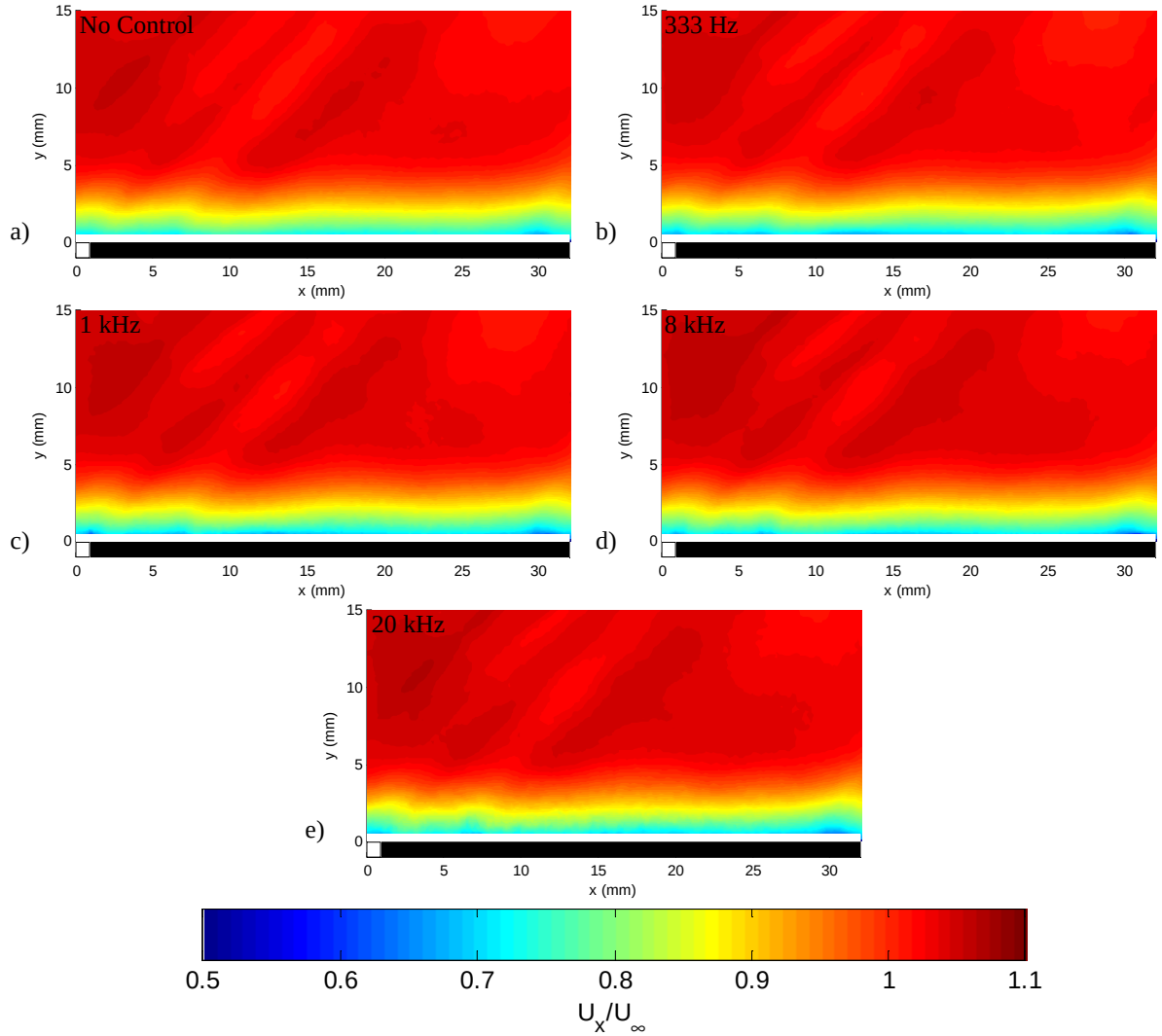

Fig. 3.14 Mean streamwise velocity normalized by the freestream velocity for the LAFPAs operated at various frequencies: a) no control, b) 333 Hz, c) 1 kHz, d) 8 kHz, and e) 20 kHz, all after a delay time of 20 μs.

It is somewhat difficult to determine from the contour plots of Figs. 3.12 and 3.14 if there is any variation in the streamwise velocity, so velocity profiles at various locations downstream of the LAFPAs have been plotted and are displayed in Fig. 3.16, for the various delay times at 333 Hz, and in Fig. 3.17 for the various frequencies at a delay time of 20 μs. These plots confirm for the most part that the LAFPAs have virtually no effect on the streamwise velocity. However, at the earliest time delay (20 μs),

it appears that within the boundary layer, the velocity profile may be slightly less full, especially for 333 Hz case. This may indicate that the LAFPAs, instead of introducing higher momentum into the boundary layer, are actually reducing the momentum.

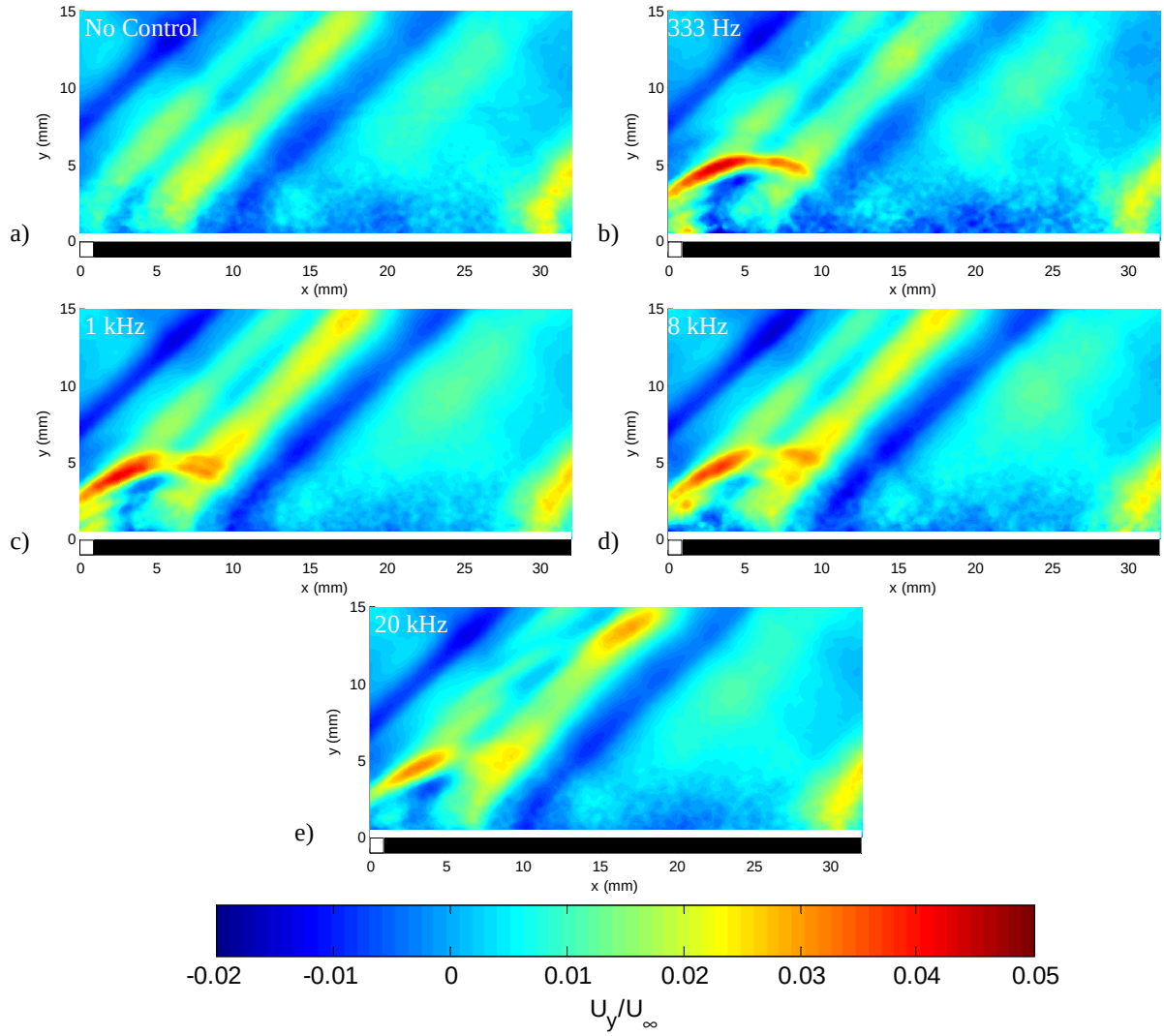

Fig. 3.15 Mean transverse velocity normalized by the freestream velocity for the LAFPAs operated at various frequencies: a) no control, b) 333 Hz, c) 1 kHz, d) 8 kHz, and e) 20 kHz, all after a delay time of 20 μs.

In order to examine this further, the mean velocity fields for the no control case were subtracted from the control (LAFPA on) cases, and the results for the various frequencies, at a delay time of 20 μs, are shown in Fig. 3.18. The differences in streamwise velocity are shown in the left column and the differences in transverse velocity are shown in the right column. The blast waves and the expelled gas are the only noticeable features in the transverse velocity difference plots. For the 333 Hz case, it appears that the LAFPAs do reduce the velocity in the boundary layer, causing the boundary layer to be less full.

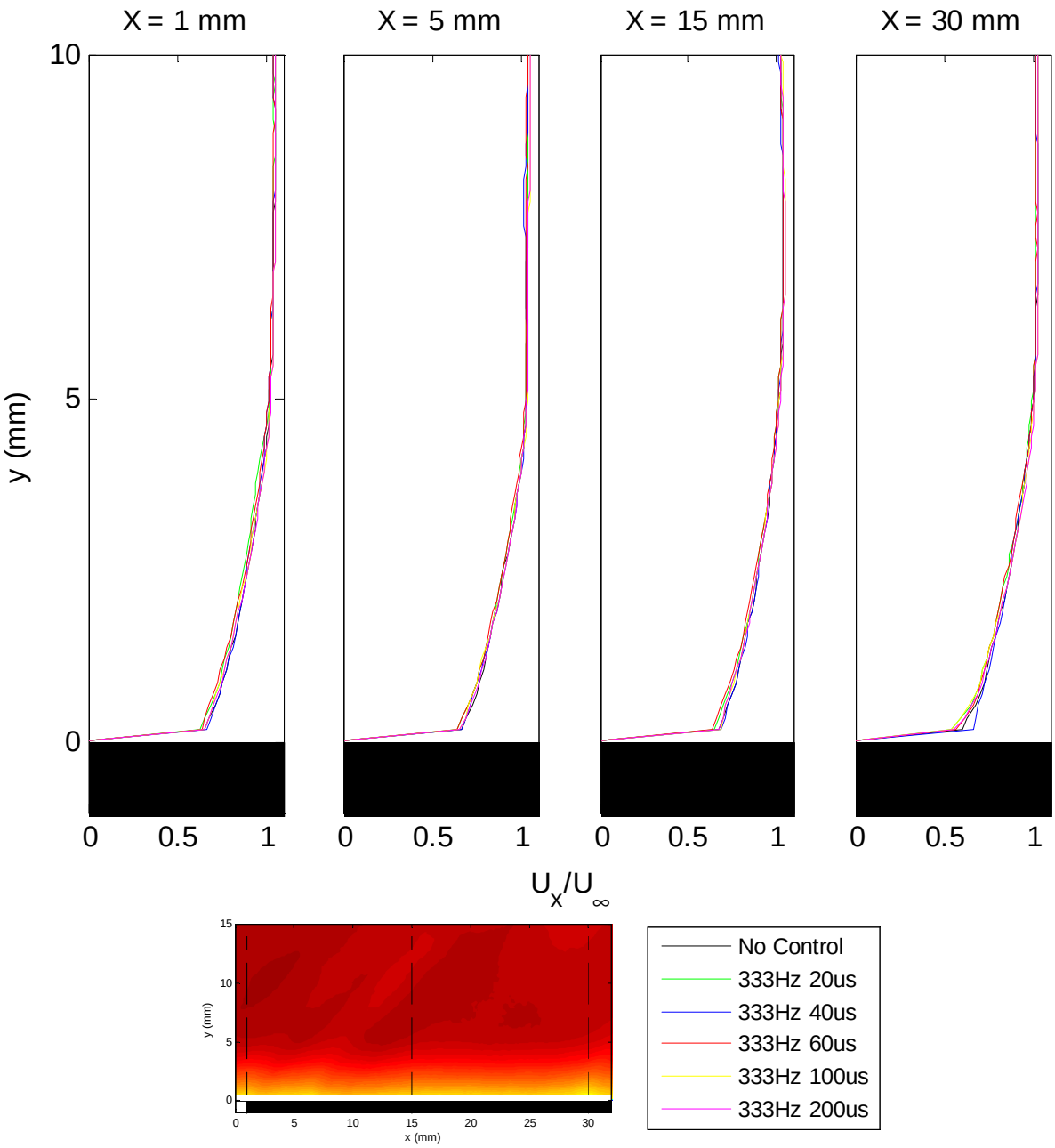

Fig. 3.16 Velocity profiles at various streamwise locations downstream of the LAFPAs, at various delay times for the LAFPAs operated at 333 Hz.

However, for the1 kHz case the LAFPA s appear to increase the velocity within the boundary, which should lead to a fuller boundary layer, and for the two higher frequency cases the LAFPAs appear to have no effect on the velocity within the boundary layer. Additionally, the differences in velocity seen in these plots are on the same order as the uncertainty in the velocity measurements, especially within the boundary layer. Because of this and the inconsistency of the effect on streamwise velocity, it is believed

that those differences are just naturally occurring differences that would be expected regardless of the LAFPAs' operation.

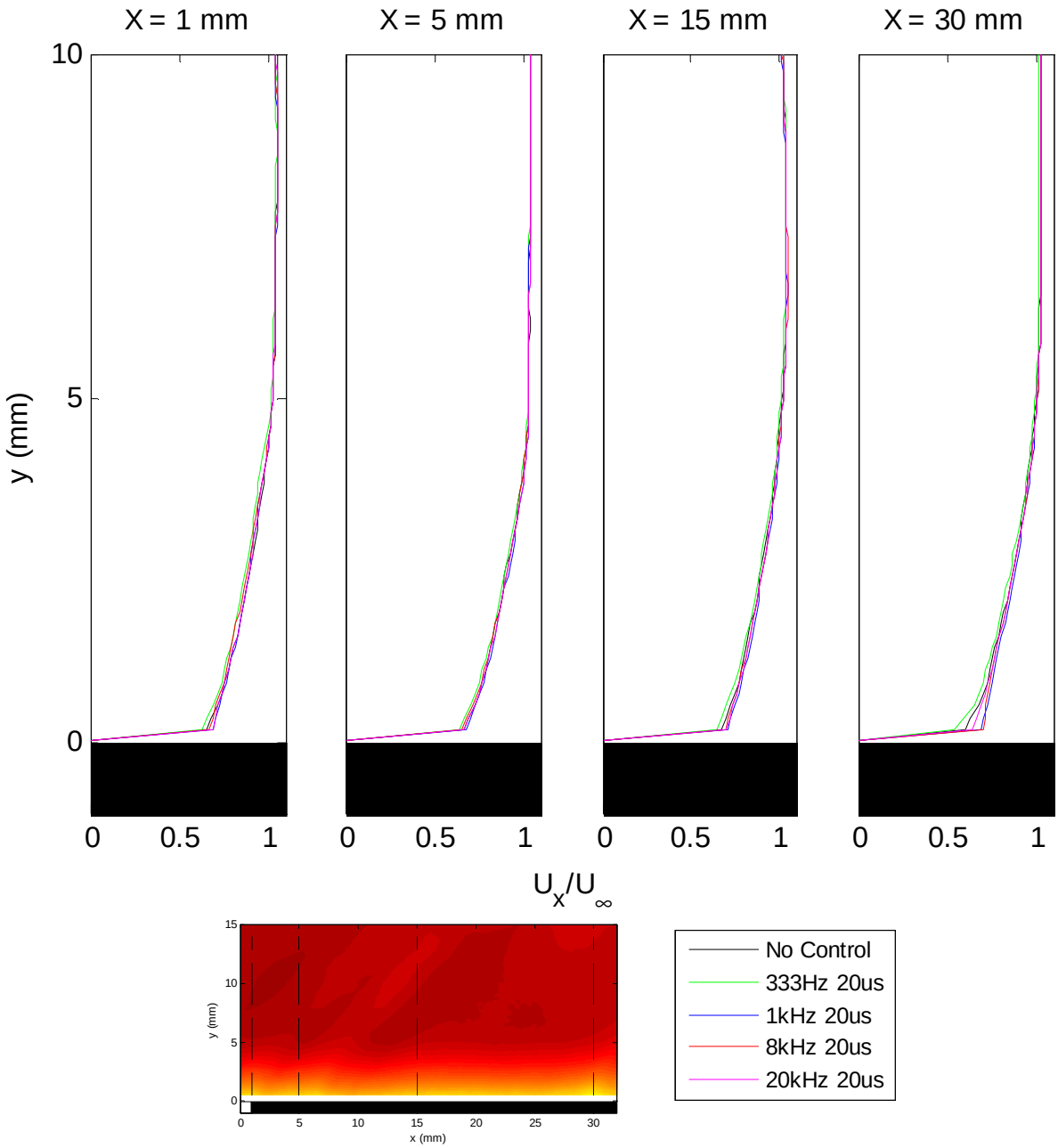

Fig. 3.17 Streamwise velocity profiles at various streamwise positions downstream of the LAFPAs, operated at various frequencies, at a delay time of 20 µs.

3.3.3 Supersonic Boundary Layer After a 5° Diffuser

PIV was again used in order to determine the effect that the LAFPAs have on the separation region after the corner of a 5º diverging ramp. Due to glare from the LAFPAs' boron nitride insert, the field of view was initially set about 10 mm downstream of the corner and LAFPAs. Additionally, the

stagnation- to-exit pressure ratio was maintained at approximately 1.35, so that the normal shock's mean position was at the corner. Once again, in the velocity field plots, the bottom wall is

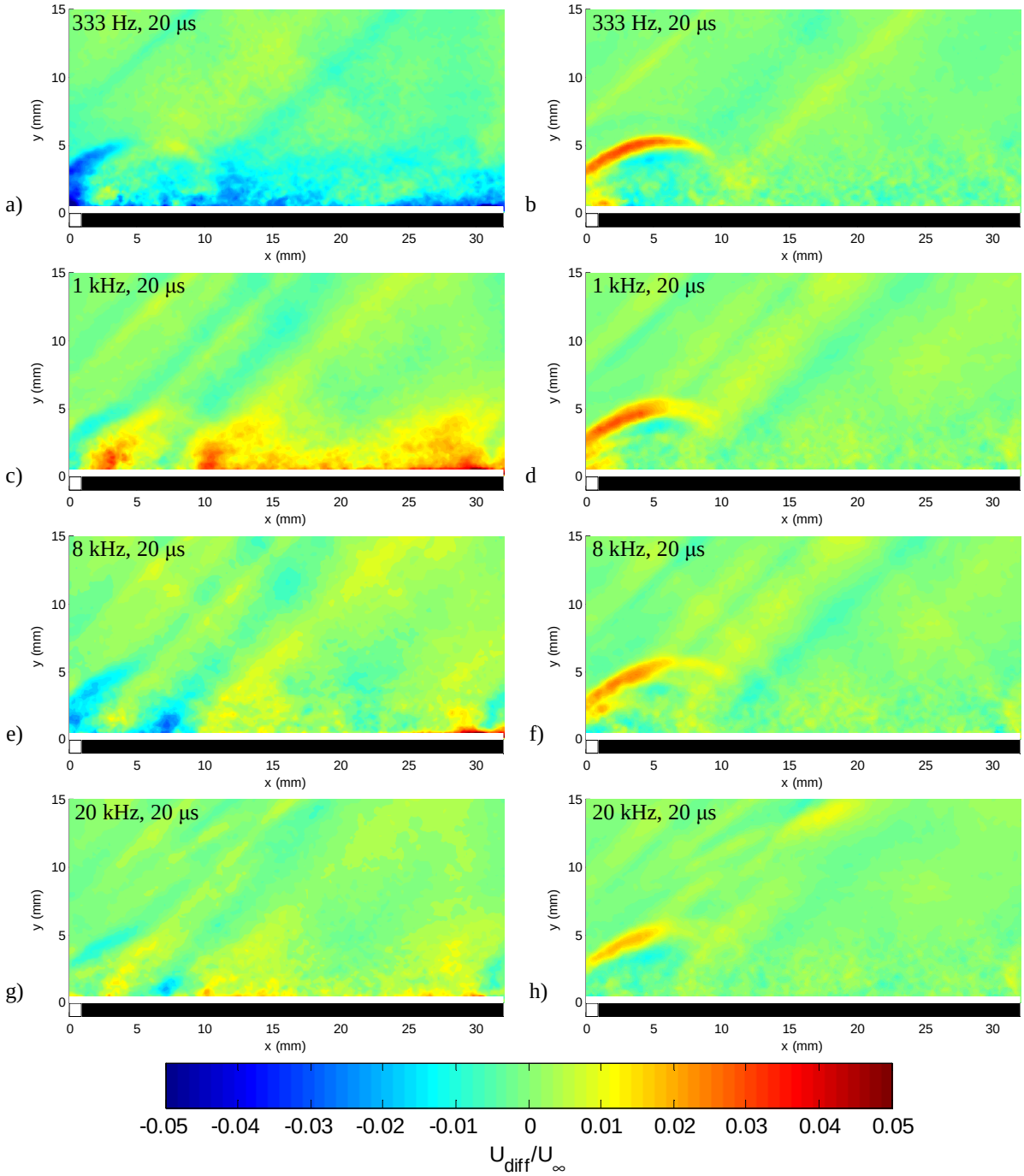

Fig. 3.18 Velocity difference between control cases and no control case, normalized by freestream velocity, at a delay time of 20 µs, for LAFPAs operated at various frequencies a-b) 333 Hz, c-d) 1 kHz, e-f) 8 kHz, and g-h) 20 kHz. The left column is the difference in mean streamwise velocity and the right column is the difference in mean transverse velocity (from the no-control case).

represented by the black area and the white area above it is the region where the boundary layer could not be accurately captured by the PIV set-up.

Figure 3.19 shows the mean streamwise velocity for some sample cases, varying both frequency of LAFPA operation and delay time after the breakdown. As can be seen in the figure, the LAFPAs have minimal effect on the streamwise velocity in the boundary layer and the separation region, regardless of frequency or delay time. Similarly, as seen in Fig. 3.20, the LAFPAs have minimal effect on the transverse velocity. The only noticeable effect of the LAFPAs that can be seen in these figures is the

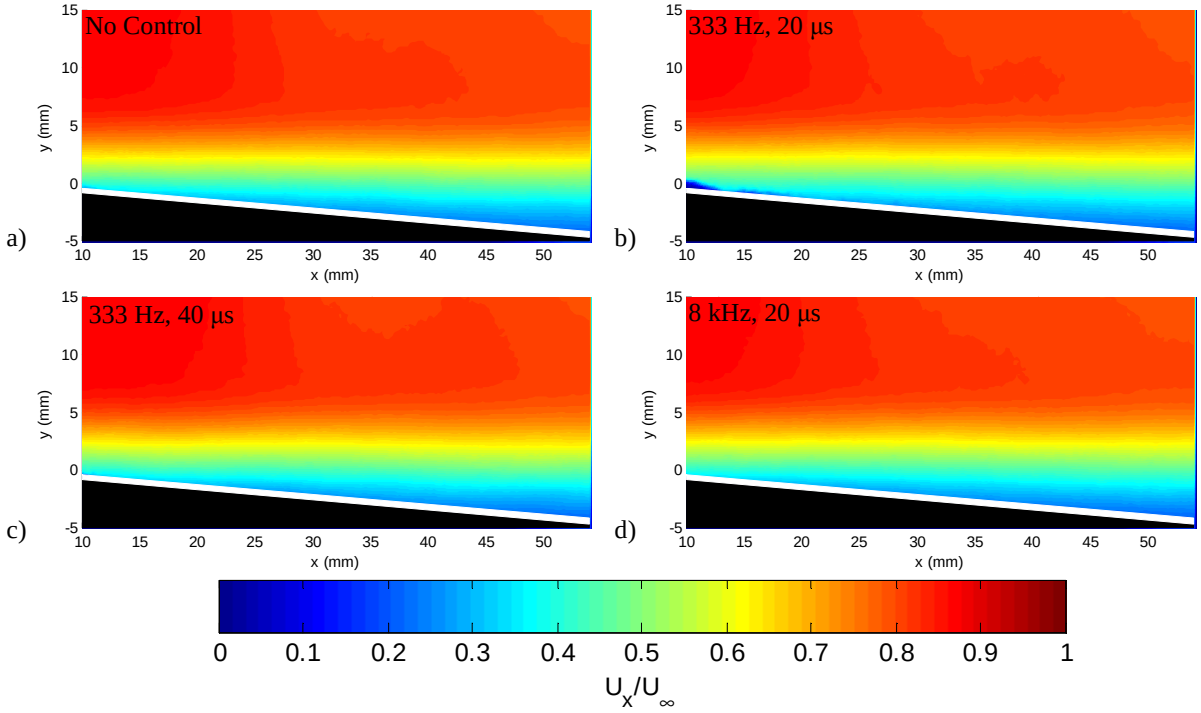

Fig. 3.19 Mean streamwise velocity normalized by the freestream velocity for some sample cases: a) No Control, b) 333 Hz at a delay of 20 µs, c) 333 Hz at a delay of 40 µs, and d) 8 kHz at a delay of 20 µs.

downstream edge of the blast wave at 40 µs for the 333 Hz case (Fig. 3.20c), which appears to be relatively weak. From these figures it appears that the LAFPAs do not have any significant influence on the flow far downstream of the actuators. This is confirmed by the velocity profiles presented in Fig. 3.21, as there is virtually no difference between no control and the various control cases at the two furthest downstream locations. There is some difference at the location 15 mm downstream of the LAFPAs; however, this variation is in the 0.5 mm region closest to the wall, and as discussed earlier, is believed to be not actually representative of the flow in that region.

In order to observe any of the LAFPAs' effects on the flow, the field of view needed to include the region immediately downstream of the LAFPAs and the LAFPAs themselves. Thus, the field of view was moved upstream, and to overcome the glare created by the boron nitride insert, it was painted black,

with care taken to not paint the electrodes or inside the cavities. Figure 3.22 shows the mean streamwise velocity for the LAFPAs operated at 5 kHz, for various delay times, with the position of the actuators indicated by the outlined white square. Once again, the LAFPAs have essentially no effect on the streamwise velocity; however, for the 60 μs delay time (Fig. 3.22d), there is some difference in the freestream velocity at the upstream edge of the figure. This is due to the mean shock position being slightly further downstream for this case. As seen in section 3.3.1, the LAFPAs have very little influence over the position of the normal shock, so this variation in shock position is most likely due to natural variation of the mean shock position and to the difficulty of controlling the tunnel stagnation pressure precisely.

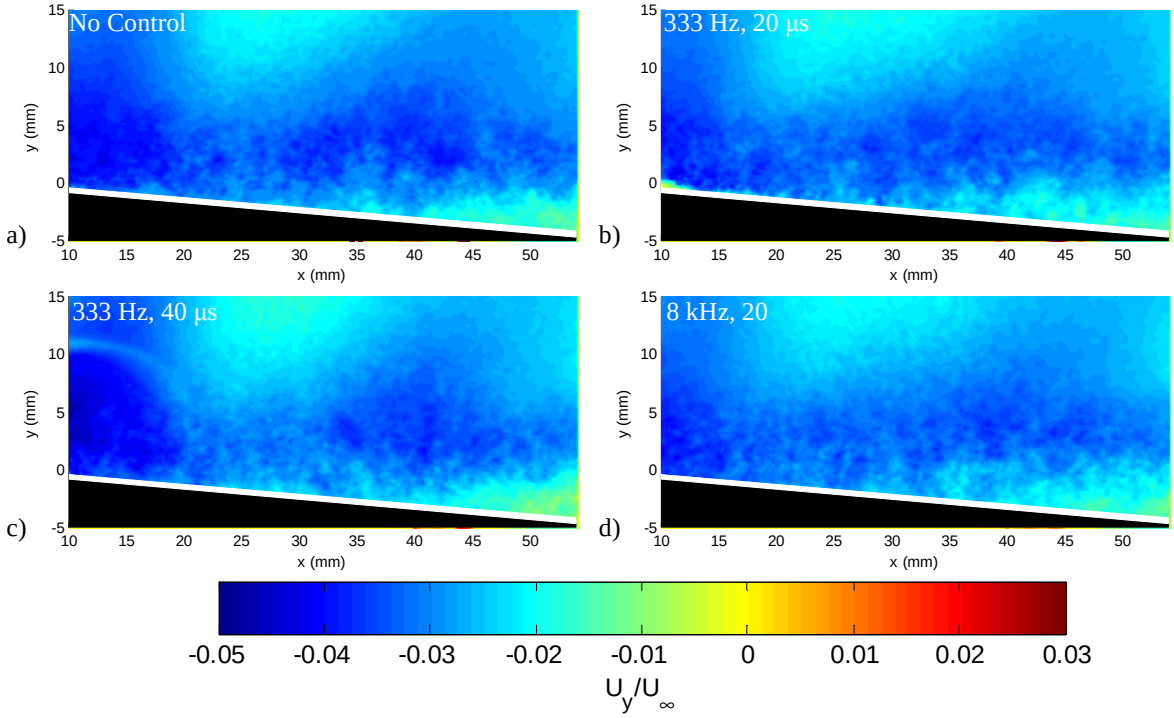

Fig. 3.20 Mean transverse velocity normalized by the freestream velocity for some sample cases: a) No Control, b) 333 Hz at 20 μs, c) 333 Hz at 40 μs, and d) 8 kHz at 20 μs.

The mean transverse velocity plots corresponding to Fig. 3.22 are shown in Fig. 3.23. Similar to the boundary layer case, the most noticeable effect of the LAFPAs is the blast wave that is seen at 20 and 40 μs (Figs. 3.23b-c), but has mostly dissipated by 60 μs (Fig. 3.23d). Previously, the blast wave was visible at 60 μs as well, but in this case the blast wave was weaker due to the increased frequency. It is also believed that the transverse velocity induced by the normal shock overwhelmed that of the blast wave because the mean position of the normal shock was slightly downstream for this case compared to the others. Less noticeable is the weak plume of heated gas visible at the 20 μs delay time, just below the blast wave. There appears to be no evidence of this plume at 40 and 60 μs, and the 100 and 200 μs (Figs.

3.23e-f) time delays appear basically identical to the no control case, indicating that, once again, this plume dissipates quickly and is not propagated downstream.

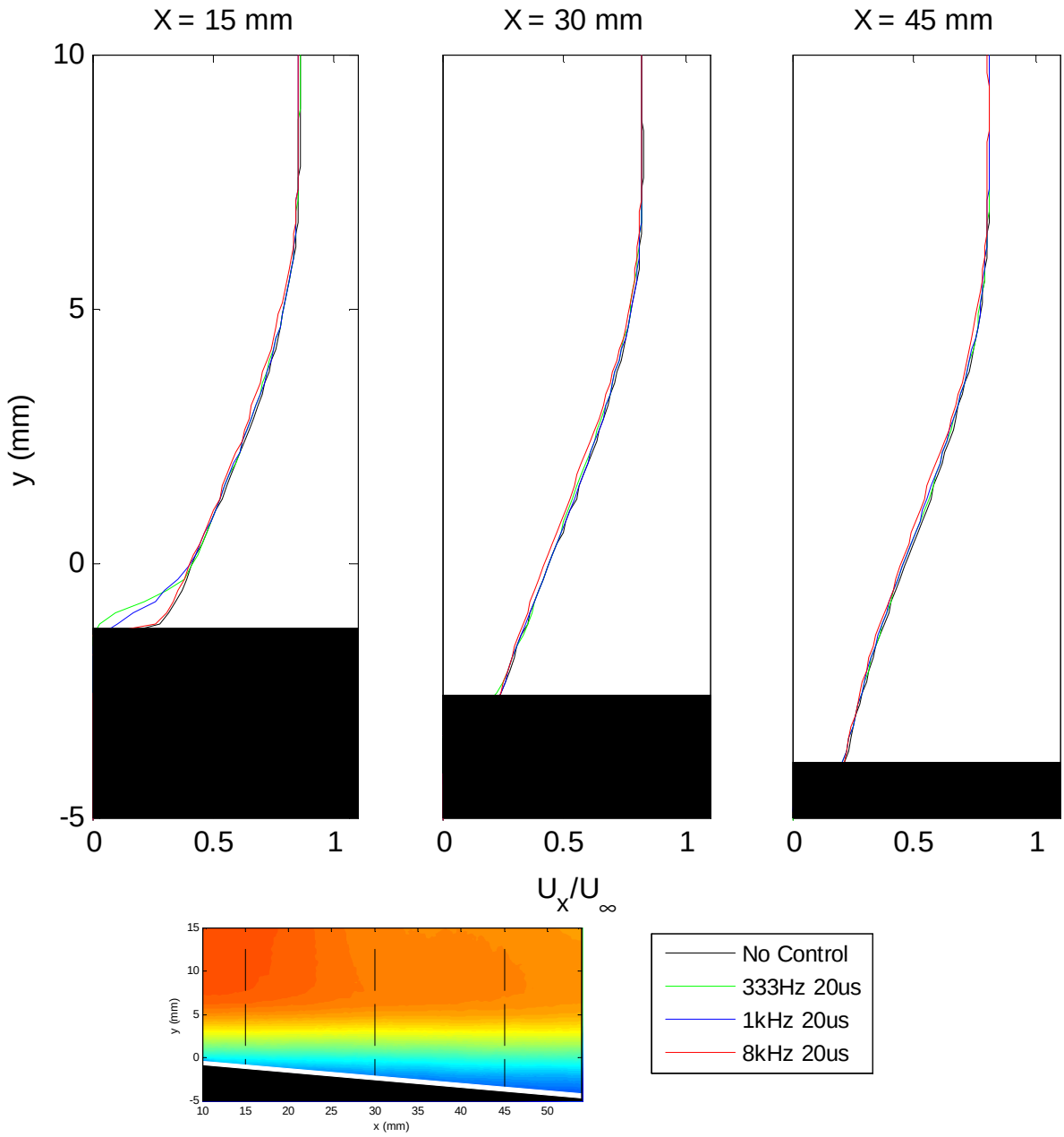

Fig. 3.21 Streamwise velocity profiles at various streamwise positions downstream of the LAFPAs, operated at various frequencies, at a delay time of 20 µs.

An additional frequency of 2 kHz was investigated and the mean position of the shock was shifted to approximately 10 mm upstream of the LAFPAs (this was accomplished with a stagnation-to-exit pressure ratio of 1.32), in order to study the influence of the shock location on the LAFPAs' effects and on the boundary layer. The mean streamwise velocity for those cases is shown in Fig. 3.24. It appears

that the LAFPAs have very little effect on the streamwise velocity. The shock location, however, does appear to have a significant influence; the boundary layer is much thicker approaching the corner and the freestream velocity is reduced, as expected, due to passing through the normal shock and the following shock train.

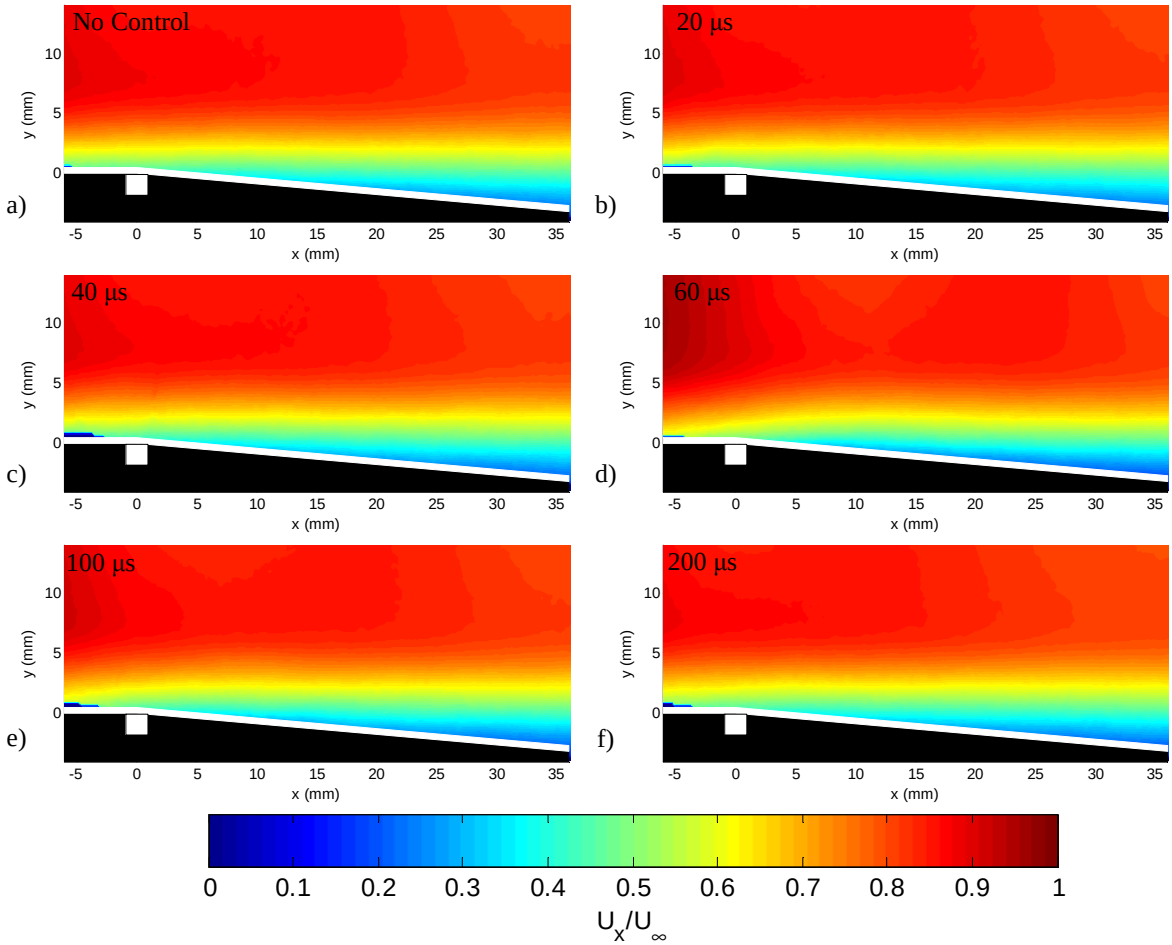

Fig. 3.22 Mean streamwise velocity normalized by the freestream velocity for the LAFPAs operated at 5 kHz at various delay times: a) no control, b) 20 µs, c) 40 µs, d) 60 µs, e) 100 µs, and f) 200 µs.

The mean transverse velocity fields for the same cases are shown in Fig. 3.25. Reducing the frequency from 5 kHz to 2 kHz noticeably increases the strength of the blast wave at both 20 and 40 µs (Figs. 3.25c and 3.25e), and the plume of heated gas produced by the arc is evident through 40 µs. However, moving the shock upstream (Figs. 3.25b, 3.25d, and 3.25f) has a much more drastic effect: it severely weakens the blast wave that is produced by the LAFPAs. There is still a slight disturbance created by the hot gas being ejected from the LAFPA cavity which can be observed at 20 µs. For both cases, however, the heated gas is dissipated quickly and the velocity disturbance is not propagated downstream.

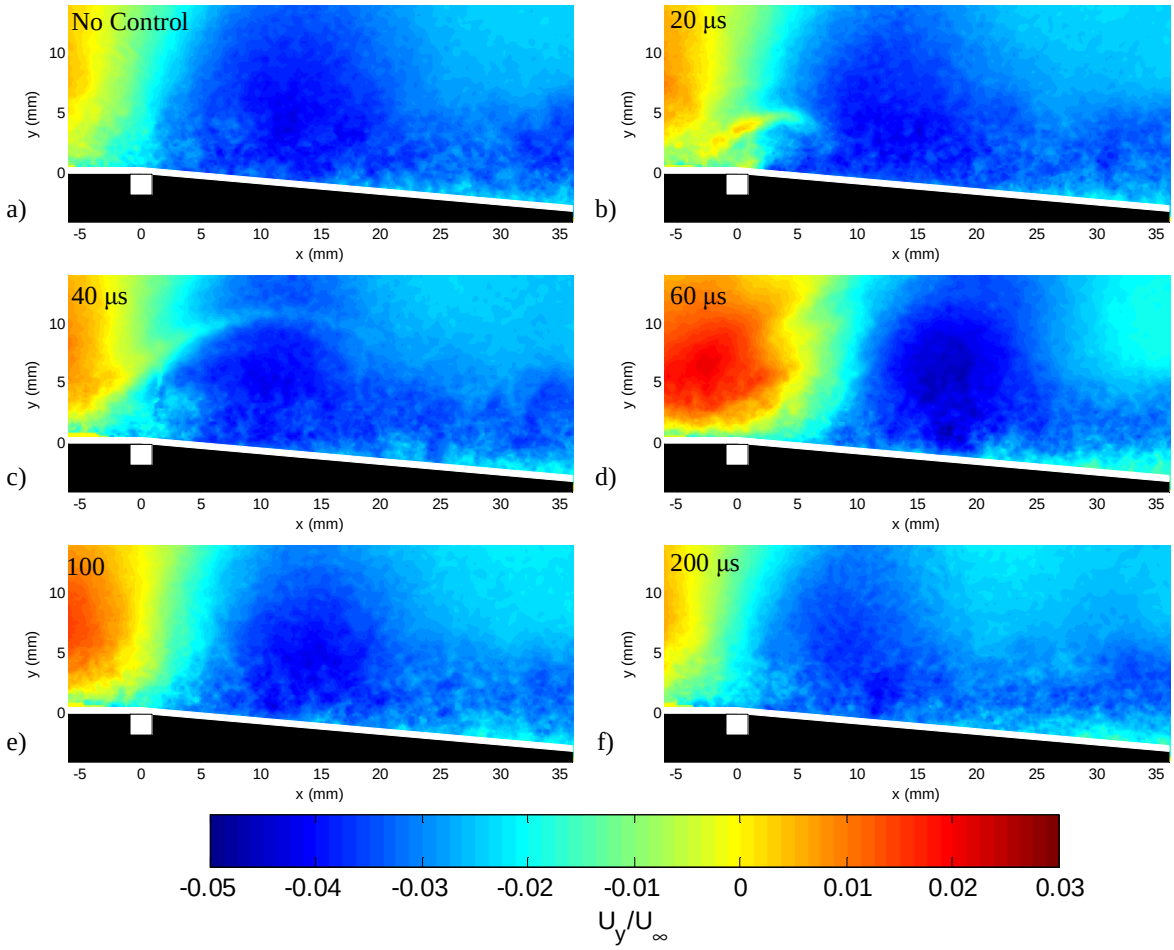

Fig. 3.23 Mean transverse velocity normalized by the freestream velocity for the LAFPAs operated at 5 kHz at various delay times: a) no control, b) 20 µs, c) 40 µs, d) 60 µs, e) 100 µs, and f) 200 µs.

Streamwise velocity profiles for the 2 kHz, 5 kHz, and upstream shock location, at delay times of 20 µs, are shown in Fig. 3.26. It can be seen from the figure that the upstream shock location significantly changes the boundary layer profile; it is significantly less full than the cases where the mean shock location is at the corner. Additionally, the boundary layer is tending towards separation much earlier when the shock is further upstream as indicated by the inflection point that is visible in the boundary layer profile for each streamwise location. That inflection point is only visible in the cases with the shock on the corner at the furthest downstream velocity profile (X = 30 mm). Yet again, the LAFPAs have very little effect on the flow, regardless of shock position. There is practically no difference in the velocity profile of the no control and control cases for the shock on the corner; for the shock in the upstream position it appears that the velocity profile is slightly less full for the control case as compared to the no control case.

In order to quantify the differences in velocity, the mean velocity field for the no control case was subtracted from that of the control cases, and the results are shown in Fig. 3.27. There seems to be more variation for the case with the LAFPAs operated at 2 kHz (Figs. 3.27a-b), however, this is due to slight variation in the shock position at the corner. For the LAFPA frequency of 5 kHz (Figs. 3.27c-d), there is virtually no difference in the streamwise velocity field. For the case of the upstream shock location (Figs. 3.27e-f), there is some variation in streamwise velocity, but this could again be due to slight variation in the mean shock position upstream of the corner. However, even if there is no variation in shock position, the difference in velocity between the no control and control cases is still very small and on the order of the uncertainty in the velocity measuremetns, which indicates that the LAFPAs have little to no influence over the flow.

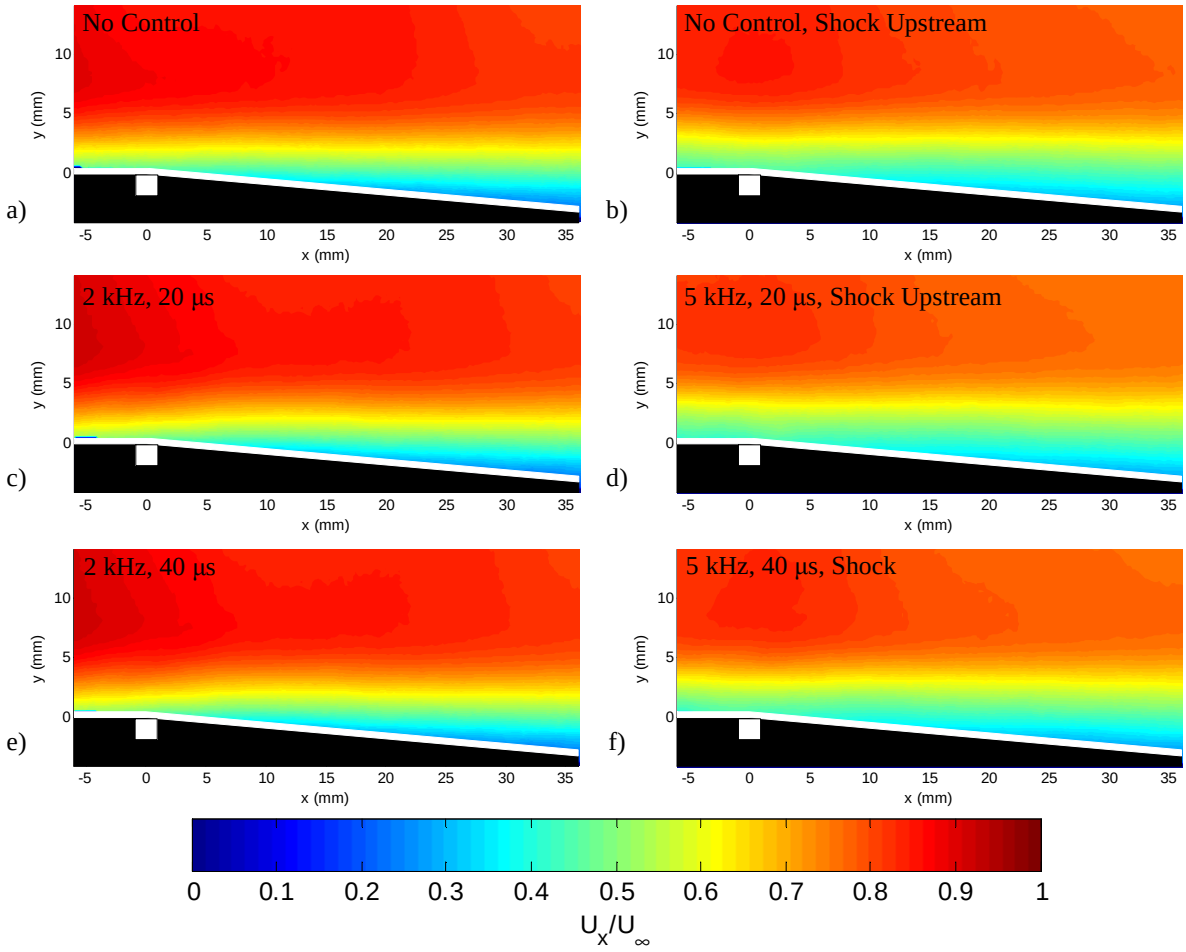

Fig. 3.24 Mean streamwise velocity normalized by the freestream velocity for a) no control, b) no control with the shock upstream of the corner, c) LAFPA frequency of 2 kHz and delay time of 20 µs, d) LAFPA frequency of 5 kHz, delay time of 20 µs, and shock upstream of corner, e) LAFPA frequency of 2 kHz and delay time of 40 µs, and f) LAFPA frequency of 5 kHz, delay time of 40 µs, and shock upstream of the corner.

Overall, the LAFPAs produce very weak effects, but it was believed that increasing the current through the arc, and thus increasing the instantaneous power, might produce more significant effects. In order to do this, the four high-power resistors on each side of the high-voltage switches were placed in parallel with each other and used to operate a single actuator. A schematic of this circuit is shown in Fig. 3.28. This configuration would nominally maintain 4 A through the arc breakdown. Unfortunately, due to extreme EMI with the oscilloscope, voltage and current traces could not be obtained, but it is believed that the HV power supply limited the current to a value slightly below 4 A.

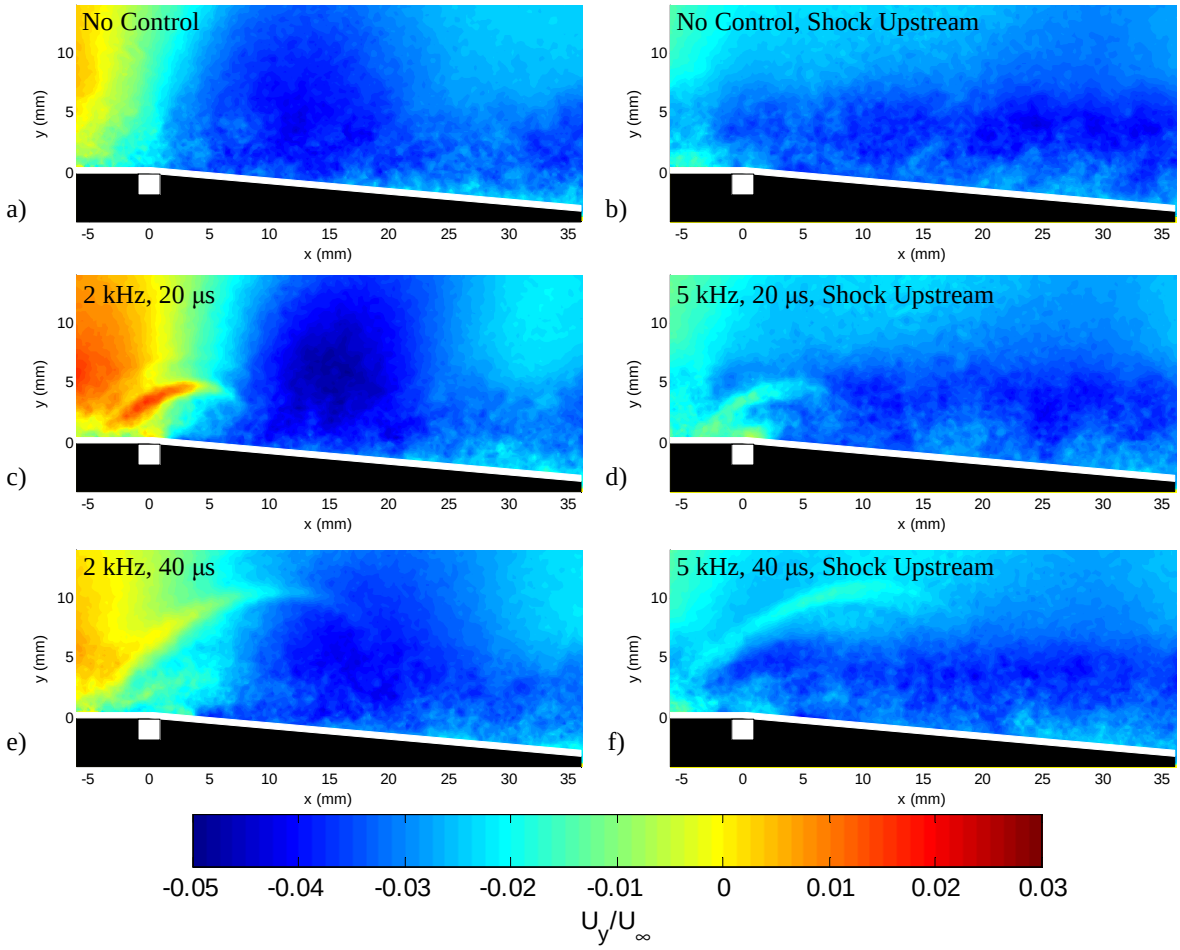

Fig. 3.25 Mean streamwise velocity normalized by the freestream velocity for a) no control, b) no control with the shock upstream of the corner, c) LAFPA frequency of 2 kHz and delay time of 20 µs, d) LAFPA frequency of 5 kHz, delay time of 20 µs, and shock upstream of corner, e) LAFPA frequency of 2 kHz and delay time of 40 µs, and f) LAFPA frequency of 5 kHz, delay time of 40 µs, and shock upstream of the corner.

The mean streamwise velocity for various frequencies and delay times is shown in Fig. 3.29. There is, yet again, no appreciable difference in the streamwise velocities, regardless of LAFPA operation. However, the transverse velocity plots, Fig. 3.30, show some more interesting results. Similar to the previous results for 1 A through the arc, the blast wave and plume of hot gas are present at 20 µs

delay (Figs. 3.30b, 3.30d, and 3.30f), except for 20 kHz (Fig. 3.30f), which only produces a blast wave. However, they appear to be stronger (induce higher transverse velocities, especially in the plume) for the 4 amp case than for the 1 amp cases. Additionally, the blast wave appears stronger at 40 µs (Figs. 3.30c, 3.30e, and 3.30g), and the plume of gas appears to have persisted through this delay time, especially for the lowest frequency of 333 Hz (Fig. 3.30c).

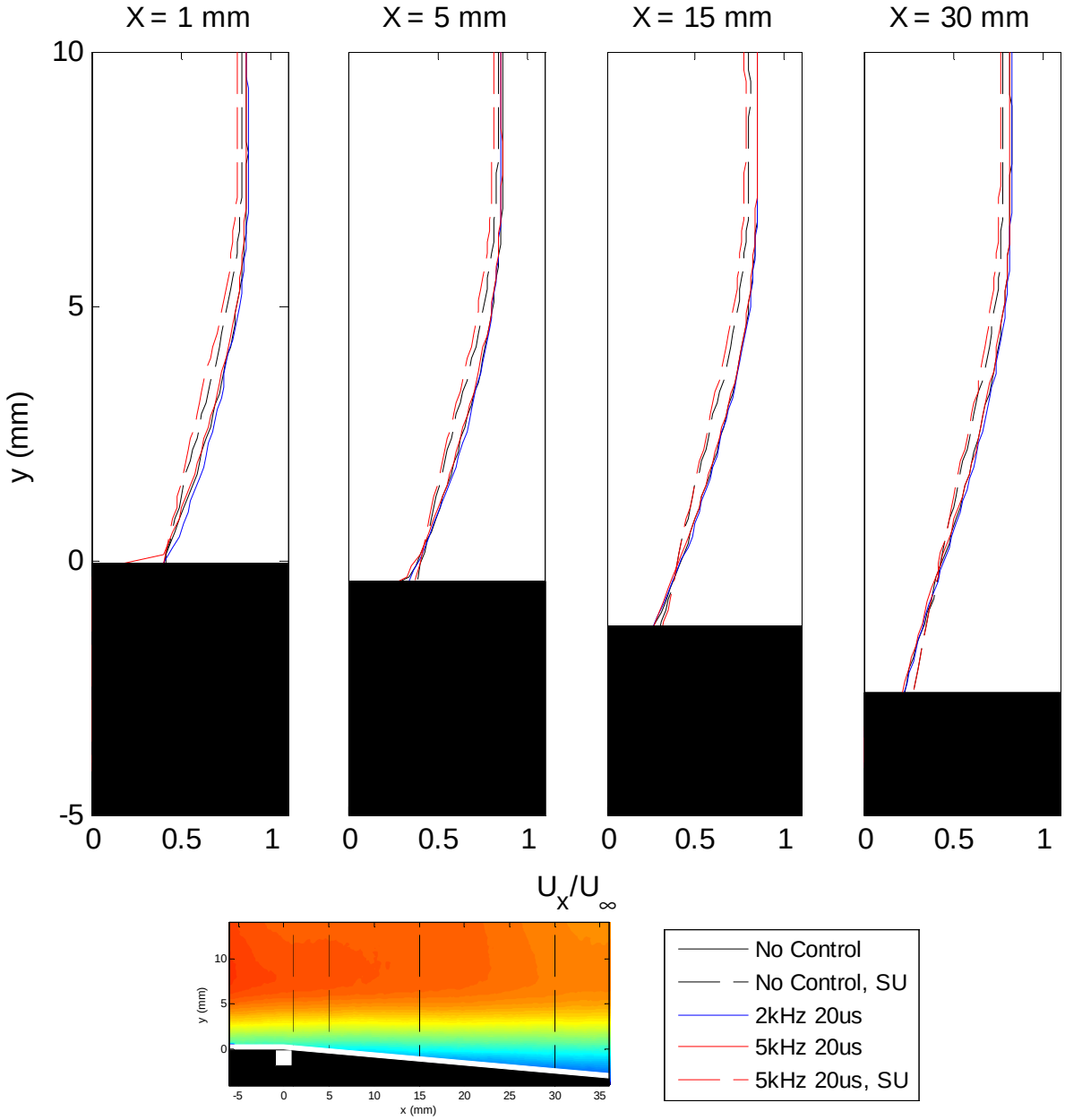

Fig. 3.26 Streamwise velocity profiles at various streamwise positions downstream of the LAFPAs, operated at various frequencies, at a delay time of 20 µs, and for two different shock locations. (SU indicates the shock upstream position.)

Streamwise velocity profiles for the various frequencies, all at a delay time of 20 µs, are plotted in Fig. 3.31, for various streamwise locations downstream of the actuators. At the location closest to the LAFPAs, the boundary layer for the control cases appears to be significantly less full than the boundary layer for the no control case. For the downstream locations there is virtually no difference between the control cases and the no control case. The same velocity profiles, but at a delay time of 40 µs, are shown in Fig. 3.32. At this time delay, there appears to still be a slight difference in the velocity profiles at the

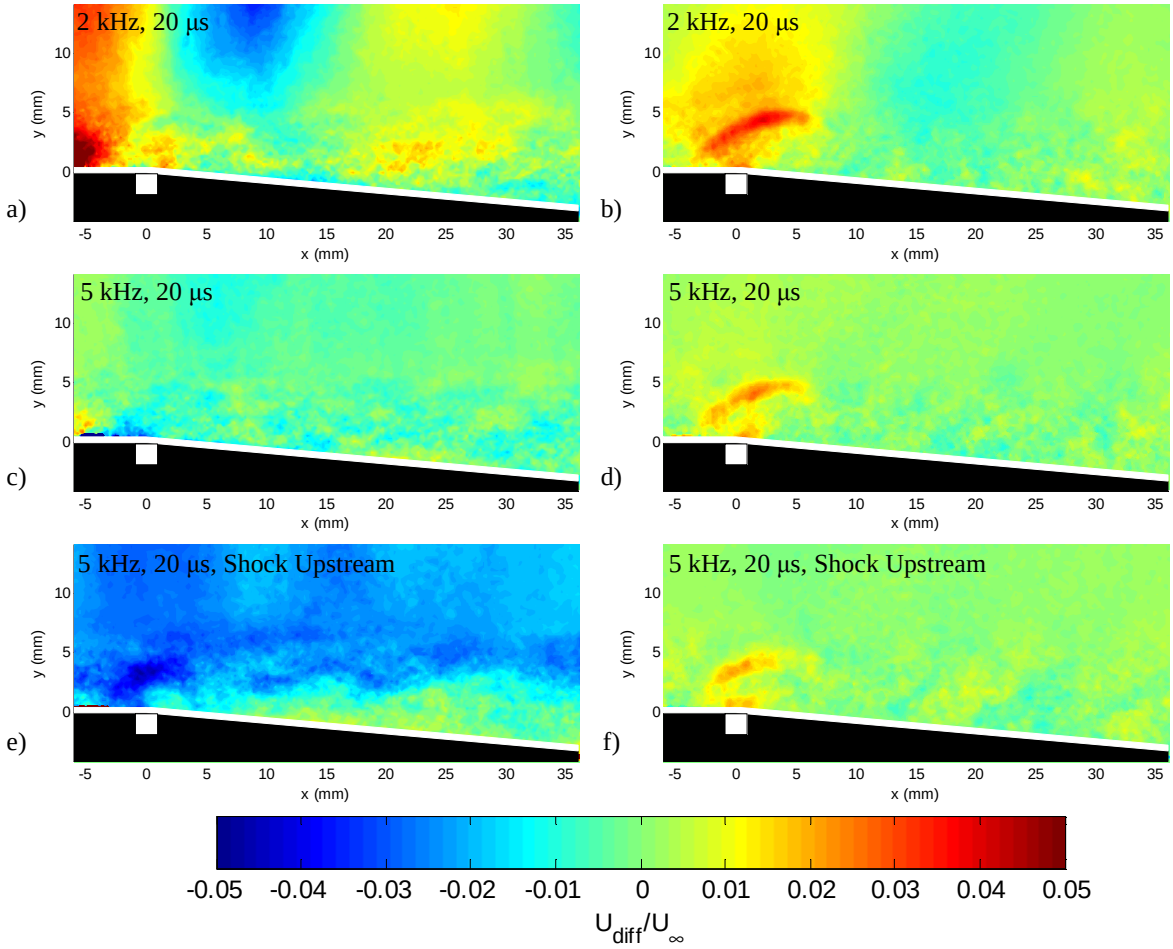

Fig. 3.27 Velocity difference between control cases and no control case, normalized by freestream velocity, at a delay time of 20 µs, for LAFPAs operated at various frequencies a-b) 2 kHz, c-d) 5 kHz, and e-f) 5 kHz, with the shock upstream of the corner. The left column is the difference in mean streamwise velocity and the right column is the difference in mean transverse velocity (from the no control case).

location closest to the LAFPAs, however, it is less significant than at 20 µs, and it does not appear to have propagated downstream. Plots of the difference in velocity between the control cases and no control case, displayed in Fig. 3.33, show that the LAFPA with 4 A of current do produce some differences in velocity, some of them larger than the 1 A case. However, once again, these differences in velocity are slight and

on the order of the uncertainty in the velocity measurements. Additionally, as can be seen in the 20 kHz case (Figs. 3.33e-f), the mean location of the normal shock still has the largest influence on the velocities.

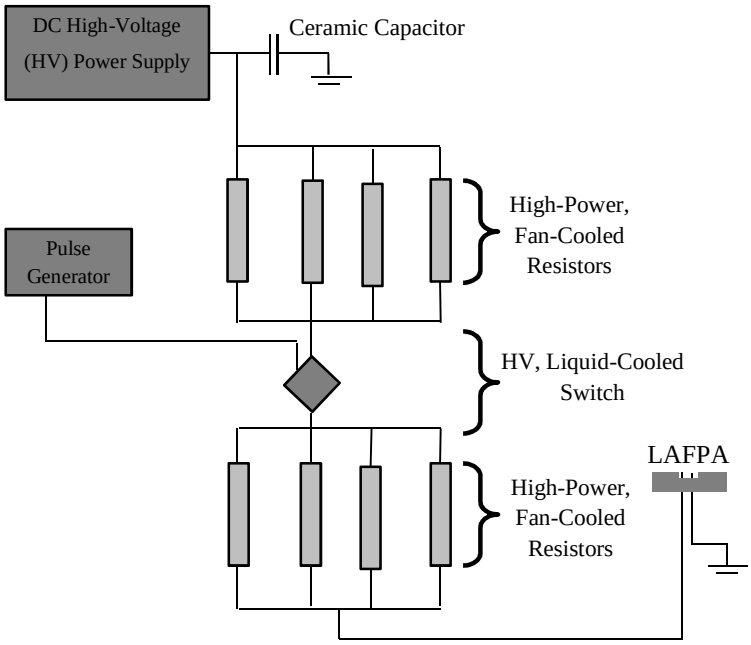

Fig. 3.28 Schematic of the 4 A LAFPA circuit.

3.4 Conclusions

An array of four localized arc filament plasma actuators was placed in a Mach 1.4 crossflow, both far upstream of the corner of a 5º diffuser and centered on that corner. Schlieren imaging was used to investigate the influence of the LAFPAs on the stability of the normal shock that occurs in the tunnel during start up. Particle image velocimetry was used to investigate the effect of the actuators on the boundary layer over a flat wall and after the 5º diffuser corner.

The schlieren images gave a preliminary view of the flowfield inside the wind tunnel as well as the LAFPA behavior. The LAFPA cavities and the edges of the actuator housing produce weak oblique shock waves even with the actuators off. When the LAFPAs were operated at various frequencies, they produced a blast wave that was observed moving downstream and being dissipated by the supersonic crossflow. However, they had virtually no influence over the mean position of the shock, regardless of frequency, delay time, actuator position, and nominal shock position. They similarly had practically no effect on the standard deviation of the shock position.

PIV also showed the blast wave produced by the actuators, and indicated that that wave was reduced in strength as the actuator frequency was increased. The travelling speed of the blast wave was

found to be unaffected by the frequency of the actuators. Additionally, the plume of hot gas created by the arc breakdown was observed to induce some upward velocity and this effect also got weaker as the actuator frequency was increased. This plume of gas caused the boundary layer profile to become slightly

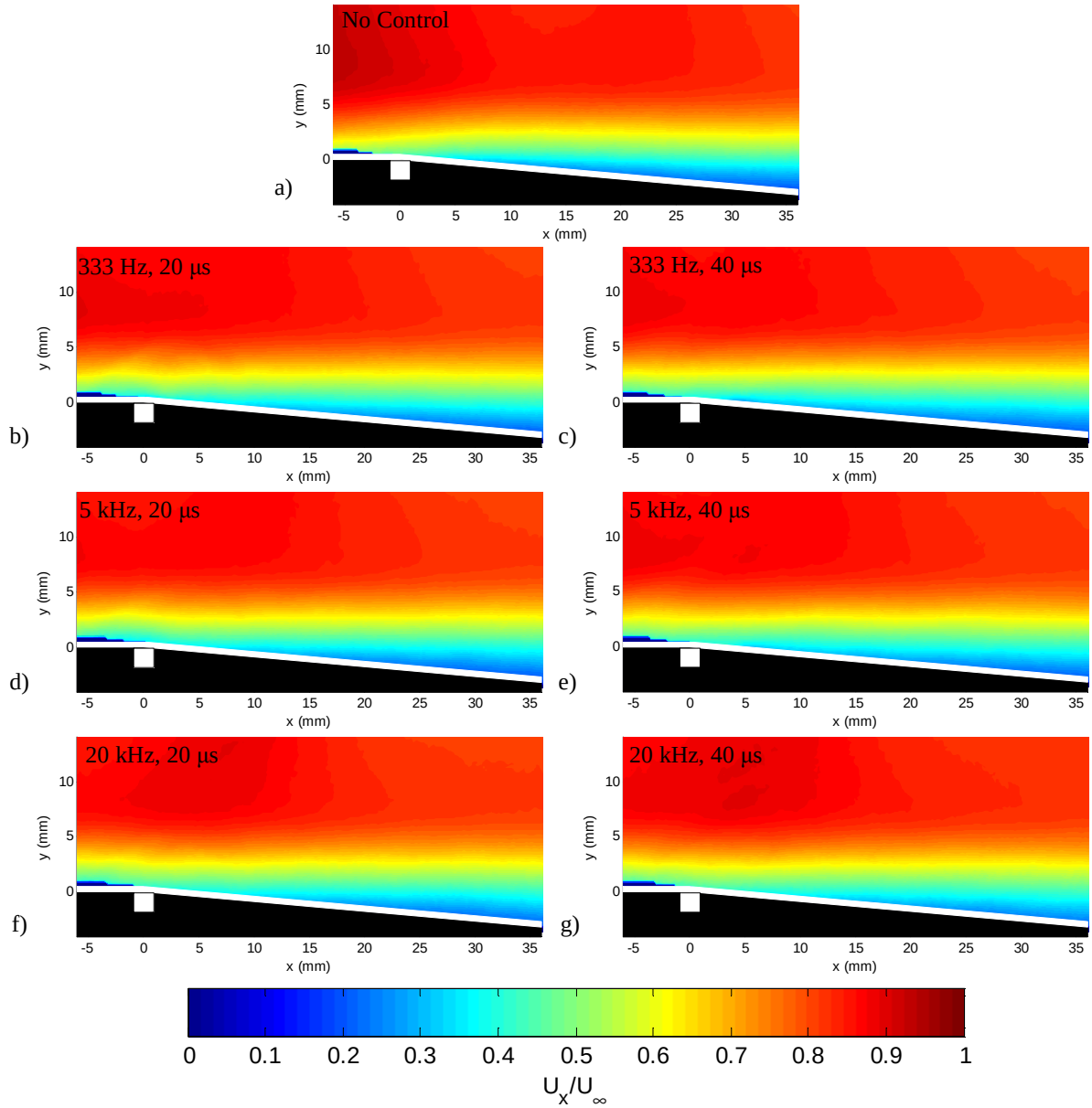

Fig. 3.29 Mean streamwise velocity normalized by the freestream velocity for a) no control, b) LAFPA frequency of 333 Hz and delay time of 20 µs, c) LAFPA frequency of 333 Hz and delay time of 40 µs, d) LAFPA frequency of 5 kHz and delay time of 20 µs, e) LAFPA frequency of 5 kHz and delay time of 40 µs, f) LAFPA frequency of 20 kHz and delay time of 20 µs, and g) LAFPA frequency of 20 kHz and delay time of 40 µs.

less full, but only in very close proximity to the LAFPAs. All of the disturbances introduced to the flow by the LAFPAs were dissipated relatively quickly and did not propagate downstream. Increasing the current through the arc breakdown increased the strength of the blast wave and plume, however, not

enough for them to be propagated further in space or time. Overall the LAFPAs produced minimal effects on the flow, and none of them were of significant benefit to the normal shock position and stability or the boundary layer. It is unlikely that these actuators have any control authority over these particular flowfields and plasma conditions.

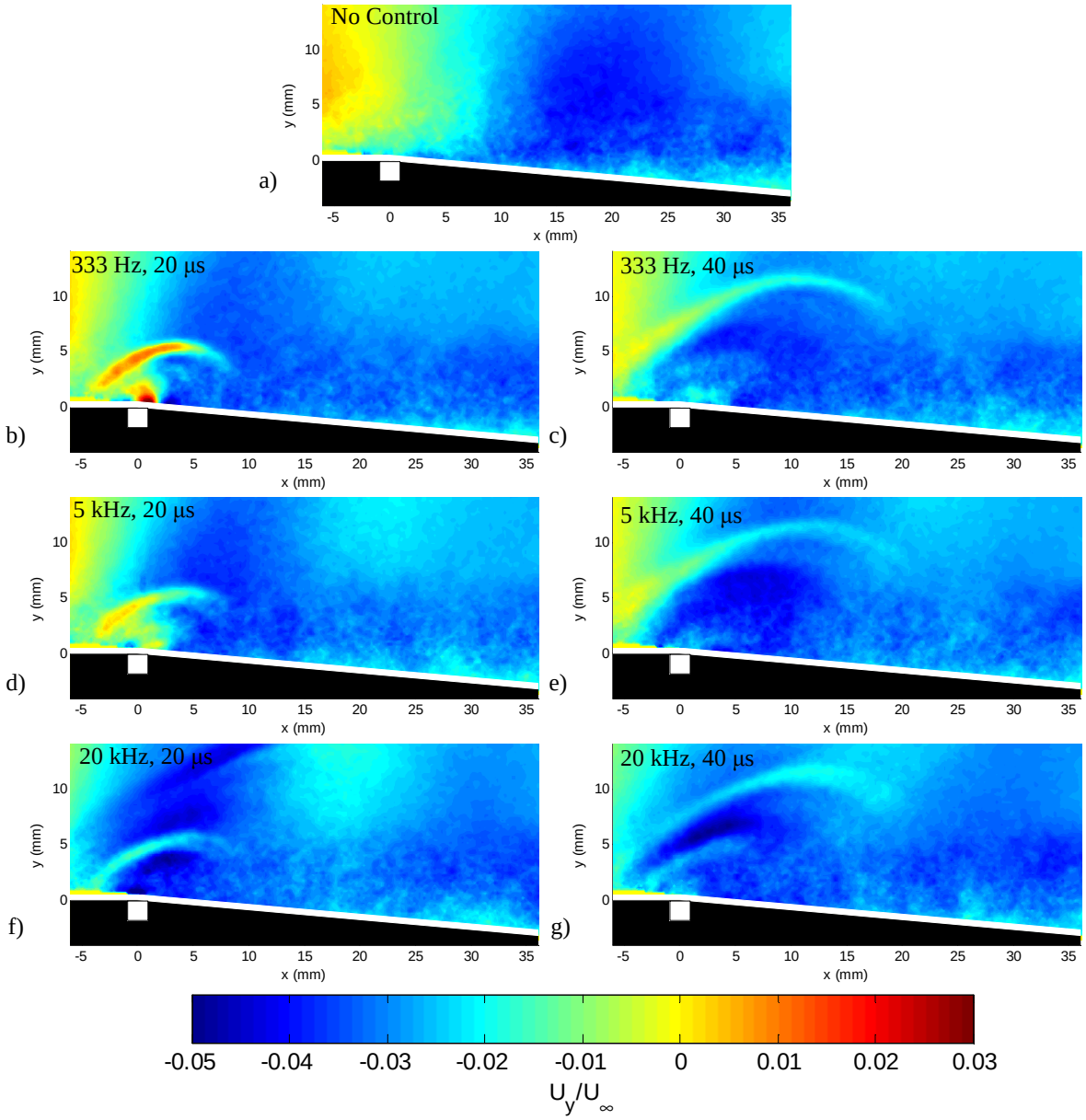

Fig. 3.30 Mean transverse velocity normalized by the freestream velocity for a) no control, b) LAFPA frequency of 333 Hz and delay time of 20 µs, c) LAFPA frequency of 333 Hz and delay time of 40 µs, d) LAFPA frequency of 5 kHz and delay time of 20 µs, e) LAFPA frequency of 5 kHz and delay time of 40 µs, f) LAFPA frequency of 20 kHz and delay time of 20 µs, and g) LAFPA frequency of 20 kHz and delay time of 40 µs.

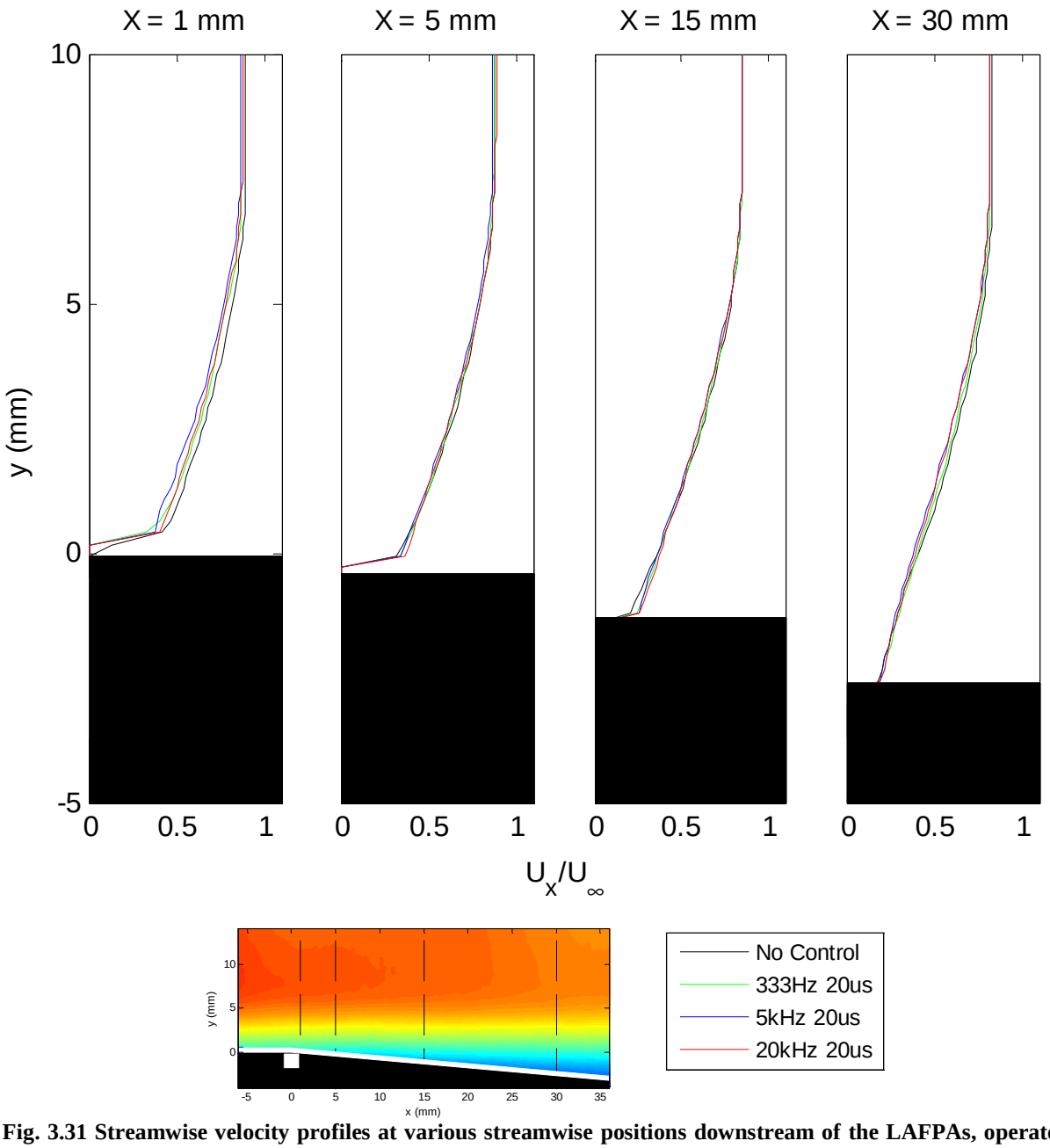

Fig. 3.31 Streamwise velocity profiles at various streamwise positions downstream of the LAFPAs, operated at various frequencies, at a delay time of 20 μs.

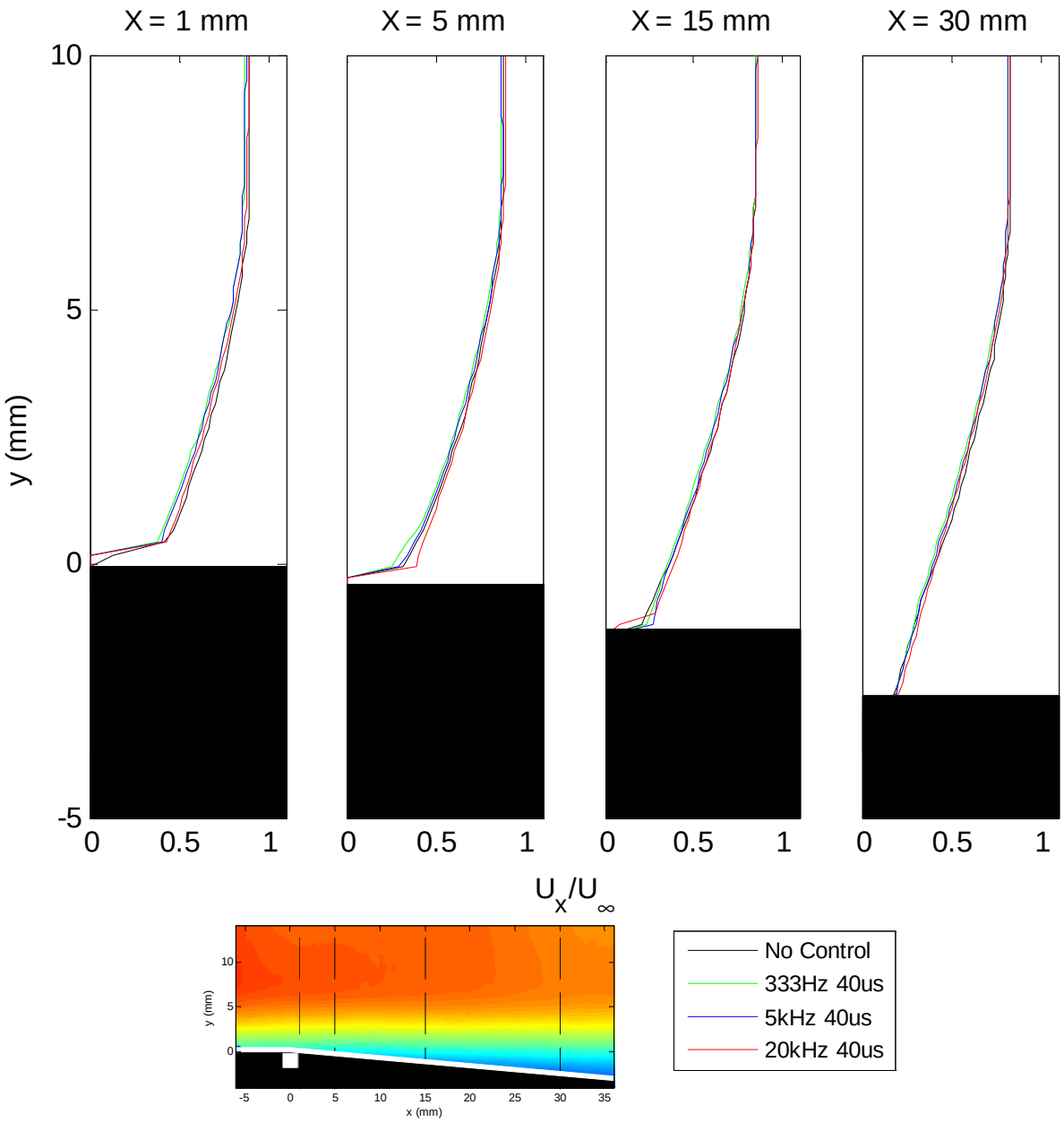

Fig. 3.32 Streamwise velocity profiles at various streamwise positions downstream of the LAFPAs, operated at various frequencies, at a delay time of 40 μs.

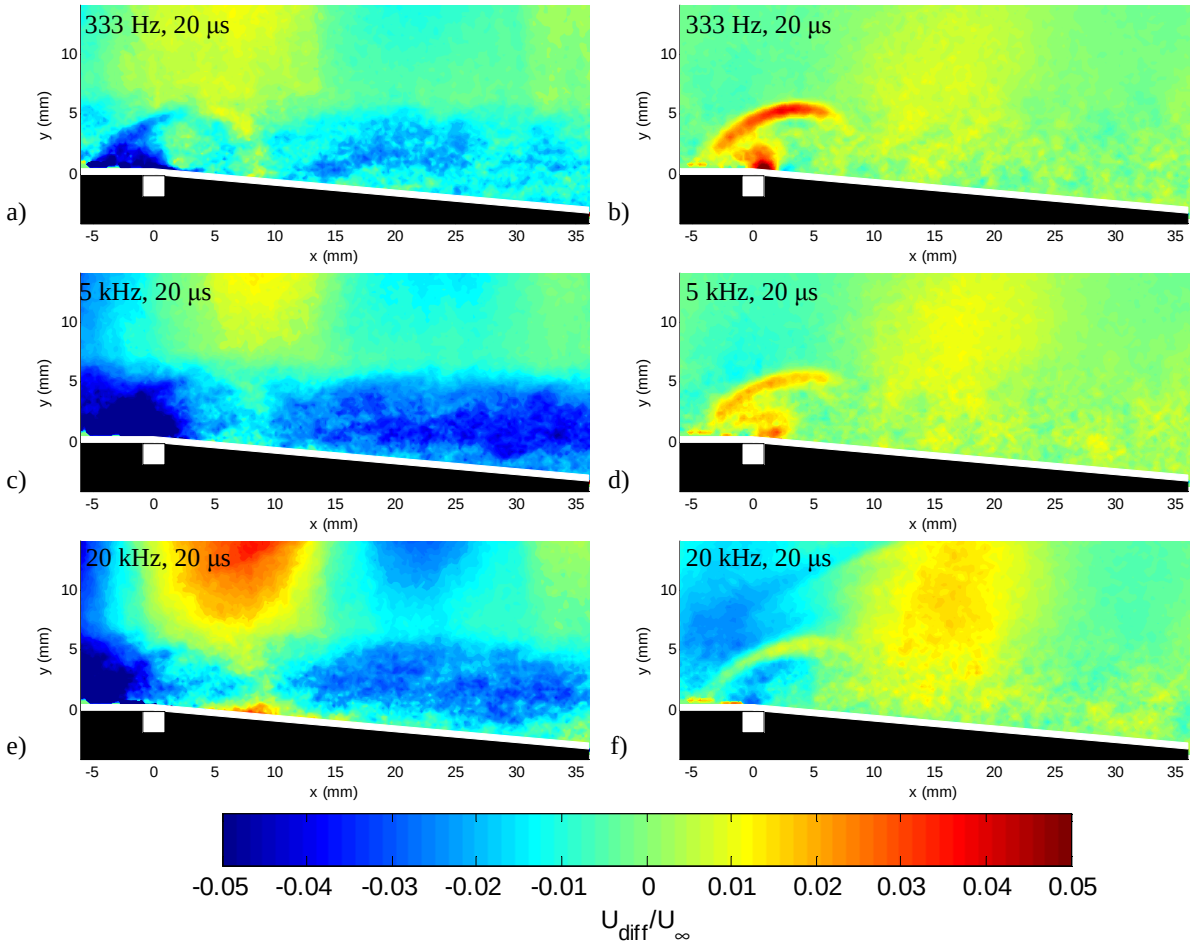

Fig. 3.33 Velocity difference between control cases and no control case, normalized by freestream velocity, at a delay time of 20 µs, for LAFPAs operated at various frequencies a-b) 333 Hz, c-d) 5 kHz, and e-f) 20 kHz. The left column is the difference in mean streamwise velocity, and the right column is the difference in mean transverse velocity (from the no control case).

4. Conclusions and Recommendations for Future Work

4.1 Conclusions

Two plasma-driven actuators were studied in order to determine their suitability for use as supersonic flow control devices. The first was a pulsed plasma jet, which used an arc discharge to drive a zero-net-mass-flux synthetic jet. The effects of a single pulse of the PPJ exhausted transversely into a Mach 3.0 boundary layer were investigated. The second device was a localized arc filament plasma actuator, which used an arc discharge to create periodic, virtual 'bumps' in the flow. An array of four of these actuators was placed in a Mach 1.4 crossflow and operated at various frequencies, in order to observe the effects on the normal shock stability, the boundary layer, and the boundary layer over a 5º diverging ramp.

The PPJ was investigated using PIV and voltage measurements. The voltage measurements revealed that the consistency of the arc breakdown is greatly improved when the actuator is placed in the low pressure environment created by the Mach 3.0 crossflow, as compared to the actuator exhausting into quiescent, atmospheric conditions. PIV revealed that the PPJ has minimal effect on the flow; weak disturbances in the streamwise velocity were produced by the jet, as well as a weak bow shock. The maximum peak velocity in the jet was about 9.8% of the freestream flow and occurred at around 20 µs after the initiation of the arc discharge. Over the entire pulse, the average peak velocity in the jet was about 4.7% of the freestream velocity. However, the strength and velocity fluctuated significantly over the course of the pulse; this 'chugging' behavior is believed to be due to complex wave interactions and reflections inside the PPJ cavity.

Schlieren imaging and PIV were used to investigate the effects of the LAFPAs. Schlieren imaging was used to determine the influence of the LAFPAs on the position and stability of the normal shock. The LAFPAs were studied both on and far upstream of the corner of a 5º diverging ramp. At both actuator locations, the LAFPAs were found to have virtually no effect on the position of the normal shock or on its stability, regardless of stagnation-to-exit pressure ratio, LAFPA frequency, or delay time. The Schlieren images also gave a qualitative view of the LAFPA's effects; a weak blast wave, created when the arc breakdown is initiated, was observed to grow outward and get pushed downstream by the crossflow. This blast wave appears to dissipate and become weaker in time.

PIV showed that the LAFPAs have a modest effect on both the boundary layer over the flat wall and the diverging ramp. They have virtually no effect on the streamwise velocity. In the transverse velocity, the blast wave can be seen and, at the lower frequencies, a plume of hot gas can also be observed. As seen in the Schlieren images, the blast wave moves outward and downstream with time. Additionally, the strength of the blast wave decreases with increasing frequency, which is believed to be

due to the shorter time between discharges reducing the amount of cooling and refilling the actuator cavity experiences. The hot gas plume also decreases in strength with increasing frequency, for the same reason as the blast wave, and is not even visible at the highest frequencies. These disturbances do not have a large impact on the boundary layer, over the flat wall or the diverging ramp. If anything, they appear to make the boundary layer velocity profile less full, but only very close to the actuators and at the earliest delay times. This indicates that instead of adding momentum to the boundary layer, the actuators actually reduce the momentum close to the wall. However, the differences in the velocity profiles are very small, and when considering the uncertainty in the velocity measurements, it is questionable whether those differences are a real or significant effect.

Overall, neither of these actuators, in their present configurations, had a significant or useful effect on these supersonic crossflows. However, with some adjustment in configuration, more tuning to flow instability frequencies, and/or a different flowfield/flow conditions, either of these actuators could be more effective.

4.2 Recommendations for Future Work

In this work, only a single pulse of the PPJ was investigated, and it was found to have extremely modest effects. In the future, it may be useful to increase and tune the frequency of the PPJ to a natural instability in the flow in order to excite or suppress that instability. Additionally, an array of actuators may provide a more significant, distributed, and useful effect on a flow. Observing the PPJ's effects on other flows, such as a shock/boundary layer interaction, may show more useful results as well.

The LAFPAs in this work were investigated at various frequencies, but the frequency studied the most in depth (333 Hz) corresponded to a Strouhal number based on the "shock foot", which was the length over which the normal shock oscillated with no control (approximately the standard deviation of the shock position with no control). In the future, it may be beneficial to more completely understand the nature of the instability that causes the shock position to vary, determine the relevant length scales, and tune the frequency of the actuators to a Strouhal number based on that length scale.

For both actuators it may also be interesting to investigate any three-dimensional effects, especially when an array is used, and to use high-speed diagnostic techniques in order to observe their behavior at higher time resolution. Additionally, parametric studies for both actuators should be done in order to optimize their geometries and circuit designs.

References

M. Amitay, B. L. Smith, and A. Glezer, "Aerodynamic Flow Control Using Synthetic Jet Technology," *36th AIAA Aerospace Sciences Meeting,* AIAA 98-0208, 1998

M. Amitay, V. Kibens, D. Parekh, and A. Glezer, "The Dynamics of Flow Reattachment Over a Thick Airfoil Controlled by Synthetic Jet Actuators," *37th AIAA Aerospace Sciences Meeting,* AIAA 99-1001, 1999

K. Anderson and D. Knight, "Characterization of Single Pulse of Plasma Jet," *50th AIAA Aerospace Sciences Meeting,* AIAA 2012-0188, 2012

E. Caraballo, N. Webb, J. Little, J. H. Kim, and M. Samimy, "Supersonic Inlet Flow Control Using Plasma Actuators," *47th AIAA Aerospace Sciences Meeting,* AIAA 2009-924, 2009

D. Caruana, P. Barricau, P. Hardy, J. P. Cambronne, and A. Belinger, "The 'Plasma Synthetic Jet' Actuator: Aero-thermodynamic Characterization and First Flow Control Applications," *47th AIAA Aerospace Sciences Meeting,* AIAA 2009-1307, 2009

N. T. Clemens and V. Narayanaswamy, "Shock/Turbulent Boundary Layer Interactions: Review of Recent Work on Sources of Unsteadiness," *39th AIAA Fluid Dynamics Conference,* AIAA 2009-3710, 2009

T. C. Corke, C. L. Enloe, and S. P. Wilkinson, "Dielectric Barrier Discharge Plasma Actuators for Flow Control," *Annual Review of Fluid Mechanics,* vol. 42, pp. 505-529, 2010

T. Crittenden, A. Glezer, R. Funk, and D. E. Parekh, "Combustion-Driven Jet Actuators for Flow Control," *31st AIAA Fluid Dynamics Conference,* AIAA 2001-2768, 2001

B. Z. Cybyk, D. H. Simon, H. B. Land III, J. Chen, and J. Katz, "Experimental Characterization of a Supersonic Flow Control Actuator," *44th AIAA Aerospace Sciences Meeting,* AIAA 2006-478, 2006

B. G. DeBlauw, E. Lazar, N. Kale, N. Glumac, C. Dutton, and G. Elliott, "Flow and Thermal Properties Induced by Electric Arc Plasma Actuators," *49th AIAA Aerospace Sciences Meeting,* AIAA 2011-734, 2011

B. G. DeBlauw, “Active Control of Massively Separated High-Speed/Base Flows with Electric Arc Plasma Actuators,” Ph.D. Dissertation, Department of Aerospace Engineering, University of Illinois at Urbana-Champaign, Urbana, IL, 2012

F. J. Diez-Garias, W. J. A. Dahm, and P. H. Paul, “Microactuator Arrays for Sublayer Control in Turbulent Boundary Layers Using the Electrokinetic Principle,” *38th AIAA Aerospace Sciences Meeting*, AIAA 2000-0548, 2000

P. Dupont, C. Haddad, and J. F. Debieve, “Space and Time Organization in a Shock-Induced Separated Boundary Layer,” *Journal of Fluid Mechanics*, vol. 559, pp. 255-277, 2006

H. H. Fernholz and P. J. Finley, "A Critical Commentary on Mean Flow Data for Two-Dimensional Compressible Turbulent Boundary Layers," *AGARDograph* 223, 1980

A. Fridman and L. A. Kennedy, *Plasma Physics and Engineering*, Taylor & Francis, New York, NY, 2004, Ch. 7, 8

M. Gad-el-hak, “Modern Developments in Flow Control,” *Applied Mechanics Reviews*, vol. 49, pp. 365-379, 1996

A. Glezer, M. Allen, D. Coe, B. Smith, M. Trautman and J. Wiltse, "Synthetic Jet Actuator and Application Thereof," US Patent 5,758,823, 02 June 1998

K. Grossman, B. Cybyk and D. VanWie, "Sparkjet Actuators for Flow Control," *41st AIAA Aerospace Sciences Meeting*, AIAA 2003-57, 2003

K. R. Grossman, B. Z. Cybyk, M. C. Rigling and D. M. VanWie, "Characterization of Sparkjet Actuators for Flow Control," *42nd AIAA Aerospace Sciences Meeting*, AIAA 2004-89, 2004

T. Herges, E. Kroeker, G. Elliott, and C. Dutton, “Microramp Flow Control of Normal Shock/Boundary-Layer Interactions,” *AIAA Journal*, vol. 48, no. 11, 2010

C. M. Ho and Y. C. Tai, “Review: MEMS and its Applications for Flow Control,” *Journal of Fluids Engineering*, vol. 118, pp. 437-447, 1996

T. Kouchi, K. Sasaya, J. Watanabe, H. Sibayama and G. Masuya, "Penetration Characteristics of Pulsed Injection into Supersonic Crossflow," *46th AIAA/ASME/SAE/ASEE Joint Propulsion Conference*, AIAA 2010-6645, 2010

N. V. Kale, “Active and Hybrid Flow Control in S-Ducts and Diffusers,” Ph.D. Dissertation, Department of Aerospace Engineering, University of Illinois at Urbana-Champaign, Urbana, IL, 2013

L. D. Kral, “Active Flow Control Technology,” *ASME Fluids Engineering Division Technical Brief*, 1998

E. Lazar, B. DeBlauw, N. Glumac, C. Dutton and G. Elliott, "A Practical Approach to PIV Uncertainty Analysis," *27th AIAA Aerodynamic Measurement Technology and Ground Testing Conference*, AIAA 2010-4355, 2010

S. O. Macheret, M. N. Shneider, and R. B. Miles, “Magnetohydrodynamic and Electrohydrodynamic Control of Hypersonic Flows of Weakly Ionized Plasmas,” *AIAA Journal*, vol. 42, no. 7, 2004

K. McManus, A. Cucharme, C. Goldey, and J. Magill, “Pulsed Jet Actuators for Suppressing Flow Separation,” *34th AIAA Aerospace Sciences Meeting*, AIAA 96-0442, 1996

V. Narayanaswamy, L. Raja and N. Clemens, "Characterization of a High-Frequency Pulsed-Plasma Jet Actuator for Supersonic Flow Control," *AIAA Journal*, vol. 48, pp. 297-305, 2010

H. Randolph, L. Chew and H. Johar, "Pulsed Jets in Supersonic Crossflow," *Journal of Propulsion and Power*, vol. 10, no. 5, pp. 746-748, 1994

T. Reedy, N. Kale, J. C. Dutton and G. Elliott, "Experimental Characterization of a Pulsed Plasma Jet," *50th AIAA Aerospace Sciences Meeting*, AIAA 2012-904, 2012

T. M. Reedy, “Control of Supersonic Axisymmetric Base Flows Using Passive Splitter Plates and Pulsed Plasma Actuators,” Ph.D. Dissertation, Mechanical Science and Engineering Department, University of Illinois at Urbana-Champaign, Urbana, IL, 2013

J. R. Roth, “Aerodynamic Flow Acceleration Using Paraelectric and Peristaltic Electrohydrodynamic Effects of a One Atmosphere Uniform Glow Discharge Plasma,” *Physics of Plasmas*,vol. 10, no. 5, 2003

M. Rybalko, H. Babinsky, and E. Loth, “Vortex Generators for a Normal Shock/Boundary-Layer Interaction with a Downstream Diffuser,” *Journal of Propulsion and Power*, vol. 28, no. 1, 2012

M. Samimy and S. K. Lele, "Motion of Particles with Inertia in a Compressible Free Shear Layer," *Physics of Fluids*, vol. 3, no. 8, 1991

M. Samimy, I. Adamovich, B. Webb, J. Kastner, J. Hileman, S. Keshav, and P. Palm, “Development and Application of Localized Arc Filament Plasma Actuators for Jet Flow and Noise Control,” *42nd AIAA Aerospace Sciences Meeting*, AIAA 2004-184, 2004

M. Samimy, J. H. Kim, J. Kastner, I. Adamovich, and Y. Utkin, “Active Control of High-Speed and High-Reynolds-Number Jets Using Plasma Actuators,” *Journal of Fluid Mechanics*, vol. 578, pp. 305-330, 2007

B. O. Sanders, “Characterization of Thermo-Chemical Properties of Electric Arc Plasma Actuators,” M.S. Thesis, Mechanical Science and Engineering Department, University of Illinois at Urbana-Champaign, Urbana, IL, 2012

A. Seifert, T. Bachar, D. Koss, M. Shepshelovich, and I. Wygnanski, “Oscillatory Blowing: A Tool to Delay Boundary-Layer Separation,” *AIAA Journal*, vol. 31, no. 11, 1993

A. Seifert and L. G. Pack, “Oscillatory Control of Separation at High Reynolds Numbers,” *AIAA Journal*, vol. 37, no. 9, 1999

J. Shin, V. Narayanaswamy, L. L. Raja, and N. T. Clemens, “Characterization of a Direct-Current Glow Discharge Plasma Actuator in Low-Pressure Supersonic Flow,” *AIAA Journal*, vol. 45, no. 7, 2007

J. Shin and S. Mahadevan, “Forcing mechanisms in supersonic flow actuation achieved by direct-current surface glow discharge plasma,” *Aerospace Science and Technology*, vol. 15, pp. 18-24, 2011

B. L. Smith and A. Glezer, "The Formation and Evolution of Synthetic Jets," *Physics of Fluids,* vol. 10, no. 9, 1998

C. C. Sun and M. E. Childs, "A Modified Wall Wake Velocity Profile for Turbulent Compressible Boundary Layers," *Journal of Aircraft,* vol. 10, pp. 381-383, 1973

Y. G. Utkin, S. Keshav, J. H. Kim, J. Kastner, I. V. Adamovich, and M. Samimy, "Development and Use of Localized Arc Filament Plasma Actuators for High-Speed Flow Control," *Journal of Physics D: Applied Physics,* vol. 40, pp. 685-694, 2007

N. Webb, C. Clifford, and M. Samimy, "Control of Oblique Shock Wave-Boundary Layer Interactions Using Plasma Actuators," *6th AIAA Flow Control Conference,* AIAA 2012-2810, 2012

N. Webb, C. Clifford, and M. Samimy, "An Investigation of the Control Mechanism of Plasma Actuators in a Shock Wave-Boundary Layer Interaction," *51st AIAA Aerospace Sciences Meeting,* AIAA – 2013-0402, 2013

I. Wygnanski, "Boundary Layer and Flow Control by Periodic Addition of Momentum," *4th Shear Flow Control Conference,* AIAA 1997-2117, 1997

K. B. M. Q. Zaman and A. K. M. F. Hussain, "Turbulence Suppression in Free Shear Flows by Controlled Excitation," *Journal of Fluid Mechanics,* vol. 103, pp. 133-159, 1981

Appendix

This appendix contains technical drawings for the wind tunnel test section floor and actuator components used in this work. It is organized into three sections, one for the PPJ test section components and two for the LAFPA test section components, one for each actuator position. Each section begins with drawings of the complete wind tunnel bottom wall assembly and these are followed with drawings of each of the parts included in the assembly. The parts used for both LAFPA assemblies are only shown once, in the first LAFPA section.

A.1 PPJ Part Drawings

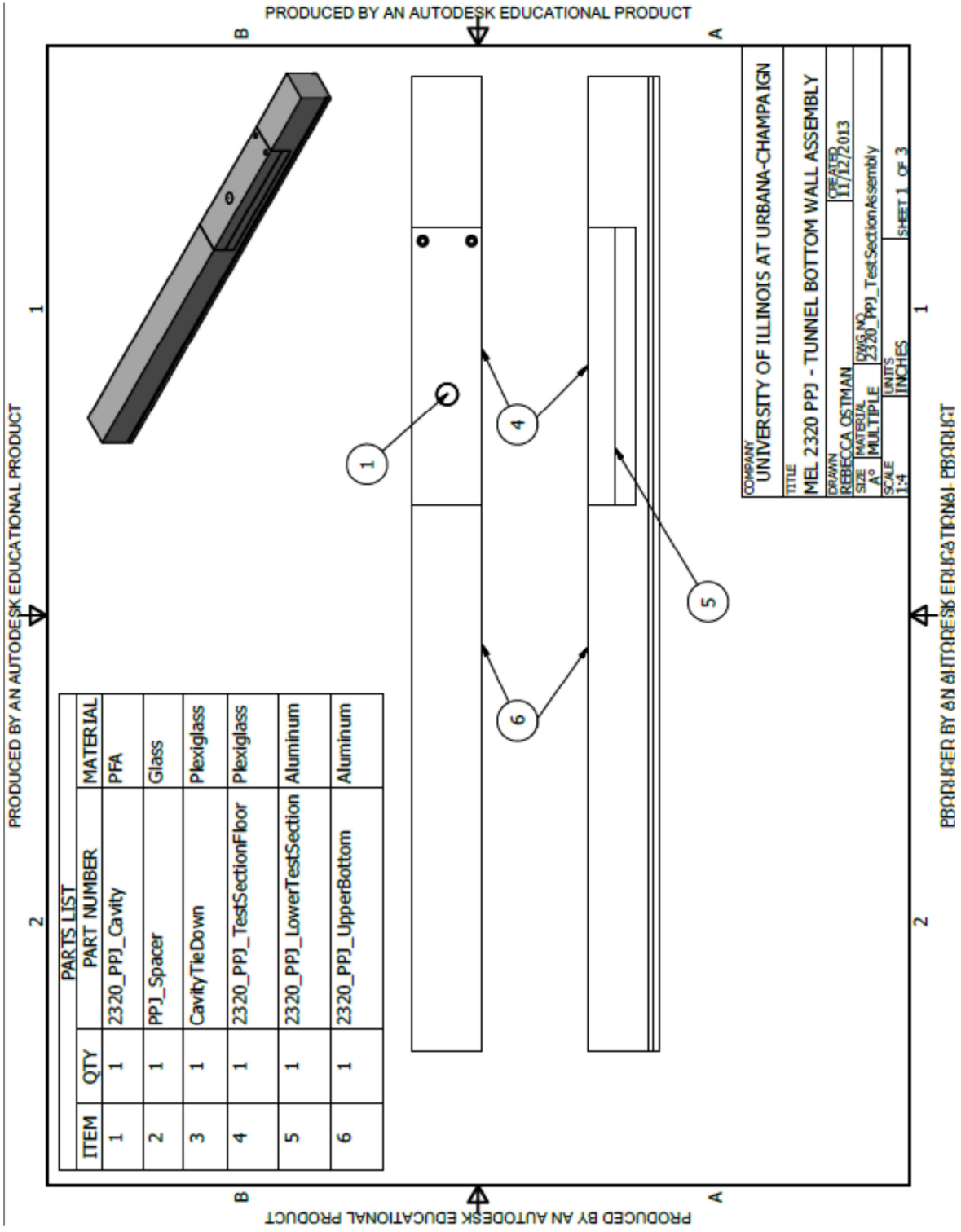

Fig. A.1 a) Base views and parts list for the PPJ assembly,

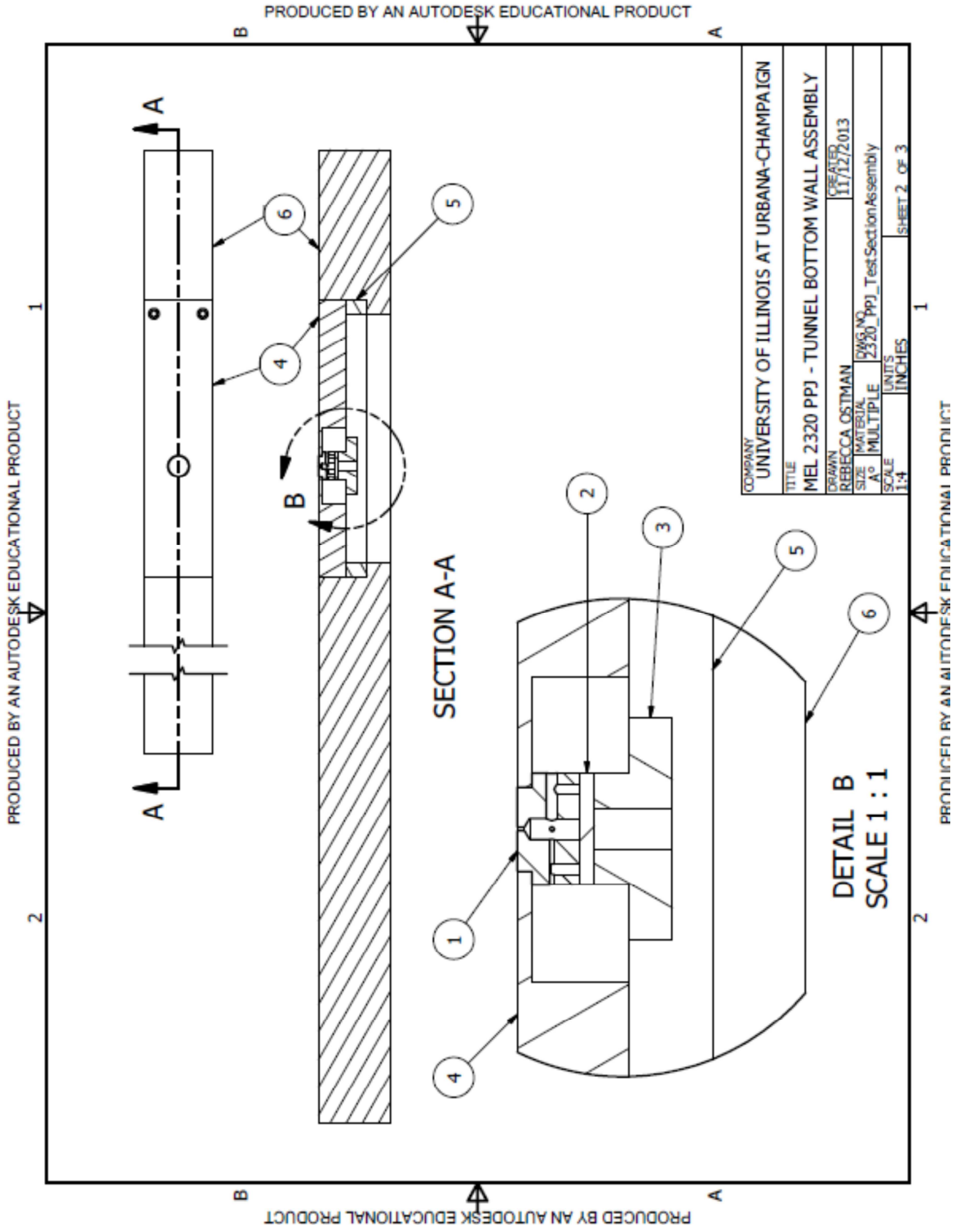

Fig. A.1 (cont.) b) cross section and detail views of PPJ assembly,

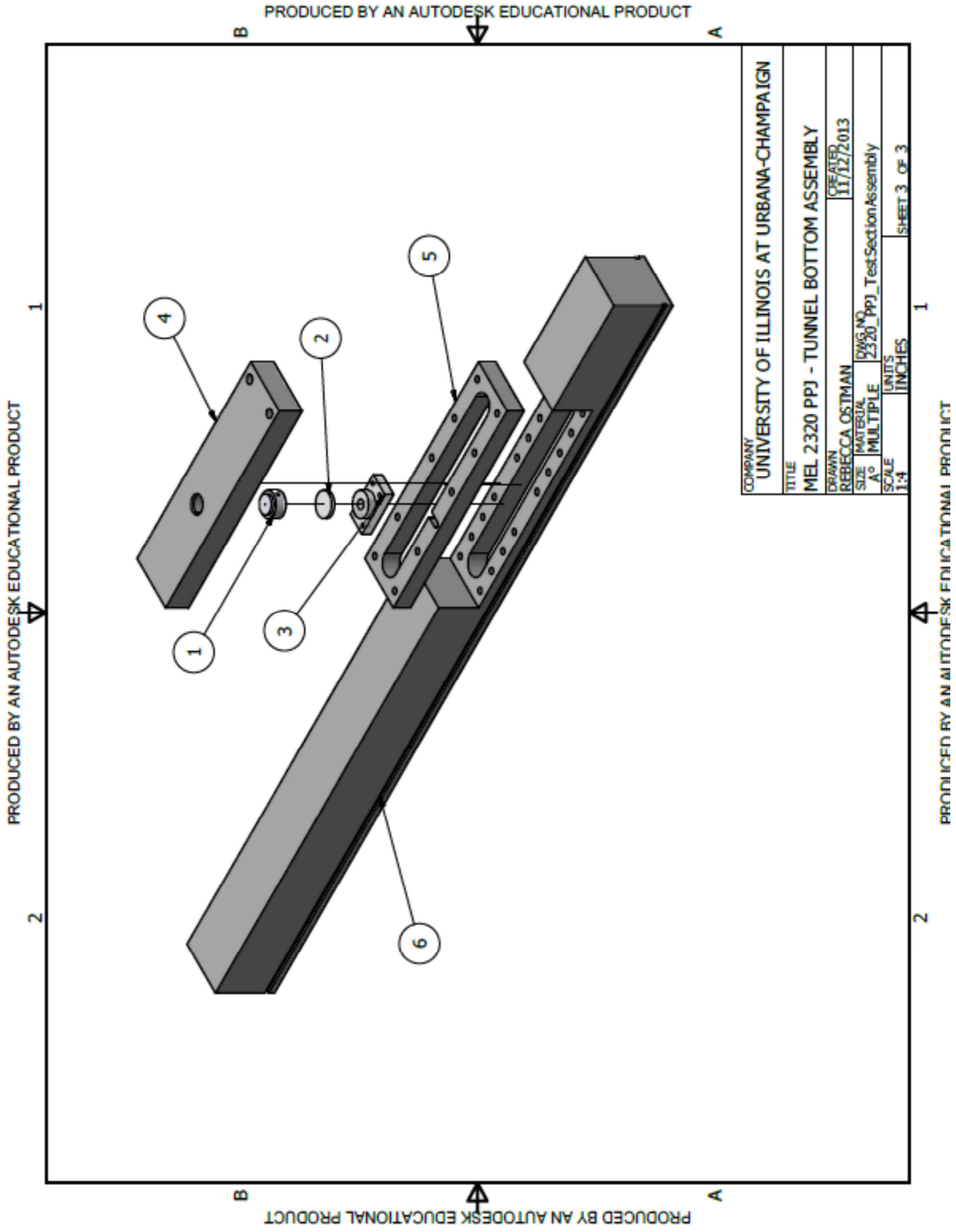

Fig. A.1 (cont.) c) exploded view of PPJ assembly.

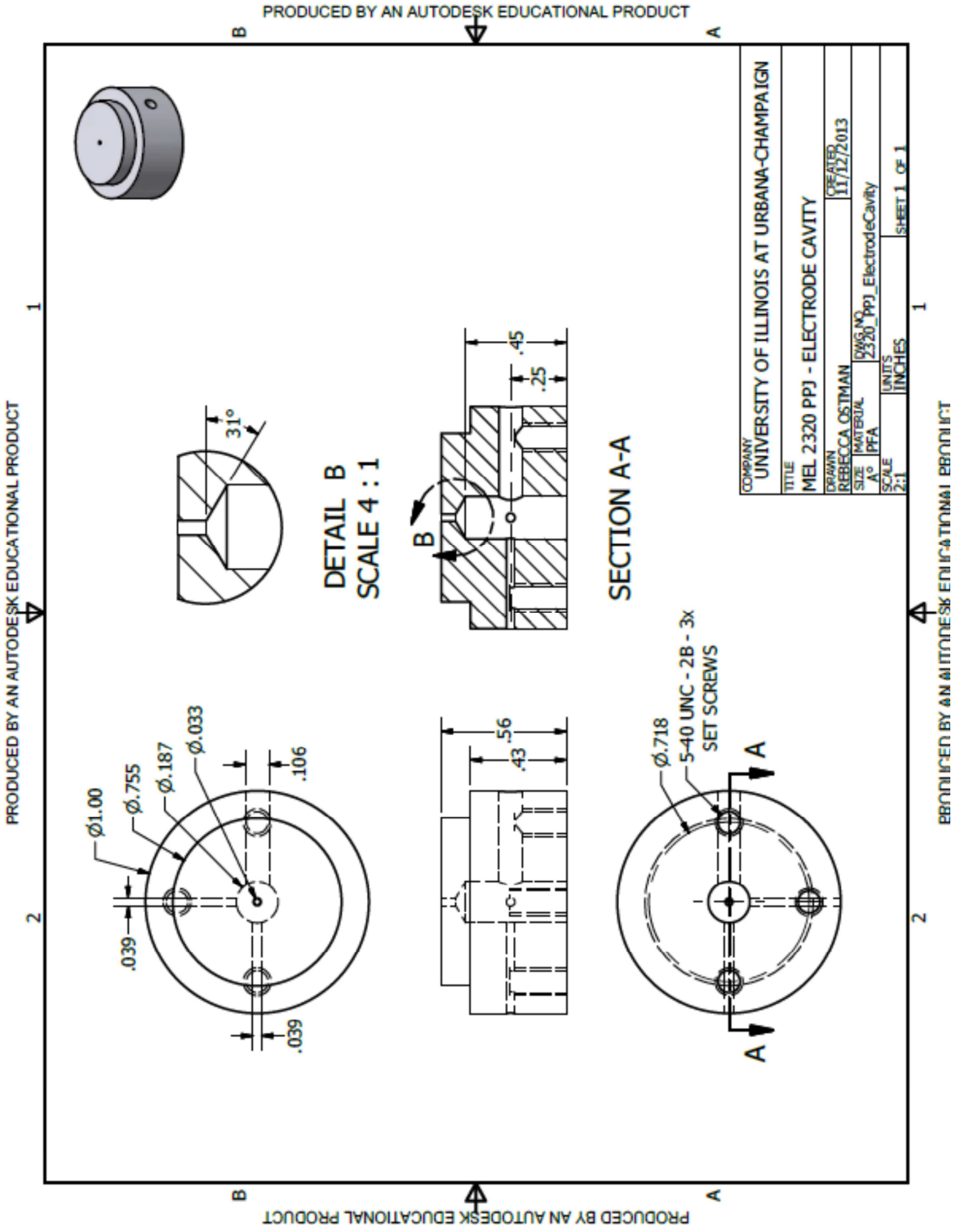

Fig. A.2 Drawing and specifications for the PPJ cavity and electrode housing.

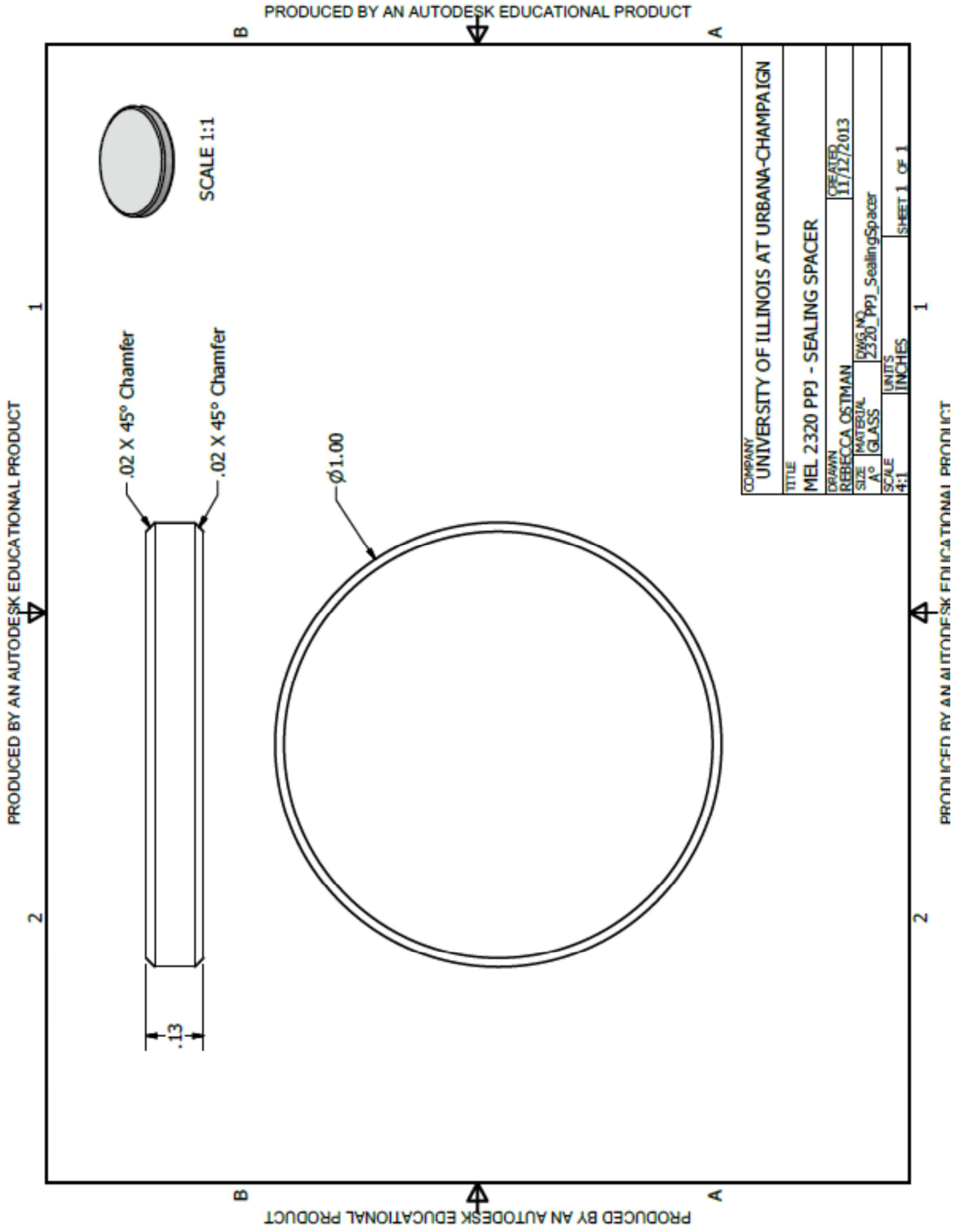

Fig. A.3 Drawing and specifications for the spacer between the cavity housing and its tie-down piece, also used to seal the cavity.

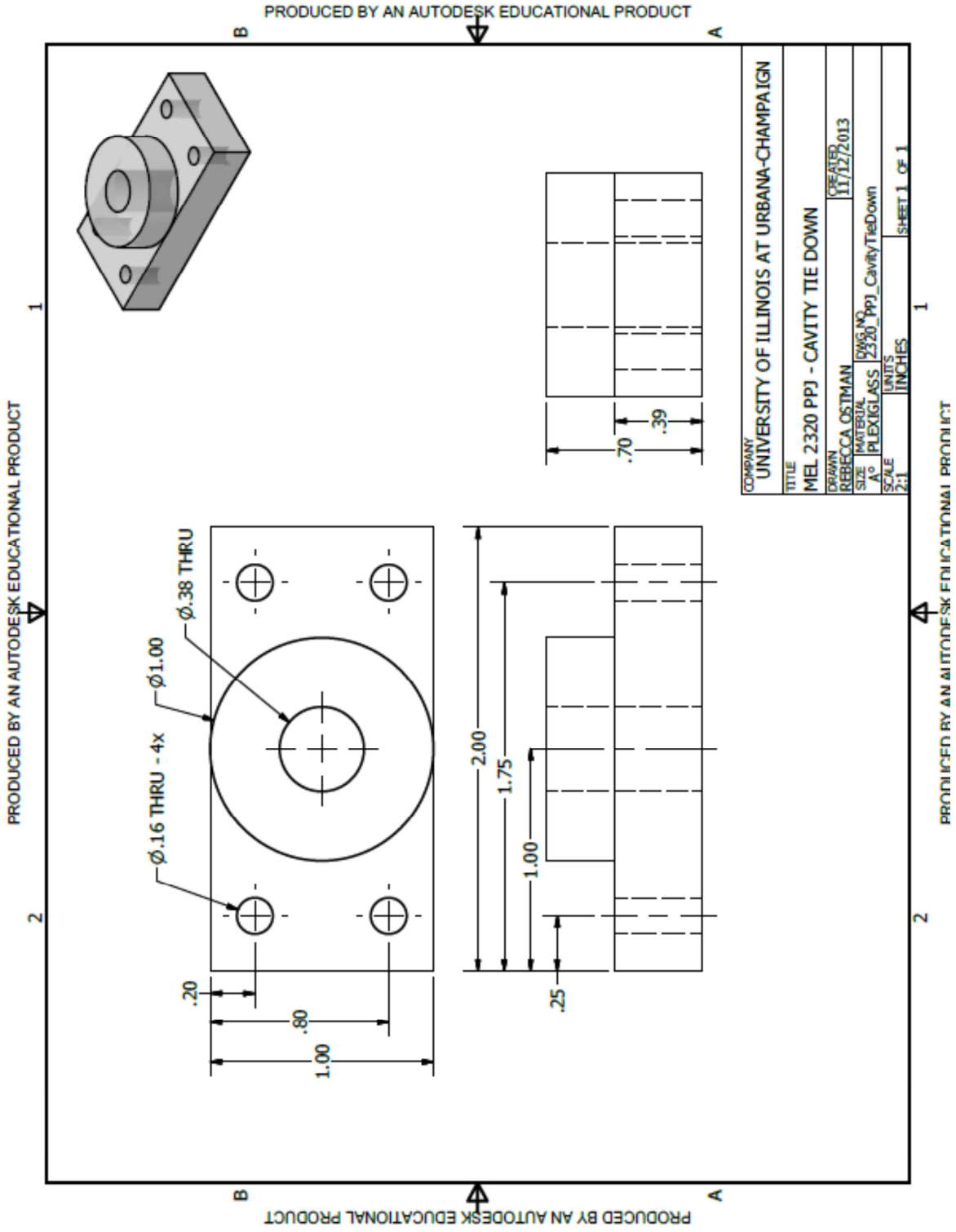

Fig. A.4 Drawing and specifications for the tie-down piece for the electrode cavity.

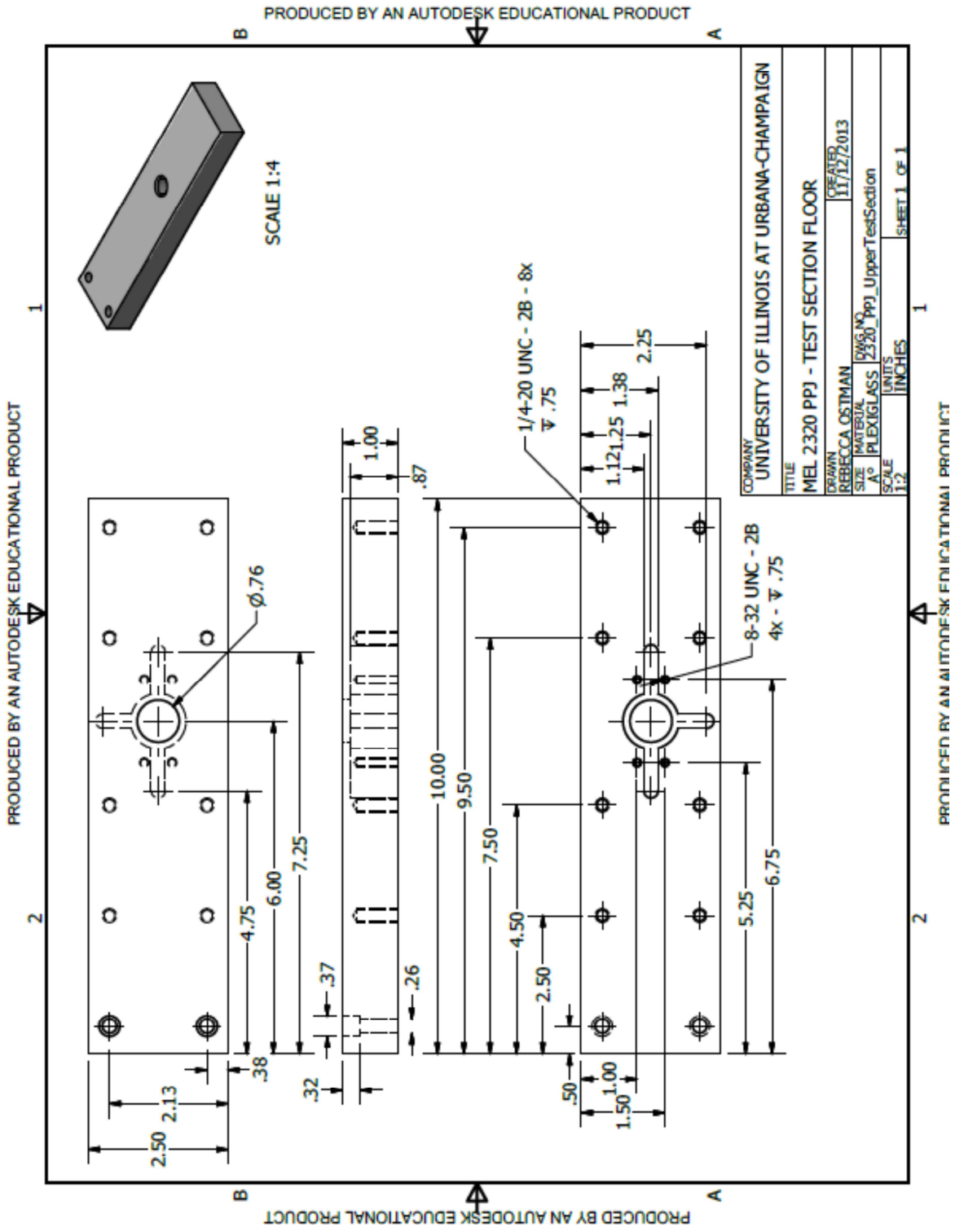

Fig. A.5 Drawing and specifications for the test section floor.

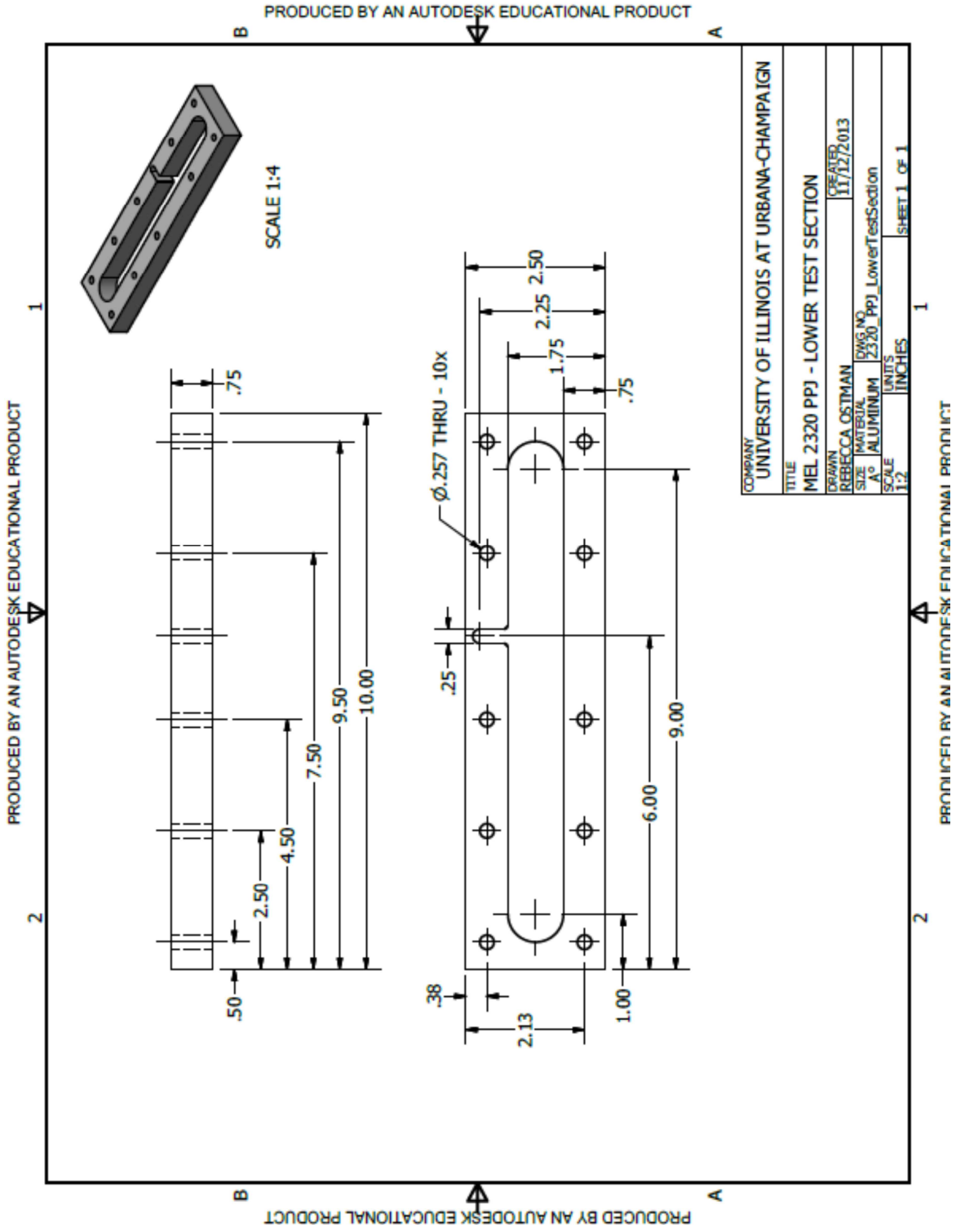

Fig. A.6 Drawing and specifications for the part below the test section floor.

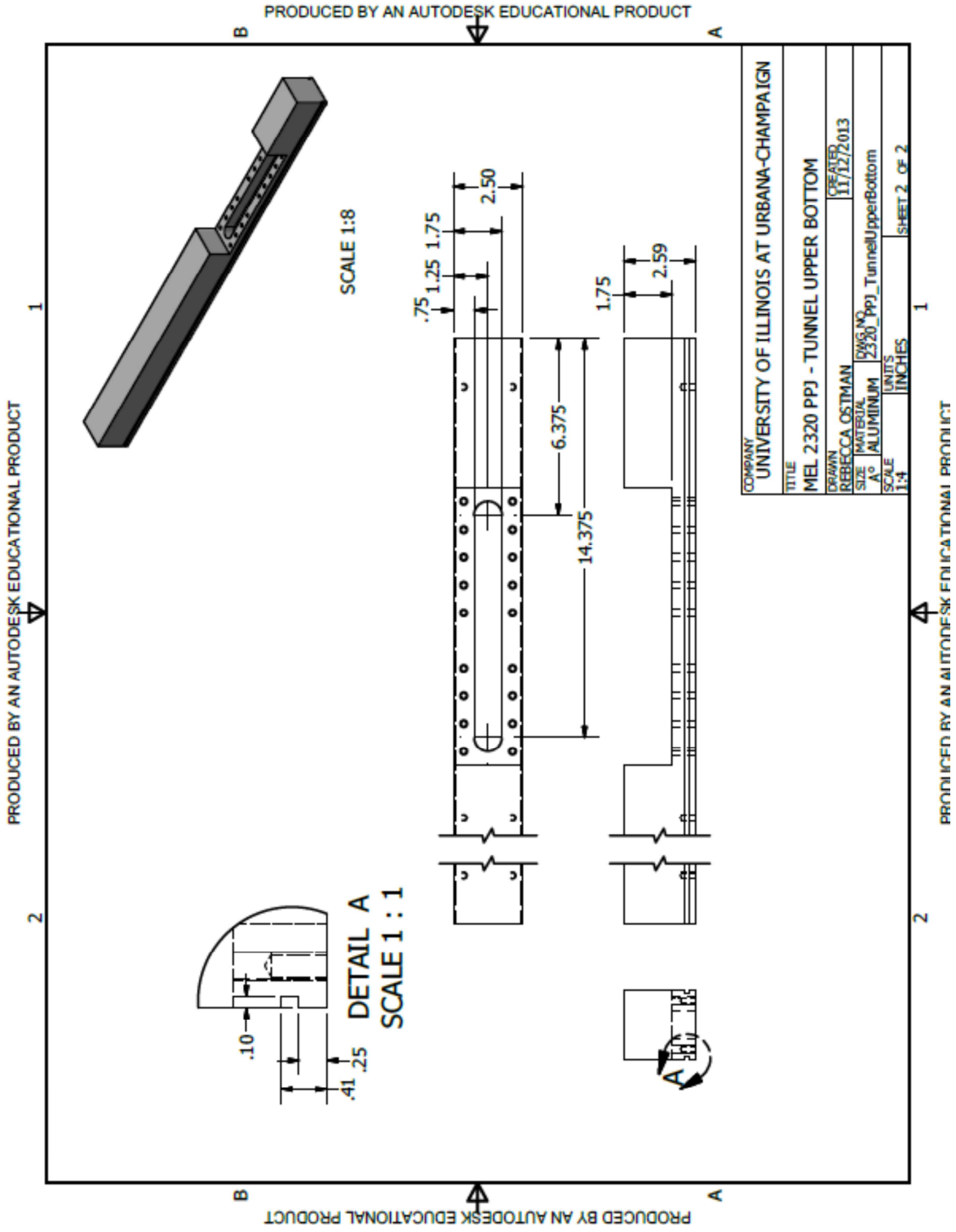

Fig. A.7 a) First sheet of drawing and specifications for the bottom wall of the wind tunnel,

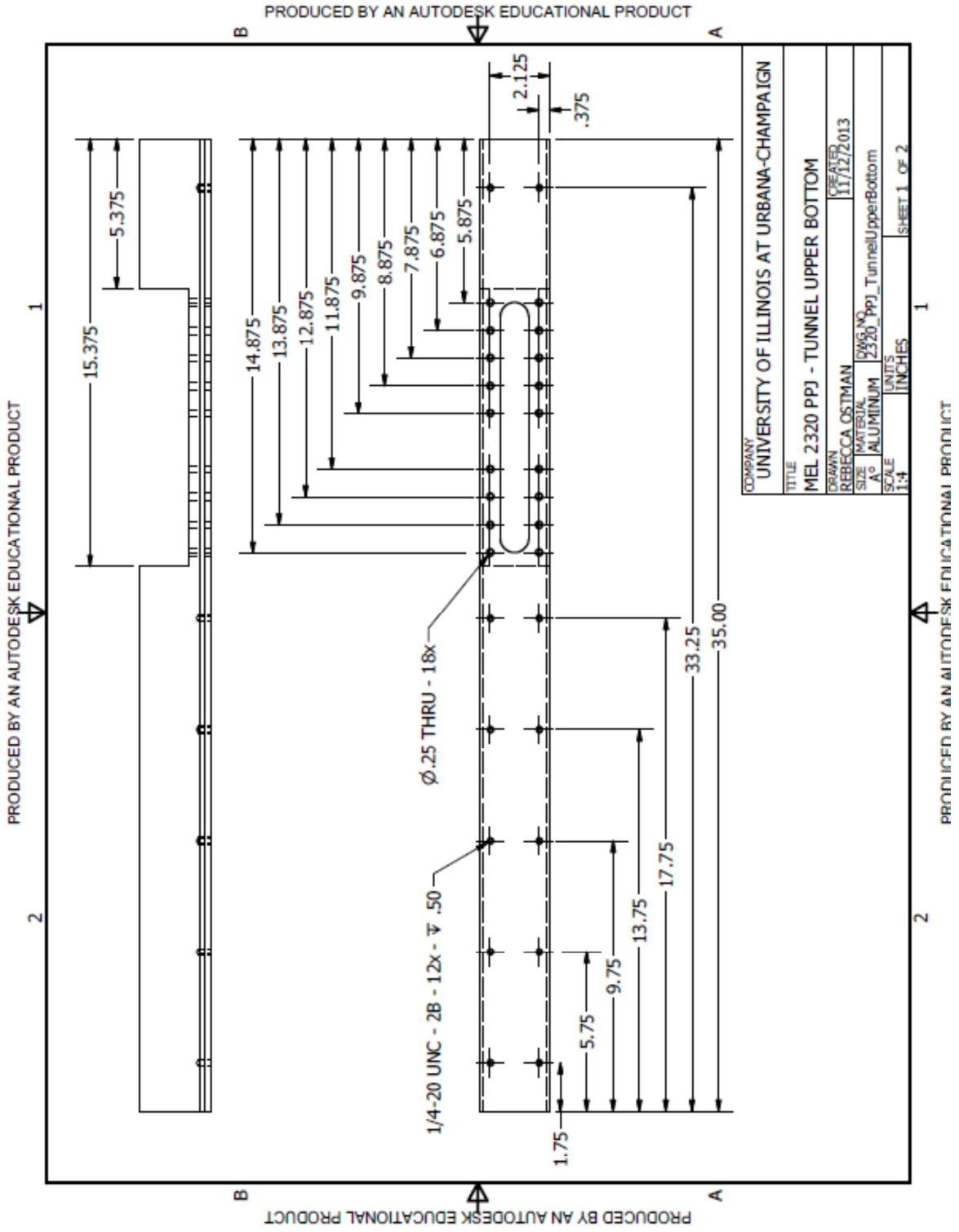

Fig. A.7 (cont.) b) second sheet of the drawing and specifications for the bottom wall of the wind tunnel, detailing the hole pattern.

A.2 LAFPAs Upstream of Ramp Corner Part Drawings

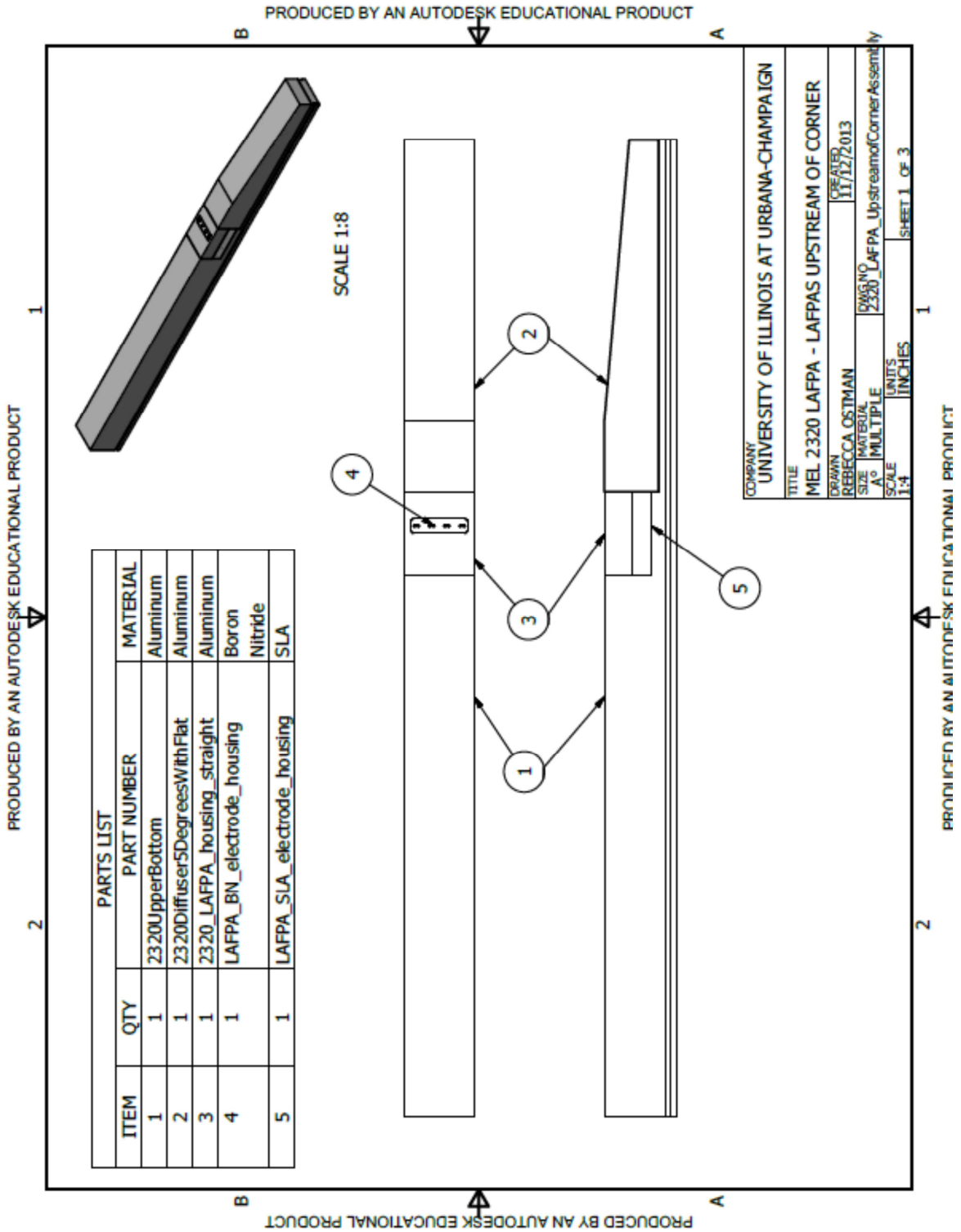

Fig. A.8 a) Base views and parts list for the LAFPAs upstream of the ramp corner assembly,

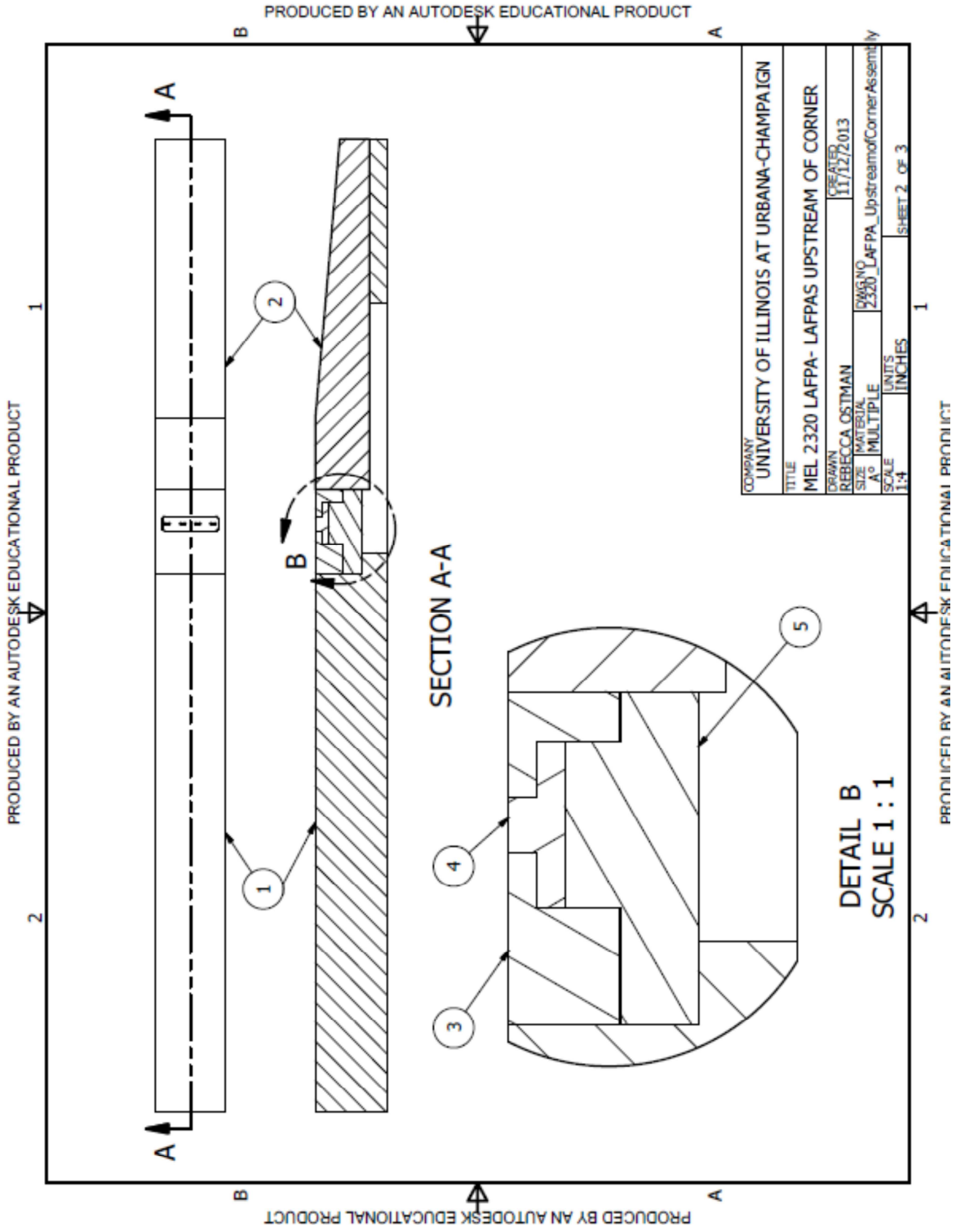

Fig. A.8 (cont.) b) cross section and detail views of the LAFPAs upstream of ramp corner assembly,

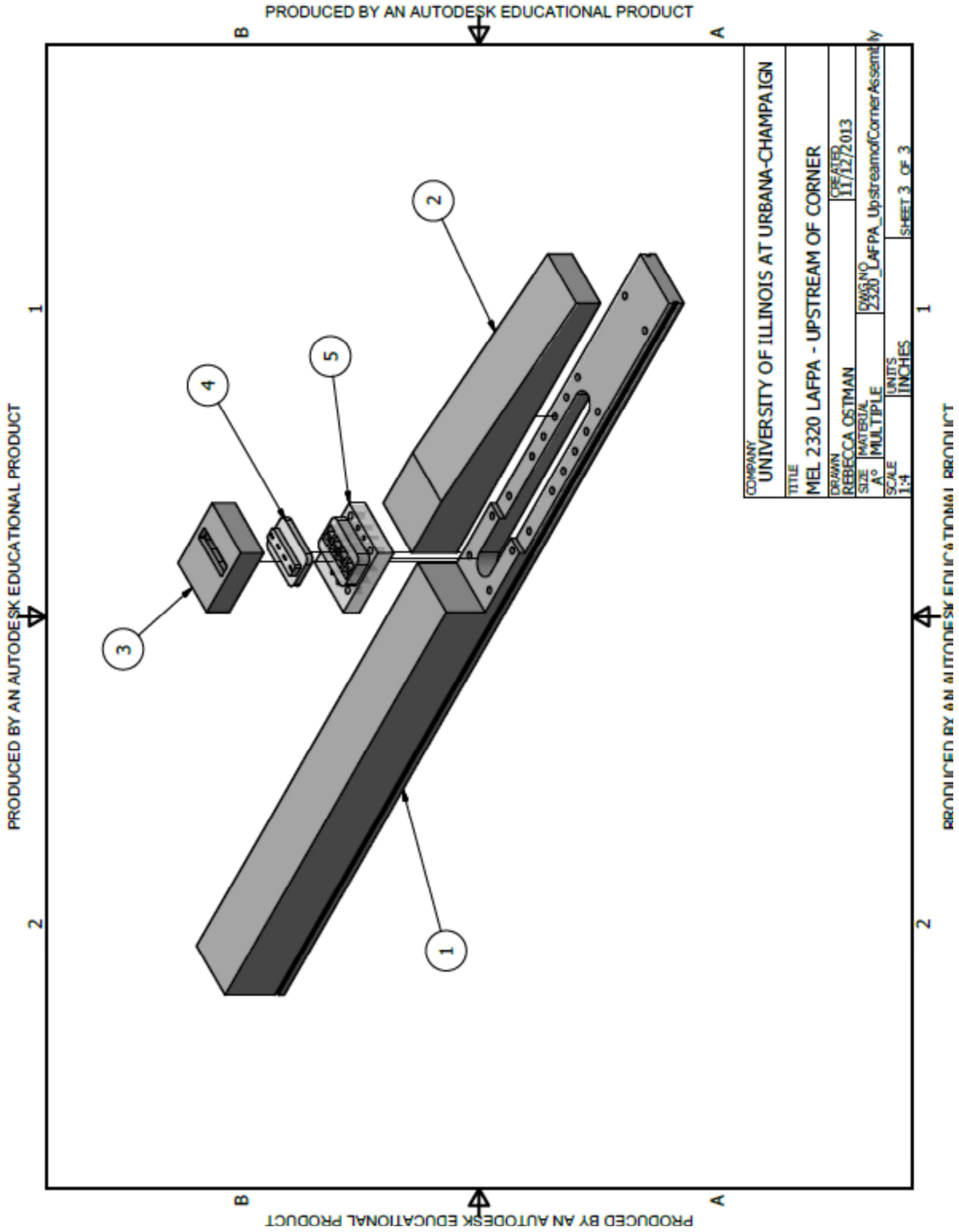

Fig. A.8 (cont.) c) exploded view of LAFPAs upstream of ramp corner assembly.

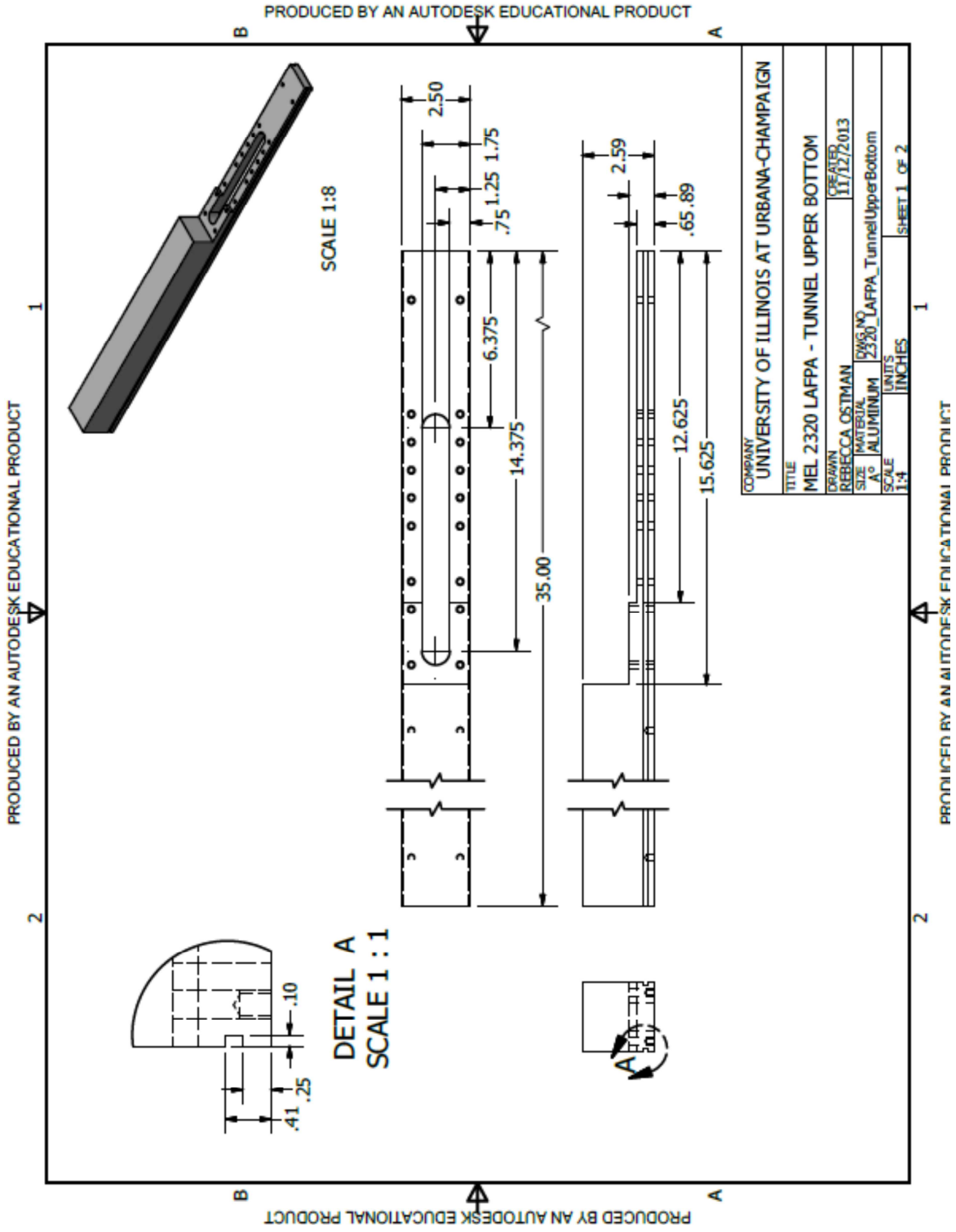

Fig. A.9 a) First sheet of the drawing and specifications for the bottom wall of the wind tunnel for both the LAFPAs upstream and on the ramp corner assemblies,

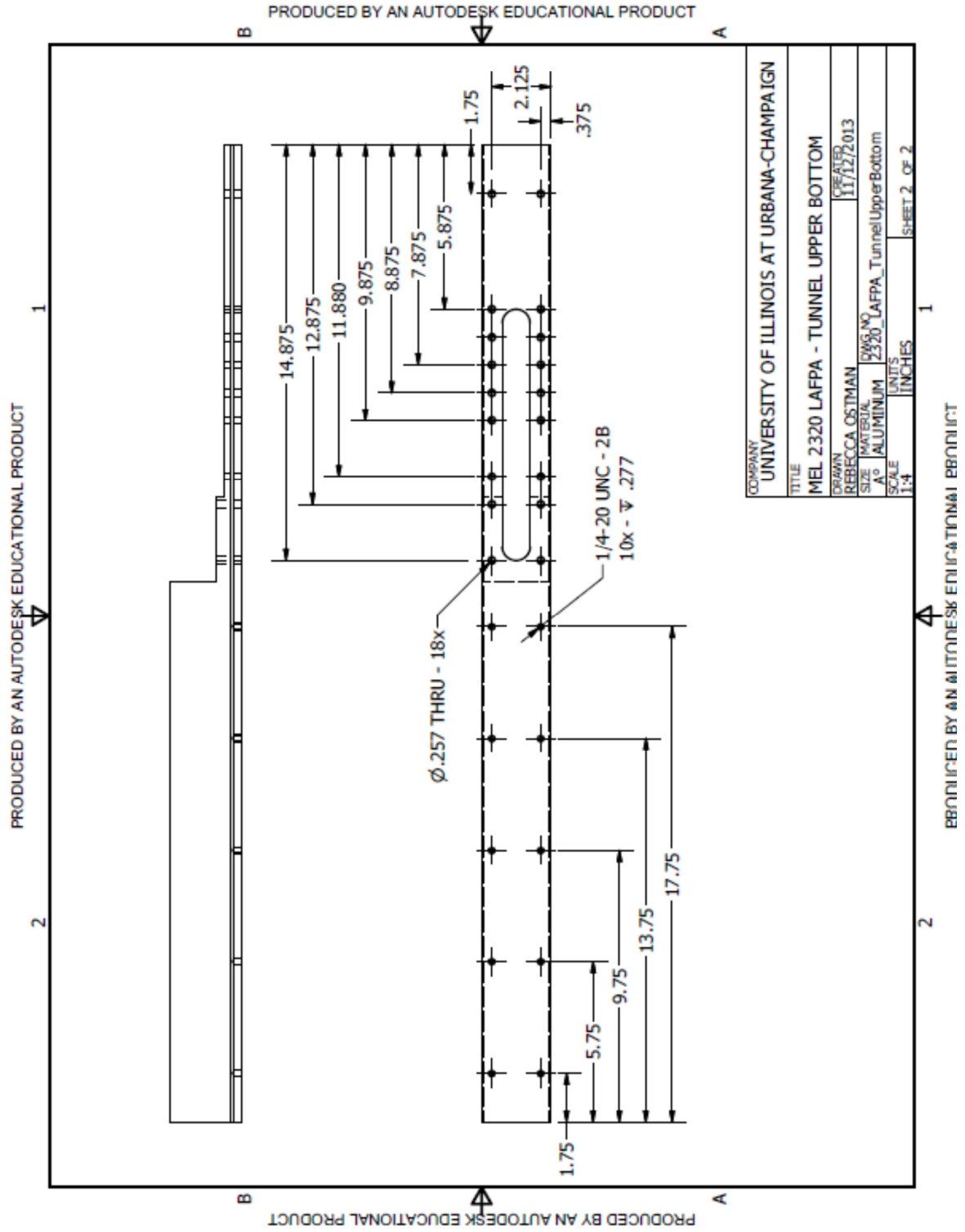

Fig. A.9 (cont.) b) second sheet of the drawing and specifications of the bottom wall of the wind tunnel, detailing the hole pattern.

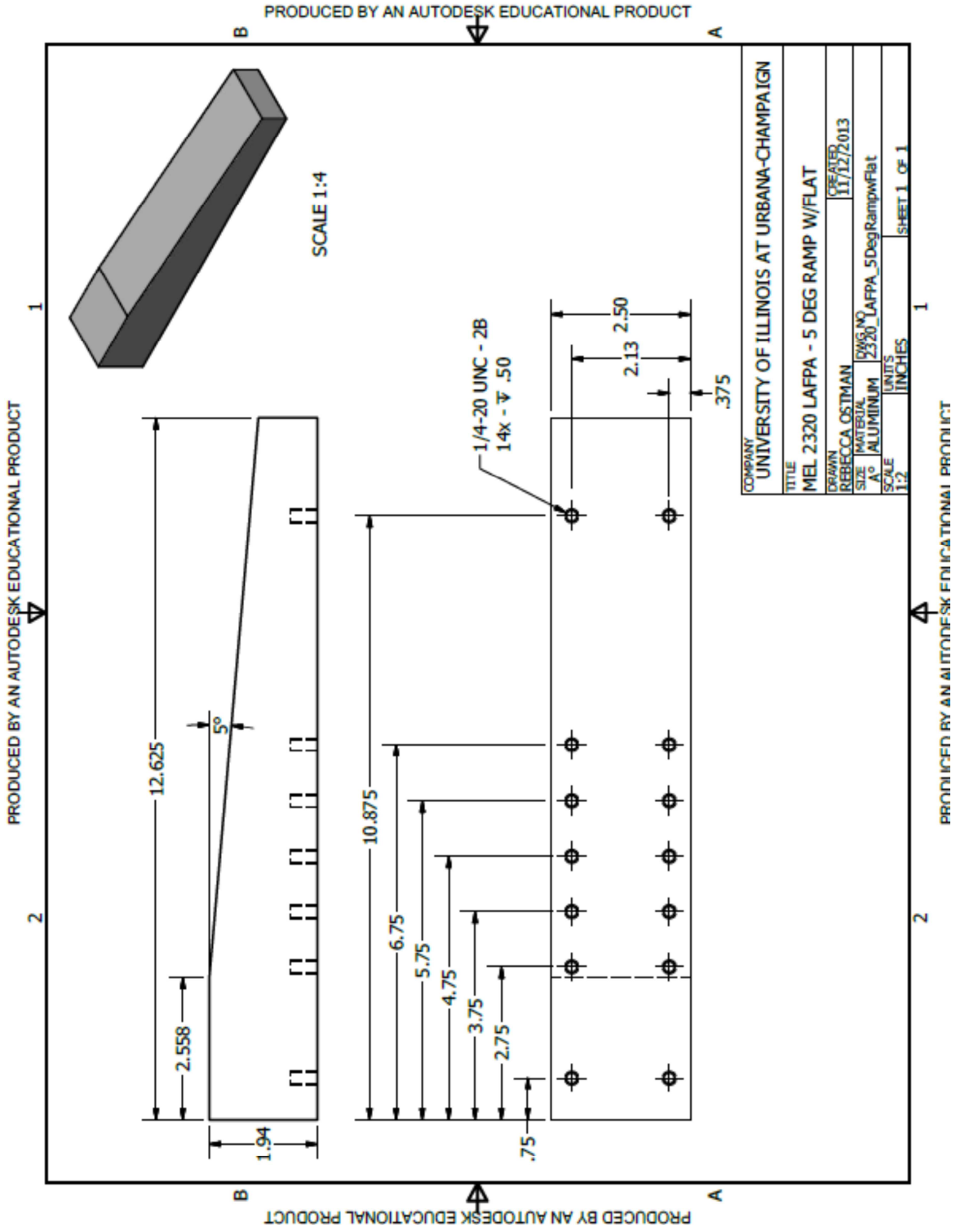

Fig. A.10 Drawing and specifications for the 5º diverging ramp for the LAFPAs upstream of the corner assembly.

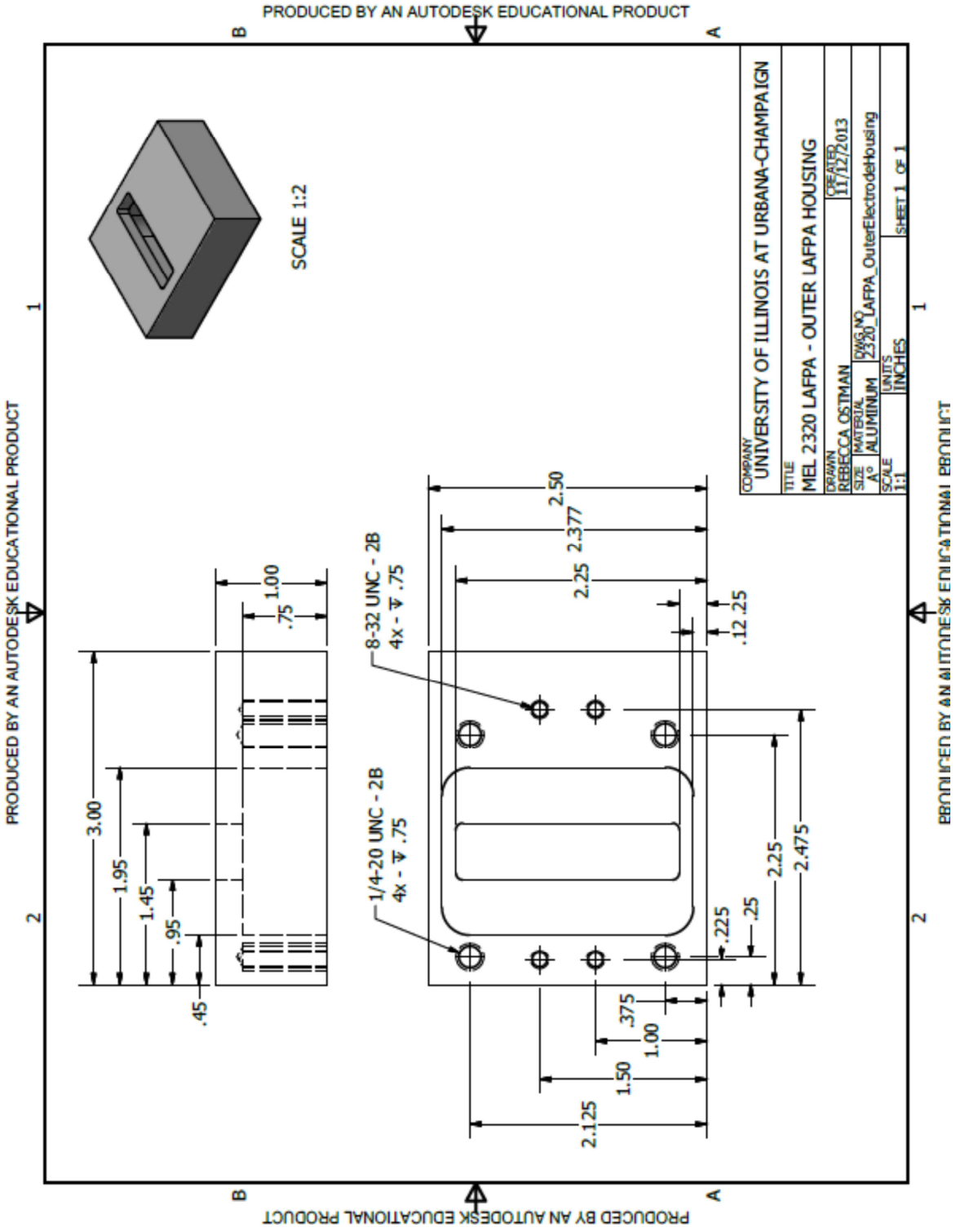

Fig. A.11 Drawing and specifications for the outer piece of the electrode housing for the LAFPAs upstream of the ramp corner assembly.

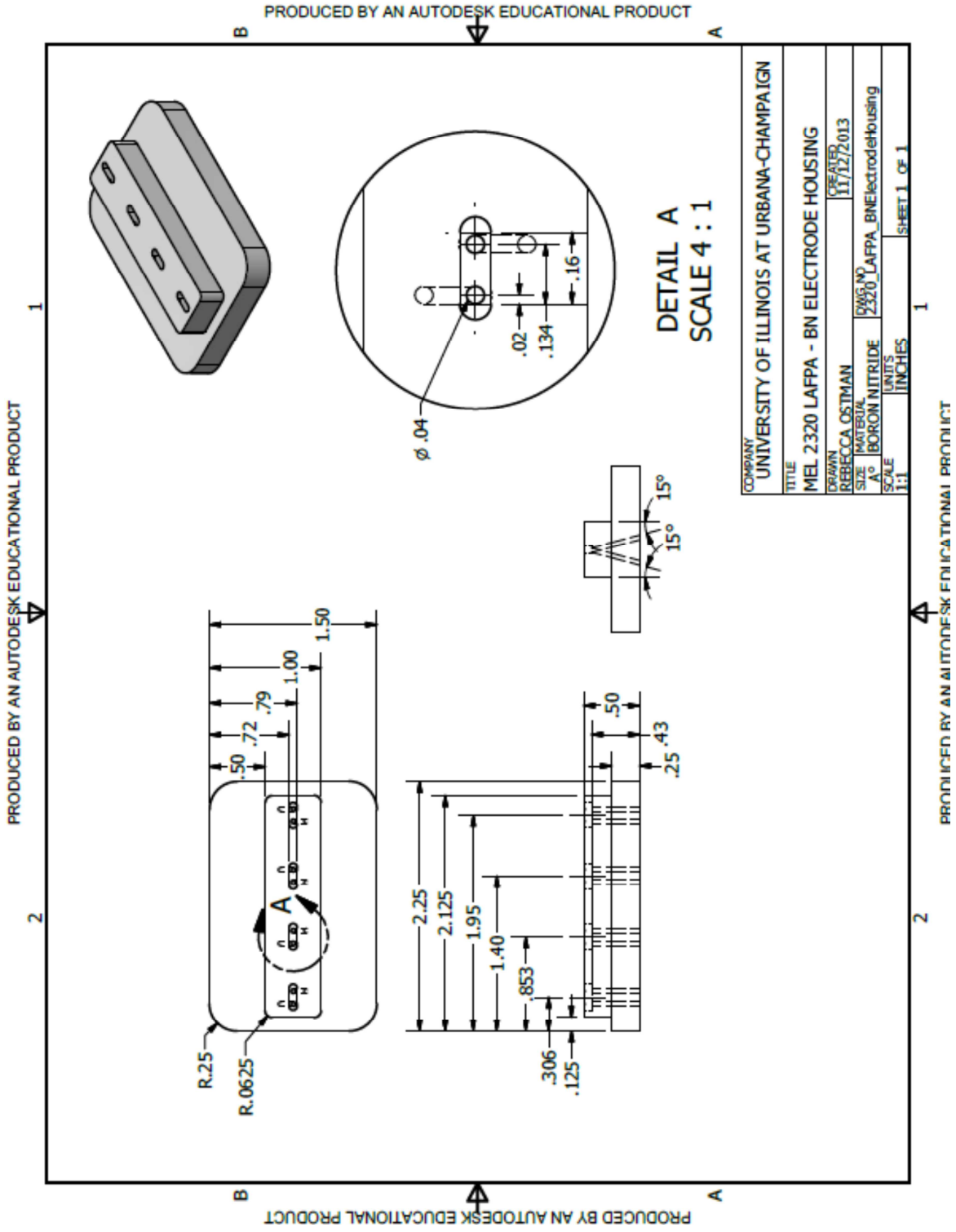

Fig. A.12 Drawing and specifications for the electrode cavities/housing for the LAFPAs upstream of the ramp corner assembly.

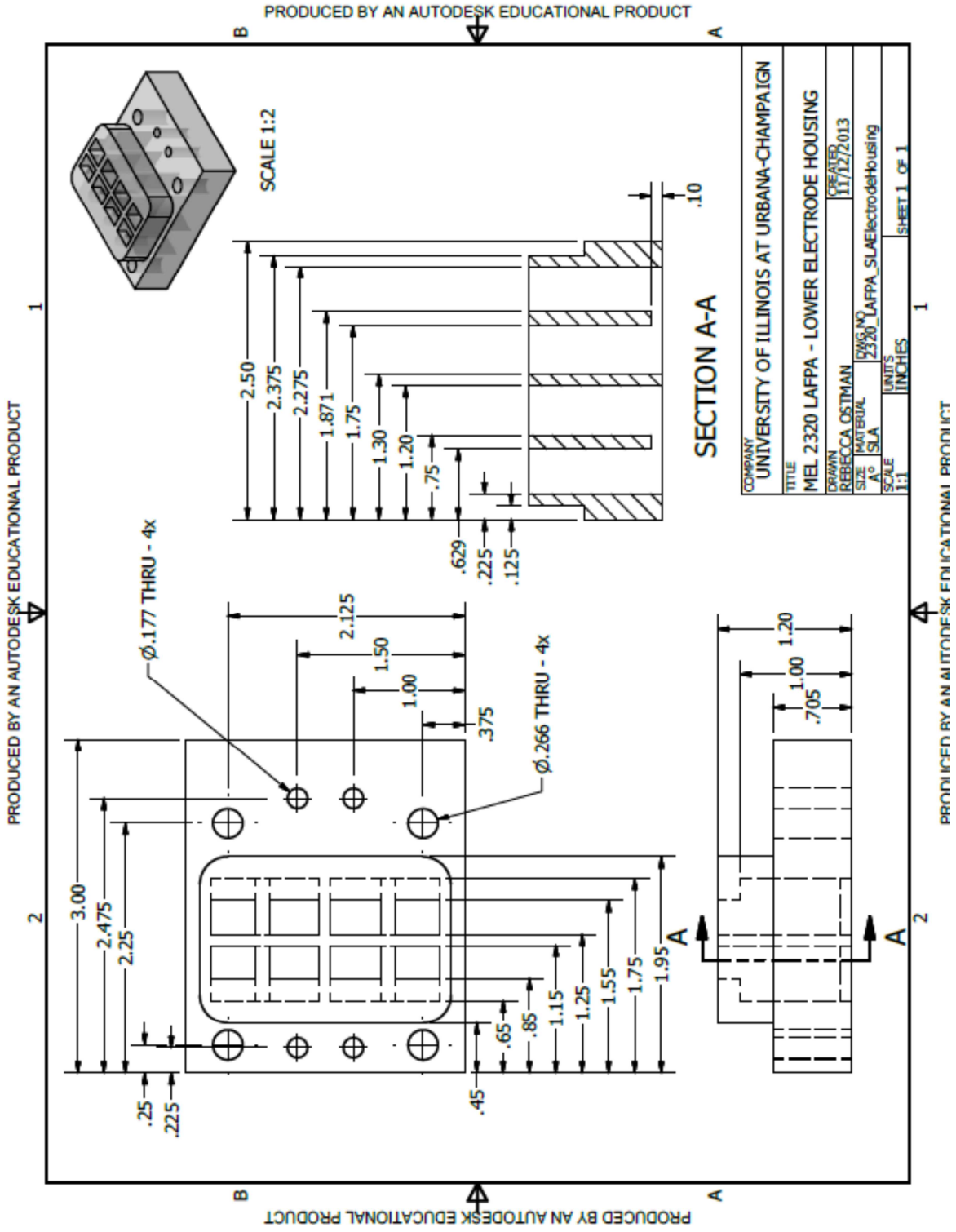

Fig. A.13 Drawing and specifications for the lower piece of the electrode housing for both the LAFPAs upstream and on the ramp corner assemblies.

A.3 LAFPAs On Ramp Corner Part Drawings

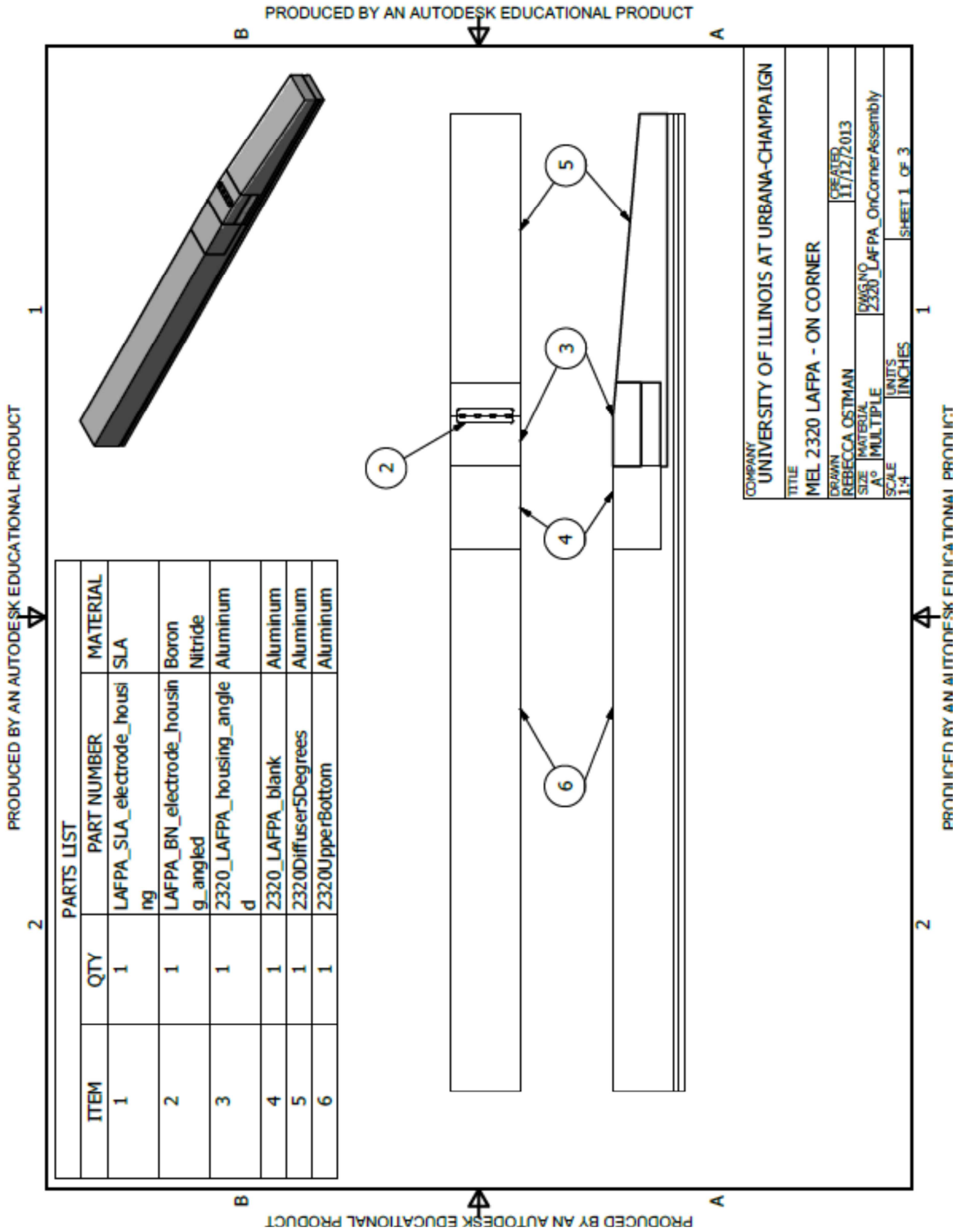

Fig. A.14 a) Base views and parts list for the LAFPAs on the ramp corner assembly,

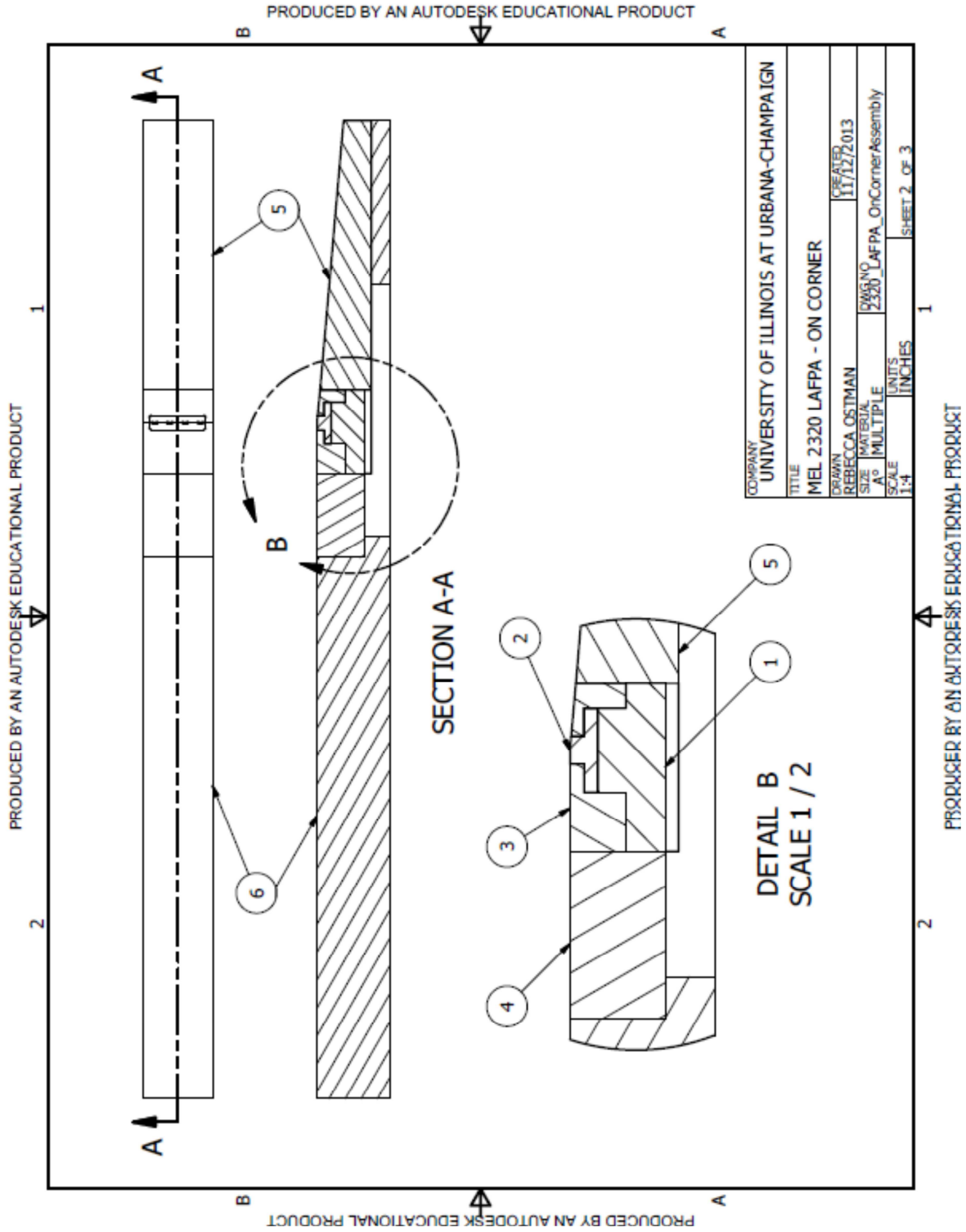

Fig. A.14 (cont.) b) cross section and detail views of the LAFPAs on ramp corner assembly,

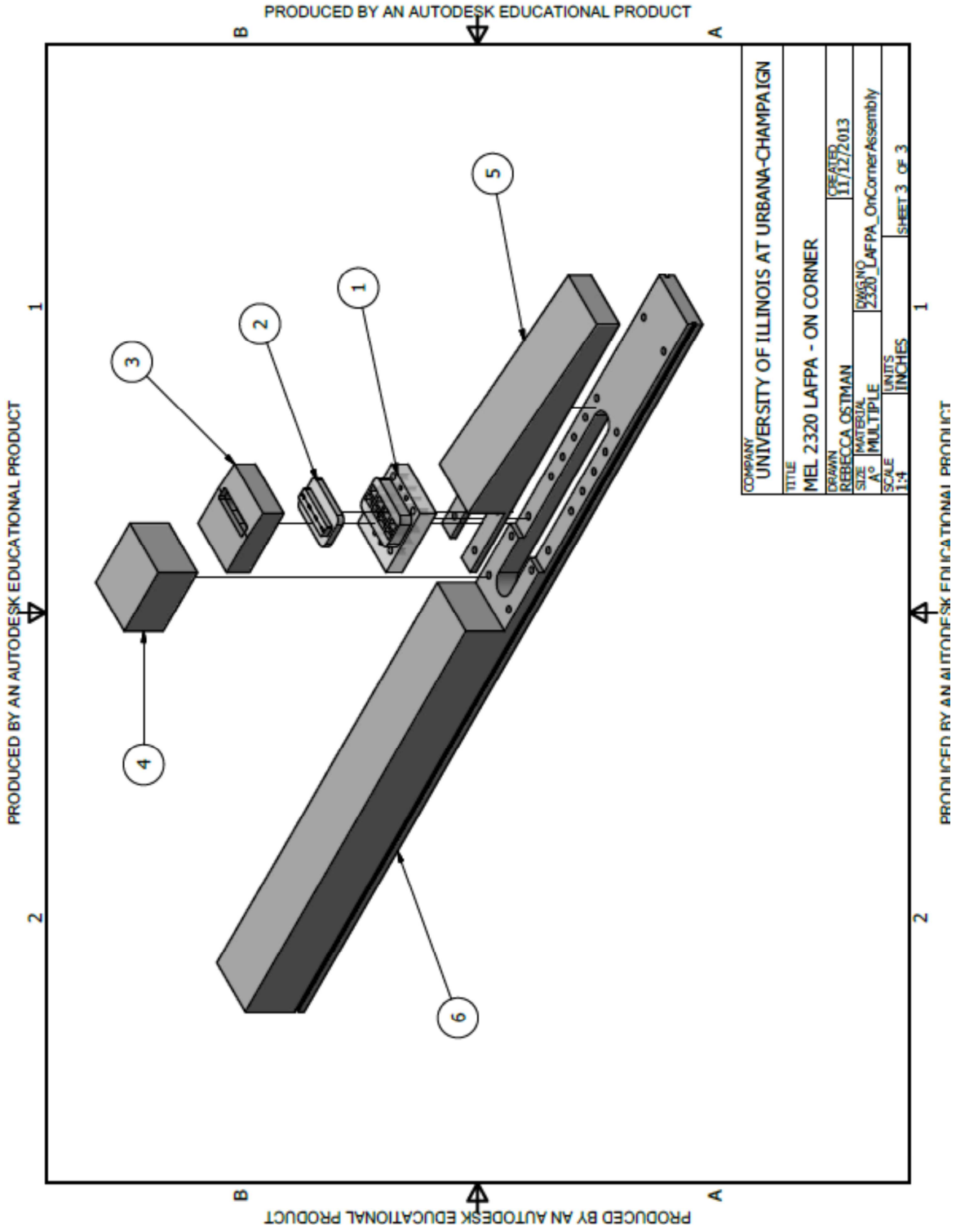

Fig. A.14 (cont.) c) exploded view of the LAFPAs on the ramp corner assembly.

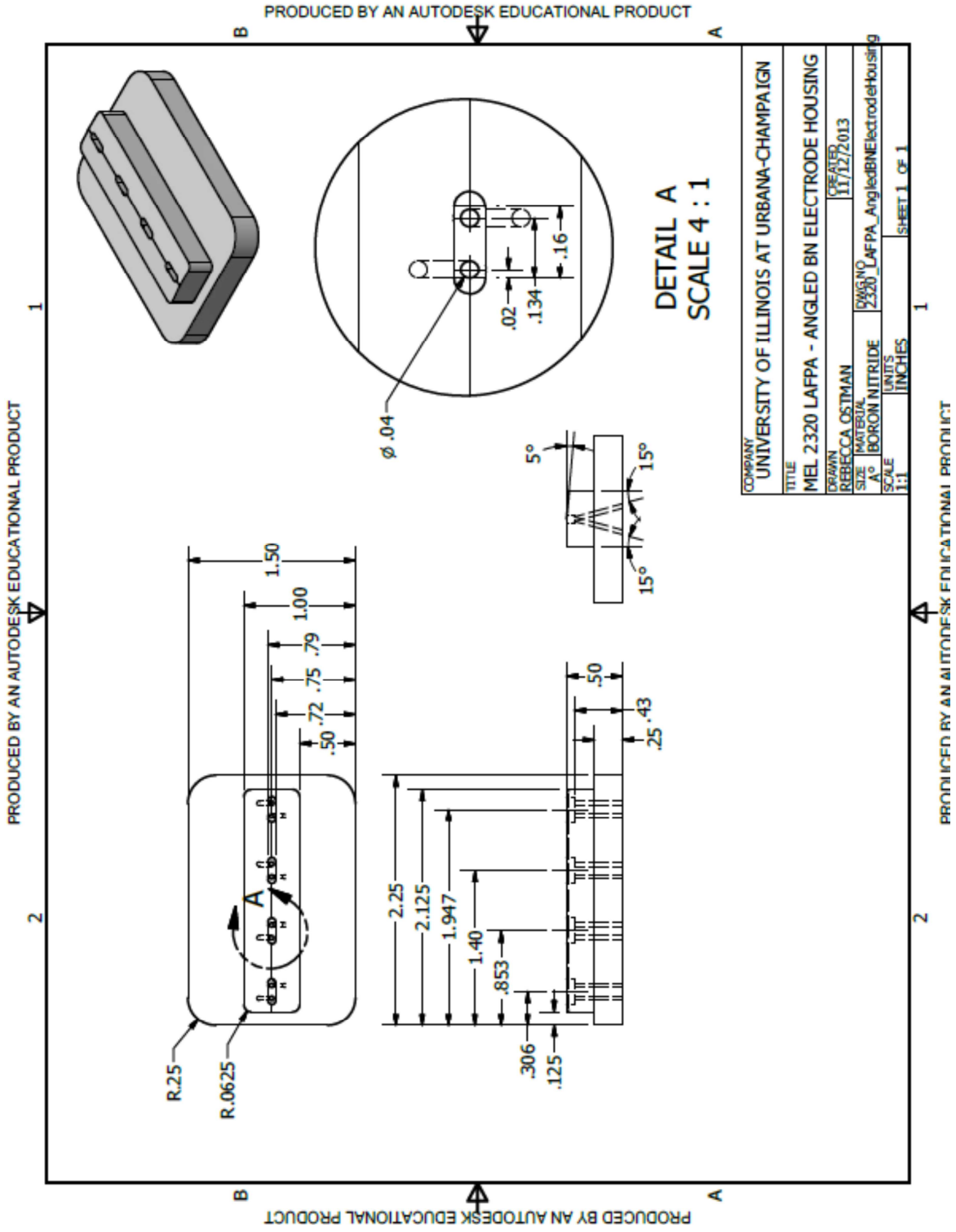

Fig. A.15 Drawing and specifications for the electrode cavities/housing for the LAFPAs on the ramp corner assembly.

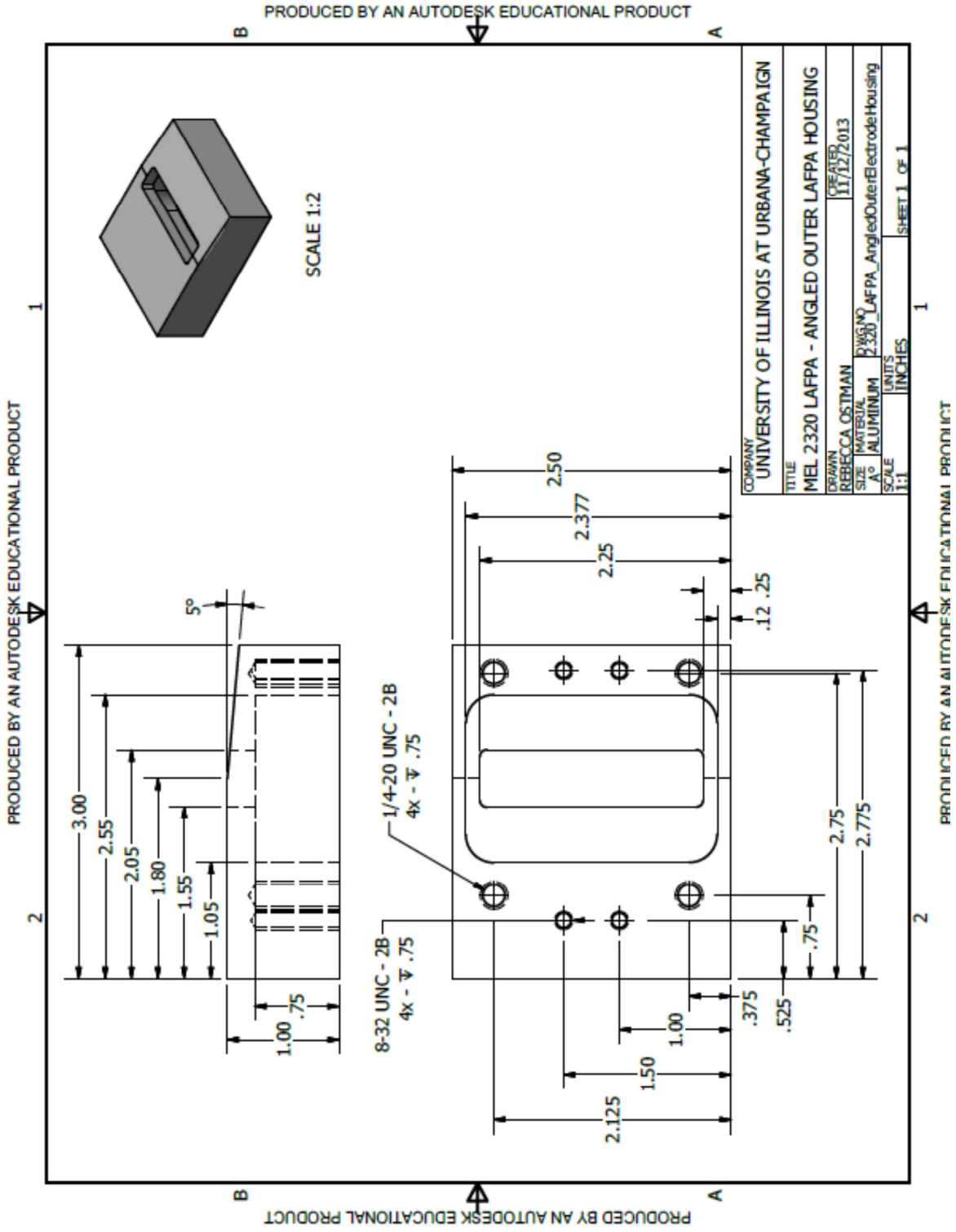

Fig. A.16 Drawing and specifications for the outer piece of the electrode housing for the LAFPAs on the ramp corner assembly.

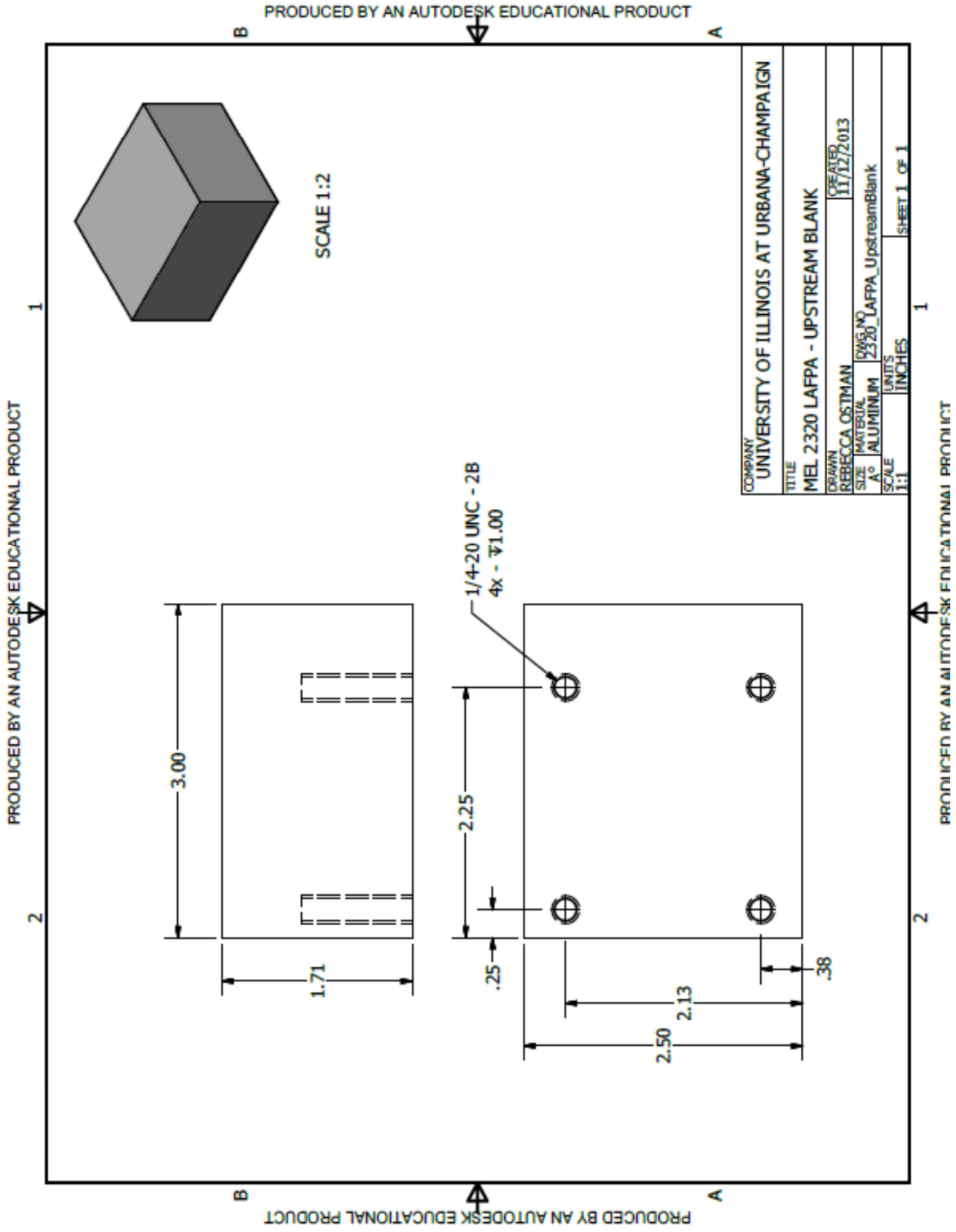

Fig. A.17 Drawing and specifications for the blank spacing block for the LAFPAs on the ramp corner assembly.

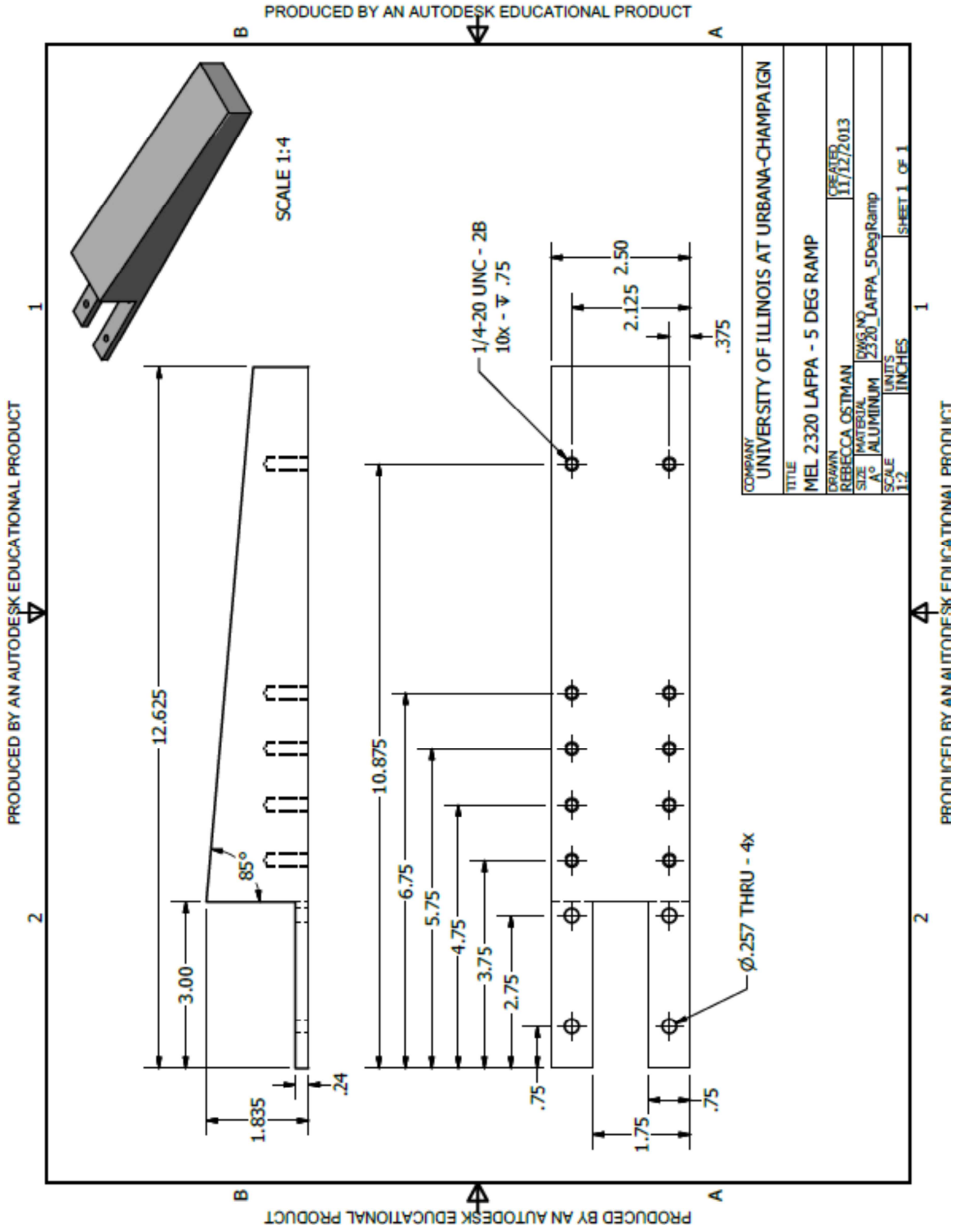

Fig. A.18 Drawing and specifications for the 5º ramp for the LAFPAs on the ramp corner assembly.